Particle Physics and Beam-Line Studies for the Electron-Positron International Linear Collider

John Colin Carter

Department of Physics

Royal Holloway University of London

Thesis submitted to the University of London for the

Degree of Doctor of Philosophy

October 2006

Abstract

The International Linear Collider (ILC) is being designed to be a high precision machine for conducting physics investigations with electron-positron collisions. The ILC is to operate at energies on the TeV scale and is required to deliver luminosities on the order of $10^{34}\text{cm}^{-2}\text{s}^{-1}$. To achieve these performance targets the ILC must employ a large array of diagnostic tools to monitor the beam conditions throughout transportation to the interaction point. Real-time measurement of the transport-invariant beam quality parameter, emittance, is essential for ensuring that high luminosity is delivered at the interaction point. The Laser-wire is a novel beam-profiling device that has been proposed as a non-invasive method of determining the emittance. The Laser-wire installation at the PETRA storage ring has been extensively simulated using GEANT4-based tools to successfully diagnose weak signal performance. Subsequent recommendations to modify to the experimental set-up have produced a significant enhancement of the signal.

To aid the ILC design process the BDSIM software package has been extensively modified, enabling the first instance of accelerator and detector descriptions to be modelled within a single code framework. Simulations of beam halo and associated backgrounds arriving at the interaction regions were conducted to set the performance requirements of the collimators in the beam delivery system. A comprehensive evaluation of the 2, 14, and 20 mrad extraction lines has been performed in terms of power loss from post-collision disrupted beams. The results indicate that the 2 mrad crossing angle design suffers intolerable levels of power loss, whilst the larger crossing angles are able to tolerate a wider range of beam conditions.

For my parents, Garry and Heather

who always believed in me

Contents

List of Figures

List of Tables

Acknowledgements

I am forever indebted to the following people for the help that I have received during my PhD studies. In Grahame Blair I have found a strong supervisor, colleague, and friend. I am incredibly grateful for his unwavering support and inspiring supervision throughout my PhD. The opportunities he has made possible over the last few years – including the experiences of working at DESY and SLAC – have been invaluable during these exciting times in linear collider studies.

My sincerest thanks goes to everyone at the Royal Holloway Particle Physics group – for putting up with my seemingly endless questions! In particular, I would like to thank Stewart Boogert for being the ROOT guru that he is and for taking the time to patiently pass on some of that knowledge.

I guess that some form of thanks must go David Hopkins – for keeping me sane with his wit and for equalling my need for coffee pit-stops. In a similar manner, I'd also like to thank the Royal Holloway Thai Boxing club for allowing me to vent my frustration through an accepted and controlled form of violence!

For their support and encouragement I thank all my friends and family. Foremost on this list are my parents, Garry and Heather, who have buoyed me with their love and provided me with endless and unquestionable support. Last, but certainly not least, I wish to thank Emma Williamson – for graciously allowing me to drag her half way around the world and back again, and for her unfailing belief in my ability.

Chapter 1

Introduction

The next generation of high energy colliders are expected to provide the opportunity to further probe the underlying nature of physics. The electron-positron international Linear Collider (ILC) has been proposed as one such experimental physics facility and is expected to deliver luminosities on the order of $10^{34}\mathrm{cm}^{-2}\mathrm{s}^{-1}$ in a high precision environment. To meet this luminosity goal, the ILC must collide beams with nanometer spot sizes at the interaction point. Achieving these groundbreaking goals requires an unparalleled level of research and development of beam delivery and diagnostic techniques.

Low beam emittance is essential in order to reach nanometer spot sizes, and its continuous measurement is therefore indispensable. In view of this, the Laser-wire scanner has been developed as a non-invasive method of measuring the high powered, yet unprecedentedly small, beam profiles. As discussed in chapter 5, the conceptual design of the Laser-wire has been realised at the PETRA storage ring. The spot sizes are measured by passing a finely focussed laser waist across the path of the electron bunches; the Gaussian profile of the bunch can be resolved by scanning in small steps and measuring the total energy of the resulting Compton-scattered photons as a function of scan position. The first experimental results from the PETRA Laser-wire project proved to be below theoretical expectations. However, this situation was verified – and subsequently rectified – after conducting realistic simulations.

After accelerating the beams to the collision energy, the beam delivery system must transport them to the interaction point. The optics lattice requires fine tuning in order to concurrently manage the beam and remove errant particles that would otherwise lead to intolerable background in the interaction regions. A range of studies – detailed in chapter 7 – have been conducted to evaluate the level of transport-related backgrounds in the 2 mrad interaction region, with the results used to set the performance requirements of the collimation system. Simulations of both the beam-lines and the detector regions prompted extensive modifications to an existing software package, BDSIM. The BDSIM code framework, along with benchmarking and modifications are outlined in chapter 6.

Once the beams have been collided they are highly disrupted and must be safely transported to high power dumps using extraction lines. The handling performances of the 2, 14, and 20 mrad extraction schemes have been evaluated in terms of the power loss from the disrupted beams.

Chapter 2

Motivation for the International Linear Collider

The last century has seen significant advancements in the area of particle physics, from early research on subatomic particle identification through to internationally collaborated high energy collision experiments. With each new experiment our understanding of the fundamental laws of physics has developed, allowing the postulation of many theoretical and practical models. To date, investigations of particle theories such as the Standard Model (SM) have been largely successful yet continue to leave gaps in our understanding. With this in mind, this chapter will attempt to outline the physics motivation for designing and building the ILC. A more detailed introduction into SM physics can also be obtained from [1].

2.1 The Standard Model and Beyond

The SM is a highly successful working theory for describing particle interactions and the fundamental nature of matter. In the SM, particle interactions occur via the exchange of mediatory particles referred to as "gauge" bosons. The SM building blocks of matter are divided into two particle groups – leptons and quarks – collectively known as fermions.

2.1.1 Fermions

Fermions are half-integer spin particles that can be divided into three generations of quarks and leptons. The current understanding of fermions indicates that they are point-like and are therefore considered to be elementary particles. Table 2.1 lists some of their key properties.

Table 2.1: Fermion table of properties. Data taken from [2] and [3]

	Generation	**Flavour**	**Symbol**	**Charge [e]**	**Mass [MeV/c^2]**
Leptons	1^{st}	electron	e^-, e^+	-1, 1	0.51100
		electron neutrino	$\nu_e, \overline{\nu}_e$	0	$< 3 \times 10^{-6}$
	2^{nd}	muon	μ^-, μ^+	-1, 1	105.66
		muon neutrino	$\nu_\mu, \overline{\nu}_\mu$	0	< 0.19
	3^{rd}	tau	τ^-, τ^+	-1, 1	1777.0
		tau neutrino	$\nu_\tau, \overline{\nu}_\tau$	0	< 18.2
Quarks	1^{st}	up	$u, \overline{u}$	2/3, -2/3	1.5 to 4
		down	$d, \overline{d}$	-1/3, 1/3	4 to 8
	2^{nd}	strange	$s, \overline{s}$	-1/3, 1/3	80 to 130
		charm	$c, \overline{c}$	2/3, -2/3	1150 to 1350
	3^{rd}	bottom	$b, \overline{b}$	-1/3, 1/3	4100 to 4900
		top	$t, \overline{t}$	2/3, -2/3	171400

Quarks combine to form composite particles known as hadrons, which are grouped into either “Baryons” or “Mesons”. Baryons are the combination of three quarks of any flavour whereas mesons are formed by one quark and one antiquark, also of any flavour.

Although experimental data has agreed with many of the predictions of the SM there are still several interesting questions regarding the fermions that remain unanswered by the current understanding of the SM:

- It is not clear why there are three distinct generations across the leptons and quarks.

- The mass spectrum of the leptons is not easily comparable to that of the quarks; the former having a relatively small mass range in comparison to the latter.

- Until recently the neutrinos were considered to have zero mass. Although their masses are not precisely known, oscillation experiments such as [4] have set upper limits. The introduction of neutrino masses requires a revision in the SM and has significant implications in other areas of physics such as astrophysics. In light of this, neutrino physics is currently a very active area of research.

2.1.2 Interactions and Gauge Bosons

Current particle theory suggests that the fermions interact via the exchange of gauge bosons resulting in the four fundamental interactions shown in Table. 2.2. Mediated by the Graviton boson, Gravity is the weakest of all the forces and is important on astronomical scales. The Electromagnetic (EM), Weak, and Strong interactions are the predominant forces in particle physics.

Table 2.2: Table of properties for the gauge bosons. Data taken from [2]

Interaction	**Exchanged Boson**	**Charge [e]**	**Mass [GeV/c^2]**
Electromagnetic	γ (photon)	0	0
Weak	W^-, W^+	-1, 1	80.4
	Z	0	91.2
Strong	g (gluon)	0	0
Gravity	G (graviton)	0	0

Electromagnetic and Weak Interactions

The EM interaction occurs between charged particles through the exchange of massless photons and is therefore long ranged and relatively strong. This interaction is well understood both classically through Maxwell's equations, and also quantum mechanically via quantum electrodynamics (QED) theory.

Mediated by massive particles, the weak interactions are relatively short range. Although the intrinsic strength of the weak force (g_w) is comparable to that of the EM interaction (e), when the large masses of the $W^{\pm}$ and Z^0 are accounted for the force appears to be weak.

The EM and weak interactions have been theoretically unified to form the Electroweak theory under the $SU(2) \times U(1)$ gauge group. Contributions to work in this area led to the joint awarding of the Nobel Physics prize to Glashow, Weinberg, and Salam in 1979.

Strong Interaction

Theoretically described by quantum chromodynamics (QCD), the strong force introduces three colour charges for each quark species to evade Pauli's Principle that no two fermions can simultaneously occupy the same quantum state. The interaction is mediated by gluons which exchange the "colour" of the quarks. At low energies the coupling constant (g_s) is relatively strong and leads to "confinement" – which dictates why no free quarks are observed.

2.1.3 Higgs Boson

In the SM the fundamental particles are thought to acquire their mass via the Higgs mechanism, which describes the spontaneous symmetry breaking of local gauge theory [1]. The masses of the weak gauge bosons, for example, are not deducible directly from the $SU(2) \times U(1)$ theory, but are instead speculated to arise from electroweak symmetry breaking (EWSB). As a result of this symmetry breaking the massless fields combine to form the $W^{\pm}$ and Z^0 along with a new scalar particle in the SM referred to as the Higgs boson, H^0 – which has yet to be detected experimentally. The LEP (Large Electron-Postiron) machine at CERN (European Organisation for Nuclear Research) conducted extensive searches for the Higgs boson, placing lower limits on the SM Higgs of $M_H > 114.4$ GeV

[5]. As a free parameter in the theory the mass of the Higgs is an unknown, yet a mass in the range of 115 to 200 GeV produces reasonable agreement between theoretical predictions and the experimentally known electroweak data [2]. Indeed, a Higgs mass in the range of $130 \leq M_H \leq 180$ GeV is expected to allow for the renormalisation and extension of the SM up to the Planck scale of $\sim 10^{19}$ GeV, as illustrated by Fig. 2.1. If the Higgs is found experimentally to lie outside of the bounds given in Fig. 2.1 then this will be a good indication to the requirement of theoretical extensions beyond that of the SM.

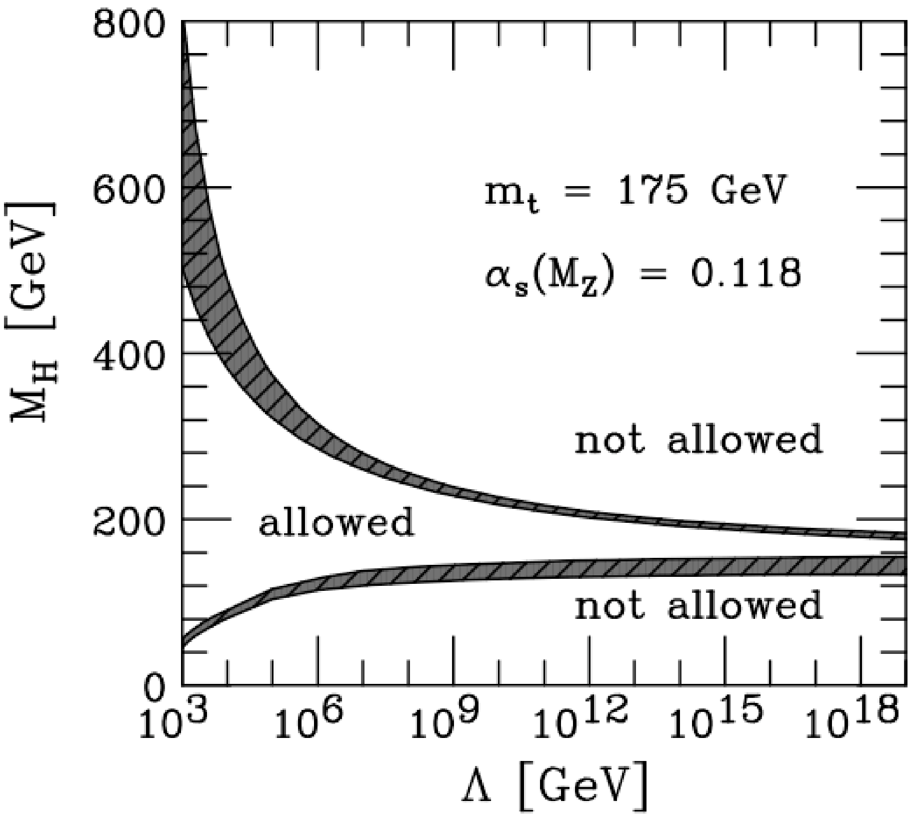

Figure 2.1: Bounds on the Higgs boson mass [6]: the upper boundary is defined to allow physics at energy scales Λ to continue to be described by the SM; the lower boundary is found through stability requirements assuming $m_t = 175$ GeV and $\alpha_s = 0.118$.

2.1.4 Beyond the Standard Model

As well as the fermion-related open questions noted in section 2.1.1 there are still several fundamental answers sought after for the SM – such as the idea of the unification of the interactions and the hierarchy problem. In the first instance, two of the four fundamental interactions have already been unified to form the electroweak theory. The third interaction – the strong force – is comparably important in particle physics phenomena and yet the unification of all three has yet to be accomplished. In fact it is a noteworthy quandary as to why the three coupling constants associated with these interactions do not converge at higher energy scales. Extending this idea of unification would raise the question as to whether the fourth interaction – Gravity – can also be unified with the other three forces.

In general terms, the hierarchy problem refers to the vast differences observed in the SM where similarities would be expected. For instance, although there are significant differences in the field strengths of the EM, Weak, and Strong forces, they are all relatively similar and incredibly large in comparison to Gravity. The hierarchy problem is evident in other areas such as the mass of the Higgs boson. From SM theory radiative corrections to the mass of the Higgs particle should be taken into account when performing mass calculations. According to the SM, corrections such as fermion loops (see Fig. 2.2a) should cause the M_H to quadratically diverge from the expected mass range. In this situation M_H is more sensitive to the heavier fermions such as the top quark, proving the precise knowledge of the top mass to be invaluable.

Minimal Supersymmetric Standard Model

To deal with these problems many extensions to the Standard Model have been suggested, including various supersymmetry (SUSY) theories. The smallest SUSY extension to the SM is known as the Minimal Supersymmetric Standard Model (MSSM). Within this framework every particle has a supersymmetric partner where the main difference between SM and MSSM variants is the spin of the particle, e.g. SM fermions of half integer spin have boson integer spin superpartners in MSSM. In this way the number of particles is effectively doubled as illustrated by Table 2.3.

Table 2.3: Overview of MSSM particle content

SM		**MSSM**	
Gauge Bosons (spin-1)	γ g $W^{\pm}$ Z^0	**Gauginos** (spin-$\frac{1}{2}$)	$\tilde{\gamma}$ $\tilde{g}$ $\tilde{W}$ $\tilde{Z}$
Leptons (spin-$\frac{1}{2}$)	$\begin{pmatrix} l \\ \nu_l \end{pmatrix}_L$ l_R $l = e, \mu, \tau$	**Sleptons** (spin-0)	$\begin{pmatrix} \tilde{l} \\ \tilde{\nu}_l \end{pmatrix}_L$ $\tilde{l}_R$ $l = e, \mu, \tau$
Quarks (spin-$\frac{1}{2}$)	$\begin{pmatrix} q_{up} \\ q_{down} \end{pmatrix}_L$ $\begin{pmatrix} q_{up} \\ q_{down} \end{pmatrix}_R$ $q_{up} = u, c, t$ $q_{down} = d, s, b$	**Squarks** (spin-0)	$\begin{pmatrix} \tilde{q}_{up} \\ \tilde{q}_{down} \end{pmatrix}_L$ $\begin{pmatrix} \tilde{q}_{up} \\ \tilde{q}_{down} \end{pmatrix}_R$ $q_{up} = u, c, t$ $q_{down} = d, s, b$
Higgs Bosons (spin-0)	H^0 $H^{\pm}$	**Higgsinos** (spin-$\frac{1}{2}$)	$\tilde{H}^0$ $\tilde{H}^{\pm}$

The addition of the new SUSY particles was prompted by the need to provide a solution to some of the SM issues such as the hierarchy problem. For instance, the new particles must be included in the radiative corrections for the mass of the Higgs Boson, Fig. 2.2b. As the SUSY particles have the same mass but different spin components to their SM counterparts, this has the effect of causing the SM correction terms to be directly cancelled by those from the superpartners. In this way the MSSM theory is able to negate the hierarchy problem associated with the mass of the Higgs Boson.

It should be noted that MSSM is not the only theory to be suggested to tackle the problems associated with the SM. Indeed the MSSM is not without its own parameter related problems that alternate theories have attempted to address.

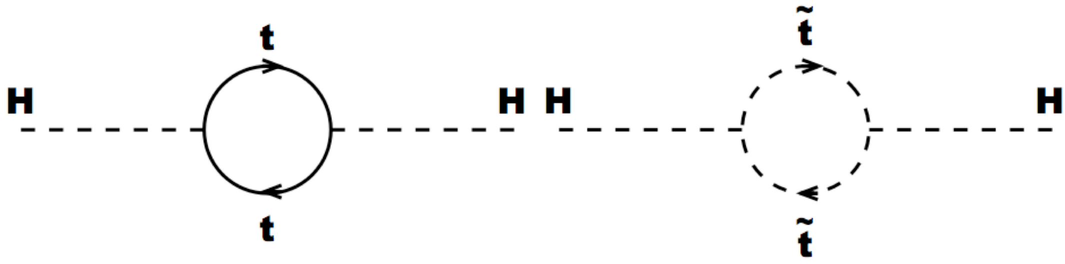

(a) (b)

Figure 2.2: Example of the radiative loop corrections that must be considered when calculating the Higgs boson mass in a) the SM and b) SUSY theories. Due to the differing spin components, SM and SUSY corrections of this form cancel directly with each other.

2.2 Collision Energy

In many respects the frontier of particle physics has been pushed by an ever-increasing availability in the centre of mass energy (E_{cm}), Fig 2.3. This rise in collision energies is partly motivated by the fundamental Einstein relation, $E = mc^2$, which indicates that the creation of heavier particles requires larger energies. For electron-positron collisions the highest E_{cm} of just over 200 GeV was achieved by the circular LEP machine at CERN.

Circular-based collider facilities such as CERN face the problem that charged particles forced to move in a curved trajectory by the use of magnetic fields lose energy via the emission of Synchrotron Radiation (SR). The fraction of energy lost ($\Delta E/E$) by a charged particle of mass m and energy E per revolution in a circular storage ring of radius R can be given as [7]:

$$\frac{\Delta E}{E} = 8.85 \times 10^{-5} \times \left(\frac{m_e}{m}\right)^4 \frac{(E[GeV])^3}{R[m]} \tag{2.1}$$

In the LEP ring this equated to an energy loss of approximately 2% per revolution, which meant that the beam had to be regularly re-accelerated to make up for the energy loss. As energy loss (ΔE) goes with E^4, increasing the E_{cm} was not economically feasible at LEP when considering power costs. From Equation 2.1 there are two possibilities

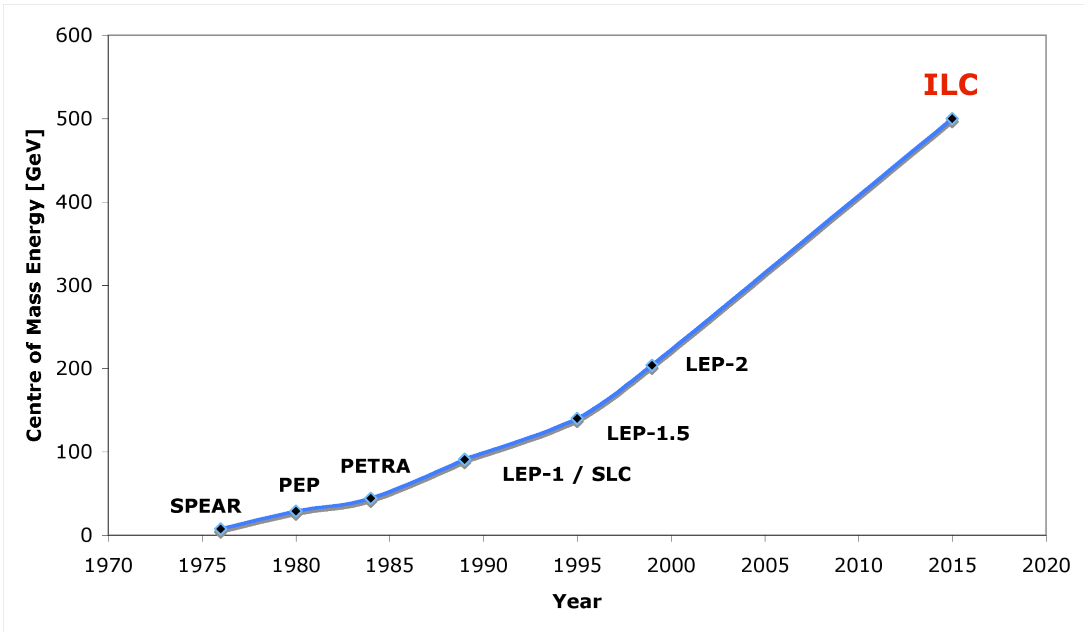

Figure 2.3: Historical timeline of E_{cm} achieved by electron-positron facilities.

for offsetting the energy loss when increasing the particles' energy: increasing the mass of the particle, and/or increasing the radius of curvature. The first of these options has already been incorporated into the latest facility being built at CERN – the Large Hadron Collider (LHC). This is being built using the old LEP tunnel and infrastructure and will collide protons instead of electrons. As protons have a mass 1.84×10^3 times greater than that of electrons, the E_{cm} can be raised much higher for a given radius of curvature. By spring 2008 the LHC expects to be colliding protons with a total E_{cm} of 14 TeV – which corresponds to an easily recoverable radiated loss of 4.3 keV per beam. It should be noted however that the collision of protons typically involves the interaction of the constituent quarks and gluons, and as such the deliverable E_{cm} for a given collision is nearer to 1/10th of the total 14 TeV. The second option for reducing the energy lost through SR is achieved by a linear collider design whereby the radius of curvature is infinitely increased. In this way the ILC aims to collide beams on the TeV scale with minimal losses from SR.

2.3 Deliverable Luminosity

Within a given energy regime, a viable particle process has a certain probability of occurring – proportional to its cross-section, σ. The number of such processes (N) observed over a certain period of time (dt) is given as [8]:

$$N = \sigma \int \mathcal{L} dt \tag{2.2}$$

where $\mathcal{L}$ refers to the luminosity, defined as:

$$\mathcal{L} = f \frac{N_1 N_2}{4\pi\sigma_x^* \sigma_y^*} H_D \tag{2.3}$$

where f is the frequency of the bunch collisions; N_1 and N_2 are the number of particles populating the bunches of each beam; σ_x^* and σ_y^* are the horizontal and vertical RMS widths of the colliding bunches at the interaction point (IP); H_D is the “pinch” factor that relates to the self-focussing effect of the bunches during high energy collisions. From Equation 2.2 it can be deduced that in order to increase the number of rarer processes (i.e. those with lower cross-section) observed it is necessary to either run the machine for a longer time period or to increase the luminosity.

After an initial start-up period, the ILC is specified to produce a luminosity of 2×10^{34} m^{-2}s^{-1} which is to be compared with the peak luminosity of 10^{32} m^{-2}s^{-1} achieved during the final years of LEP running. From Equation 2.3 there are several methods by which the ILC could chose to reach its luminosity target. In single-pass machines such as a linear collider all the energy put into accelerating the beams is lost into the beam dumps. Therefore a dramatic increase in the collision frequency or bunch population would be economically unfeasible in terms accelerating costs. To increase luminosity the ILC will take the alternative method of decreasing the collision spot size to be approximately 5 nm vertical by 200 nm horizontal. It should be noted however that such a small spot size places a stringent limit on the emittance of the beam which, in conjunction with the high beam power, will require a large amount of R&D effort into novel beam diagnostics and emittance measuring techniques such as the Laser-wire scanner, covered in chapter 5.

2.4 Physics at the ILC

As mentioned in section 2.2 the LHC is due to start operation in 2008 as a proton-proton collider. With a proposed first beam date of 2015, the ILC will be following the LHC in the exploration of TeV-scale physics. Rather than conflict or overlap with the proposed studies at the LHC, the ILC is being designed as a complementary and yet groundbreaking machine in its own right. A comprehensive overview of the physics interplay between the ILC and LHC can be found in [9].

2.4.1 High Precision

As protons are composite particles their collision in the LHC can be more precisely defined as the interaction of their elementary constituents – the quarks and gluons. Whilst observing one particular interaction of interest it is likely that others can take place between the remaining proton constituents – known in this case as “spectator” particles. This can add a confusing background to the proton collisions, which are already complex as a result of the large amounts of hadronic showering. In contrast to this situation, the ILC will be colliding elementary electrons and positrons which are expected to result in much lower and also more definable levels of background. As a direct result of this the ILC is often referred to as having “clean” interactions or being a “clean” machine.

Threshold Scans

The elementary nature of the colliding particles in the ILC has the advantage of allowing for the fine tuning of the E_{cm} by changing the energy of one or both of the beams. This is in contrast to the LHC whereby the composite nature of the colliding particles means that only a loose range can be set on the E_{cm}. The ILC can therefore be used to help determine the mass of particles by scanning the E_{cm} in small steps across their pair production threshold. High precision measurements on the mass of the particle can be obtained by examining how the pair production excitation curve changes with E_{cm}.

An example of how threshold scans can play an important role in particle physics is the placing of a higher precision on the top quark mass by observing $t\bar{t}$ production. Completing the SM picture of matter fermions, the top quark was discovered at the Collider Detector at Fermilab (CDF) experiment at the Tevatron in 1995 [10] with a mass of $M_t = 176 \pm 8 \pm 10$ GeV/c^2. Recent preliminary studies combining the latest data from both CDF and D0 have greatly improved the precision on the top mass to $M_t = 171.4 \pm 2.1$ GeV/c^2 [3] – which includes both statistical and systematic errors and corresponds to an overall precision of 1.2%. Threshold scan simulations [11], accounting for expected statistical and systematic errors, predict that the ILC could reduce the uncertainty on the top quark mass to ≤ 100 MeV/c^2. When the E_{cm} is in the vicinity of $2M_t$ the $t\bar{t}$ production rate will increase as illustrated by the cross-section plots in Fig. 2.4. Fitting this curve against the theoretical prediction will determine the mass of the top quark. Fig. 2.4 shows the theoretical sensitivity of the top cross-section to the top Yukawa, y_t and smearing effects from beam-related effects.

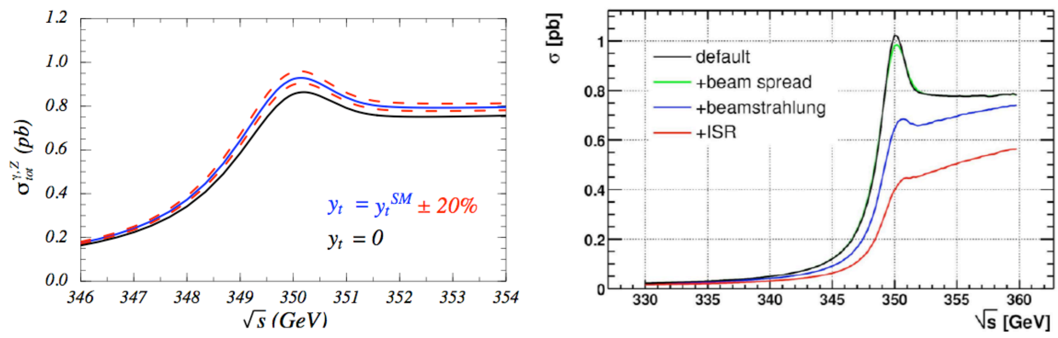

(a) (b)

Figure 2.4: Top cross-section predictions for a) the dependance of the top cross-section on the top Yukawa (y_t) based on a SM Higgs with $M_H = 115$ GeV [12] and b) the smearing of the $t\bar{t}$ cross-section by beam effects and initial state radiation [13].

With the top being the heaviest of all the quarks, knowing its mass with more precision will give a unique handle on several important areas of particle theory [14], including the following:

- The large top quark mass means that it is close to the electroweak symmetry breaking scale. If the Higgs boson is found to exist then it will have a larger coupling with the top quark due to its mass. This in turn opens up a range of possibilities for pinning down extensions to the SM.

- When comparing the leptons and quarks (see Table 2.1) the intra-family range of masses are noticeably disproportionate. Knowing the top mass with a greater precision will be invaluable for future theories of flavour dynamics and mass relations.

- As discussed in section 2.1.4 for the particular example of the Higgs boson, the top mass must be taken into account for radiative corrections to a wide range of particle mass calculations. Precise knowledge of its value therefore plays an important role in particle theory.

Polarised Beams

The ILC baseline design specifies that it should operate with polarised electron beams, with an optional upgrade to polarised positrons. The electron polarisation is planned to be at least 80% with a measurement accuracy of $\sim$0.5%, although recent R&D has suggested that 90% polarisation may be achievable. The degree of polarisation of the positrons is currently under debate, and is expected to reach 60% with little or no impact on luminosity. Higher levels of polarisation can be achieved by sacrificing deliverable luminosity in the process.

Polarised beams are important for the detailed study of a variety of physics processes. In top quark searches, the neutral coupling of the top to electroweak gauge bosons can only be investigated at lepton facilities as hadron colliders typically use gluon exchange for the top pair production. Polarising the beams at a lepton facility will allow for the measurement of the left-right asymmetry of the top vector coupling.

An interesting advantage to colliding polarised beams is that it is possible to exclude certain interactions – which can be useful for reducing background. For instance, the $W^{\pm}$ gauge bosons only couple to left-handed particles (or right-handed anti-particles). Taking this into account it should be possible to choose the polarisation of one or both of the beams such that interactions mediated by the $W^{\pm}$ are suppressed.

The need for polarised beams is widely accepted in the physics community and an extensive examination of the physics case for polarisation at a linear collider can be found in [15] – in which the requirement for both beams to be polarised is highly stressed. In many of the discussed physics cases the use of polarised beams does not necessarily open up exclusive areas of research, but instead offers an opportunity of increased understanding.

Chapter 3

Beam-Related Physics Processes

Beam halo and associated background are critical factors that must be considered throughout the design process of both the Beam Delivery System (BDS) and the Interaction Regions (IR's). Beam-beam interactions at the IP produce a large contribution to the background in the IR and also in the beam extraction lines. This chapter introduces all of the background physics and particle processes that are used throughout the studies incorporated in this thesis.

3.1 Beam Halo

Ideally the beam should be transported throughout the acceleration and delivery phases with all particles being contained within a well defined set of spatial and momentum limits. In reality the main core of the beam is accompanied by errant particles that are typically referred to as halo particles. Following the typical TESLA definition [16], a halo particle can be defined as one which is either outside the energy acceptance of 1.5% or has a betatron amplitude in the vertical plane greater than 30 standard deviations. Observations from Stanford Linear Collider (SLC) operation [17] have led to the prediction that the number of halo particles at the ILC will be approximately 10^{-3} – 10^{-4} of a bunch. The experience at the SLC showed that the low energy region of the accelerator, in particular the damping rings, were major contributors to the beam halo [18]. The underestimation of the beam halo at the SLC highlighted the importance for understanding the levels expected for a given ILC damping ring design. Post-SLC theories, applied to Next Linear Collider (NLC) designs, have suggested that intrabeam scattering can constitute a large component of the emittance growth in damping rings - especially in the creation of large non-Gaussian tails through hard single particle scattering processes [19]. However, a direct result of the loose categorisation of halo particles is that there are a large number of potential sources that can attributed to their production, the most important of which will be outlined in this section.

3.1.1 Physical Processes

There are a number of physical processes that can be lead to the formation of beam halo. Residual gas in the beam pipe of the accelerator can give rise to elastic (e.g. Coulomb) and inelastic beam-gas scattering. Elastic scattering, by its very definition, can only contribute to the generation of off-amplitude particles as only the trajectory is changed when scattering off a gas molecule. Beam particles scattered off gas molecules through inelastic scattering causes off-momentum and also large betatron amplitude particles. Inelastic scattering can also occur via the collision of beam electrons with atomic electrons. The degree to which beam-gas scattering contributes to the overall halo population depends not only on the atomic composition of the residual gas, but also on its pressure.

Although one of the driving philosophies behind building a linear collider is to avoid the SR issues accompanying circular accelerators, the ILC design will not be able to completely avoid this. A certain number of chicanes are to be included in the baseline design as they are vital for beam diagnostics and energy collimation. SR can be generated in these chicanes as well as in straight section magnets – such as quadrupoles during the focusing and defocusing of the beam. The momentum loss that a particle experiences when radiating a synchrotron photon can be sufficient to cause it to deviate from the main core of the beam.

At operating temperatures the beam pipe is a black body radiator that emits thermal photons. Beam particles can interact with these photons through simple Compton Scattering. Interactions between the particles that populate the core beam (e.g. intra-beam scattering) can lead to scattering that contributes towards the halo. However, the halo contribution from this source is expected to be low.

3.1.2 Optical Influences

Magnetic field conditions along the beam-line can lead to the generation of beam halo. Studies for halo sources for the Next Linear Collider (NLC) estimated that relatively small magnet imperfections are unlikely to give a significant enough kick to drive a core particle to the halo [20]. Beam halo from large multipole errors were seen to be removable by minor adjustments to post-linac collimators. However, existing halo particles will be susceptible to any non-linearities – leading them to be driven to higher amplitudes, which in turn can increase the strain on the collimation system further downstream.

Improper alignment of accelerator components can cause the beam particles to become incorrectly focused or to become out of phase with the core beam population. Misalignment could come from several sources including incorrectly positioned elements and ground vibrations.

3.1.3 Miscellaneous Sources

Particles that are not perfectly dealt with by physical insertions such as spoilers, absorbers, and masks can add to the halo population. The particles can undergo multiple scattering within the material of the insertion and can also initiate electromagnetic showers. Unchecked, the resulting particle debris can add to the beam halo. An overview of the use of spoilers and absorbers in particle collimation is given in chapter 8.

The charged beam is sensitive to the shape of – and the distance from – the walls of the beampipe. As a particle passes through an aperture of, for example, a collimator its charge is mirrored within the conductive material. In the case of intra-bunch wakefields the mirror charge can give a kick to other particles within the same bunch – which due to the build up of charge from the front of the bunch usually has a larger effect on the tail of the bunch. Inter-bunch wakefields depend on the bunch separation and the geometry of the material containing the mirror charge. The cumulative mirror charge from the lead bunch can give rise to a kick to the following bunches. In both cases the kick given by the mirror charge depends on the shape of the aperture and the resistance of the material. The wakefield kick to a given particle could cause it to deviate from the core of the beam, thereby adding to the halo content.

3.2 Synchrotron Radiation

Although the SR issues in circular electron/positron accelerators have provided some of the motivation for designing a linear collider (see section 2.2), this does not rule out the significant contribution of this process to the background in the detector region. Although SR can be generated along the entire BDS, it is the radiation produced from halo particles – especially in the final doublet – which dictates collimation performance requirements.

Uncollimated halo particles arriving at the final doublet will be subjected to the strong focusing and defocusing fields of these last few magnets. By their very definition these particles will be off momentum and/or greatly off axis when traversing the final focus magnets and as such will be greatly deflected, resulting in the emission of SR, Fig. 3.1. This is in addition to the radiation generated by the core of the beam itself. Therefore the depth of halo scraping which the collimators must minimally achieve can be easily defined as that which reduces the spatial distribution of the SR in the IR such that it can pass through every aperture unperturbed. In this way the contribution to backgrounds from SR should be reduced such that only secondary back-scattering from further downstream need be a concern. Backscattering and halo collimation depth studies are described in more detail in sections 7.4 and 7.3 respectively.

3.3 Beamstrahlung

The crossing of densely populated bunches at the interaction point gives rise to a beam-beam phenomena known as beamstrahlung. Due to the bunches carrying strong collective electromagnetic fields, their crossing at the interaction point gives rise to the radiation of photons as the beam particles undergo a certain amount of bending within these fields. This leads to a tight cone of relatively high powered photons leaving the detector region alongside the post-collision bunches. Although this beamstrahlung cone does not directly add to the detector backgrounds, some care must be taken in order to collimate or extract it to a specifically designed dump such that secondary particles are not produced and inadvertently back-scattered to the Vertex Detector – which would have a direct line of sight to any downstream beamstrahlung photon scattering point.

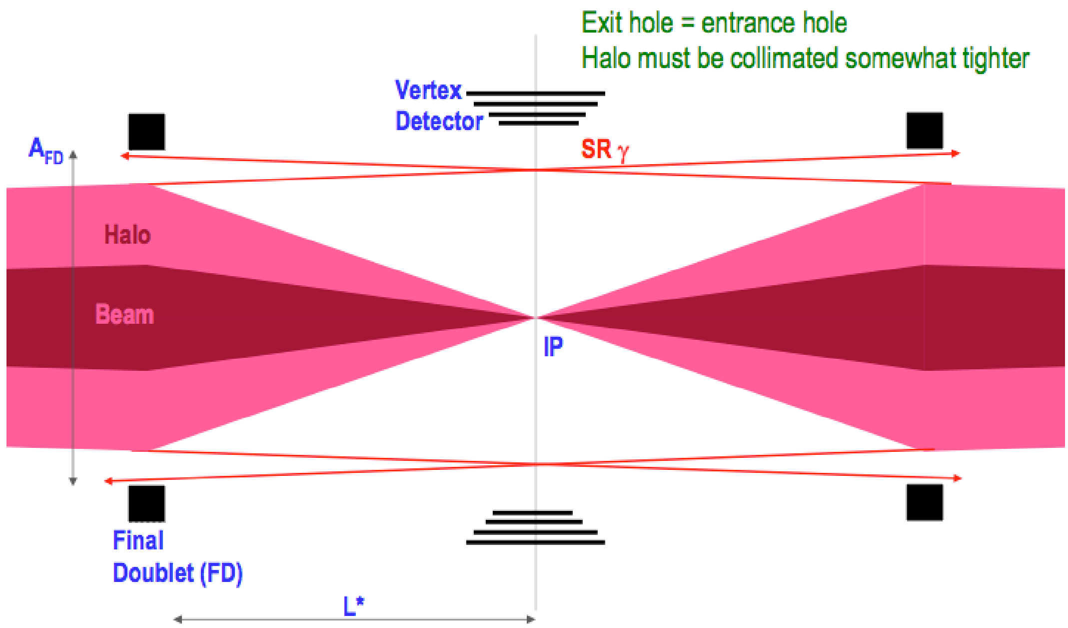

Figure 3.1: Schematic overview of SR production from halo passing through the final doublet for a simple head-on scenario [21].

An important side effect of the resulting energy loss via beamstrahlung is the increase in spread of the centre of mass beam energy. Large energy spreads can potentially decrease the accuracy of mass measurements achievable by threshold scans. Luminosity monitors close to the interaction point should therefore be used to measure this effect in order to reduce its impact on precision physics experiments.

3.4 Pair Backgrounds

Low energy pairs are created in the detector region by the collision of two photons. There are three different processes (see Fig. 3.2) that can lead to the creation of the low energy pairs:

- Breit-Wheeler: two real incident photons, for example from Beamstrahlung.
- Bethe-Heitler: the interaction between one real and one virtual photon.
- Landau-Lifshitz: two virtual incident photons.

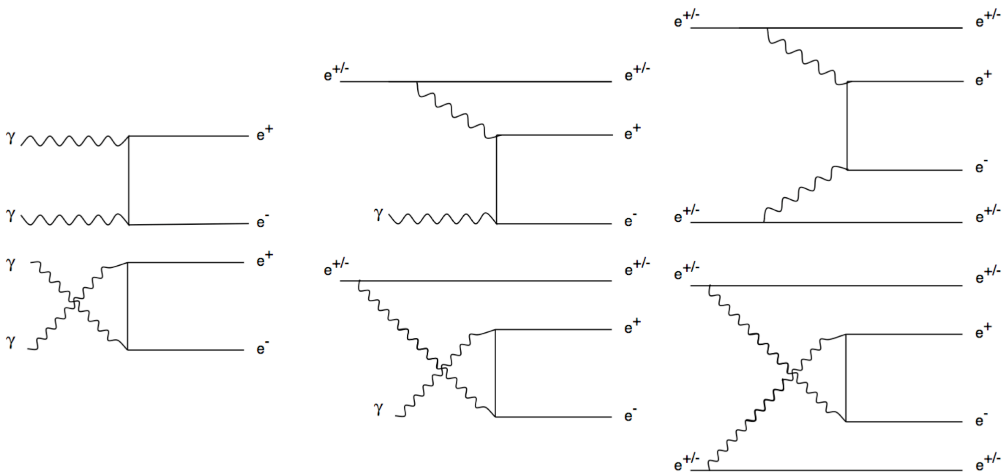

(a) Breit-Wheeler (b) Bethe-Heitler (c) Landau-Lifshitz

Figure 3.2: Low energy pair creation processes.

These low energy electrons and positrons tend to move in the solenoid detector field following a helical path. From a detector background point of view this can cause problems as they are more likely to hit masks and apertures and back scatter to the sensitive detector components such as the vertex detector. As the closest sensitive component to the IP, the vertex detector's minimum inner radius is determined by the opening angle of the low energy pairs. The number of hits on the vertex detector must be minimised such that the hit density does not cause intolerable radiation damage or adversely affect vertex reconstruction.

3.5 Radiative Bhabhas

During the beam-beam collisions an individual particle can undergo bremsstrahlung and emit a photon as a result of interacting with the field of a second particle, Fig. 3.3a. This process of energy loss results in a continuous spectrum of degraded beam particles as illustrated by Fig. 3.3b. In the case of an electron-positron collider a complete range of low energy particles are produced at the interaction point and are collectively referred to as "radiative Bhabhas".

A result of the small transverse beam sizes at the ILC leads to a phenomenon known as the beam-size effect - whereby the virtual photons are suppressed. When the transverse momentum of a virtual photon is significantly small, the impact parameter can become greater than the transverse size of the beam and therefore lead to a reduction in the bremsstrahlung cross-section. The smallness of the transverse beam size at the ILC makes this effect especially important when simulating radiative Bhabha productions. This was first noticed during observations of photon production in the process $e^+e^- \rightarrow e^+e^-\gamma$ in experiments at the MD-1 detector on the VEPP-4 collider [22].

The radiative Bhabhas in the ILC leave the interaction point highly polarised in the direction of the original beams; with electrons travelling in one direction and the positrons in the other. The particles therefore exit the detector region along the same path as the extracted beams. Although the extraction lines are designed to handle particles with a large energy spread as would be expected from a post-collision bunch, it is not possible to fully account for the entire range of energies presented by the radiative bhabhas. The trajectories of the particles forming the low energy tail of the spectrum of radiative bhabhas

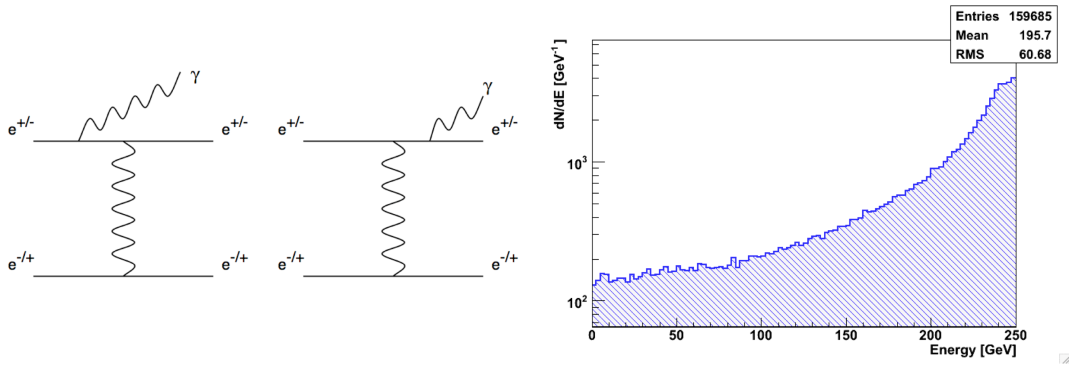

(a) Feynman diagrams

(b) Energy spectrum for radiative Bhabhas produced in the positive Z direction as a result of the collision of 250 GeV nominal parameter beams. Spectrum produced using Guinea-Pig generated events.

Figure 3.3: Radiative Bhabha Feynman diagrams and typical energy spectrum

can be heavily deflected in the strong focusing fields of the final doublet magnets situated adjacent to the detector region, Fig. 3.4. The apertures of most of the magnets can be enlarged to handle the majority of the spread of the particles. However, large energy deposits in the first quadrupole (QD0) are unavoidable. Due to its superconducting nature this magnet has very strict limits on the localised power loads that can be tolerated during operation. Detailed studies of these power loads are given in section 7.5.

3.6 Muon Backgrounds

Beam particles striking the collimators and apertures in the BDS can produce muons from a variety of processes [24], however the Bethe-Heitler process ($\gamma Z \rightarrow Z\mu^+\mu^-$) is expected to be the dominant production mechanism. The muons are hard to stop and due to the inherent nature of the tunnel layout they are guided towards the main detectors. Reducing the large muon flux to a tolerable level in terms of detector backgrounds and personal pro-

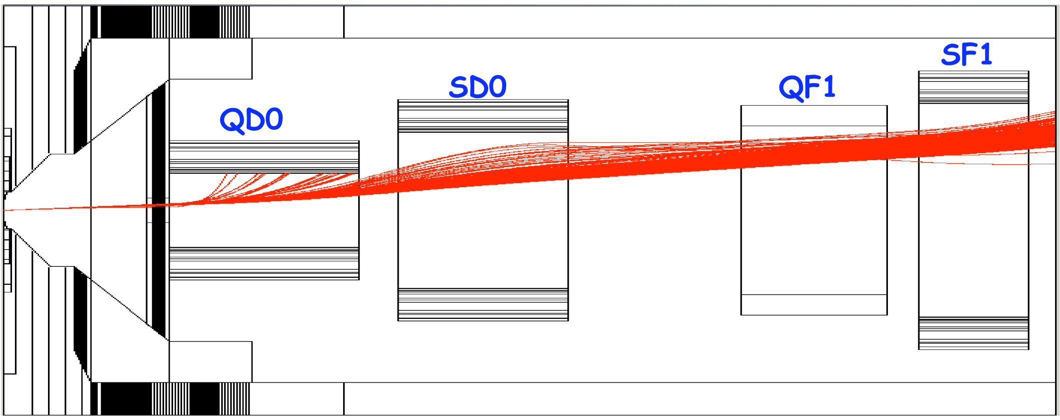

Figure 3.4: Simulated tracks of Radiative Bhabhas in the 2 mrad extraction line [23].

tection requires the use of thick magnetised iron spoilers along the delivery line. Recent studies have shown that the muon flux entering the detector region can be reduced from 4.1 $cm^{-2}s^{-1}$ to 1.2×10^{-3} $cm^{-2}s^{-1}$ with the installation of muon spoilers [25].

3.7 Neutron Backgrounds

Neutrons can cause a considerable amount of background and radiation damage to the detector components. They can be produced along the entire BDS and within the IR by a variety of processes – inferring a large number of possible sources. Some key neutron sources include the high power beam dumps and also e^+/e^- pairs from beamstrahlung within the IR itself. It should also be noted that the use of muon spoilers is also a contributor to the neutron background incident on the IR [25].

Chapter 4

ILC Design

The operating energy range and deliverable luminosity promised by the ILC will present an excellent opportunity to investigating new regions of physics. In order to achieve its full potential the ILC will require a very complex and involved design process on a global scale. In this respect the ILC effort has made significant advancements with key technology decisions and a definite road map already set out. This thesis marks the first real use of accelerator and detector descriptions being modelled and simulated in a single code framework – with the results being used as key factors in the design decision process [26]. This chapter outlines the overall design of the ILC and describes the baseline configuration document.

4.1 Generic Layout of a Linear Collider

The design for a linear collider such as the ILC can be described in a modular fashion with each section having a specific task essential to the overall operation of the machine. The basic layout is as illustrated in Fig. 4.1, where the beam is created as a relatively low energy source and is accelerated to a damping ring to reduce its initial emittance. The beam's energy is then increased in the linear acceleration (linac) section before being transported to the interaction point (IP) via the BDS. Post IP, the beam is guided to the dump by an extraction line. The gross length for each half of the linear collider is approximately 15 km – where the majority of this is dominated by the length of the linac. The total length of the linear collider, including both electron and positron lines, is therefore expected to be approximately 30 km.

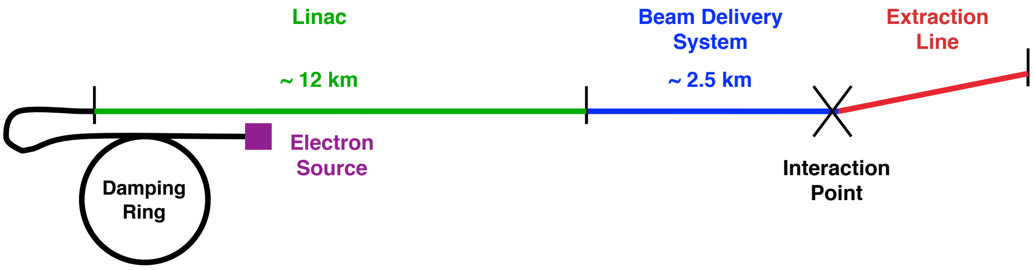

Figure 4.1: Generic layout for a linear collider – showing only the (electron) source to interaction point sections for one beam.

4.1.1 Electron Source

Generic LC System

Laser-driven electron guns are used to produce photoelectrons via the photoelectric effect by firing a laser onto a photocathode. Once produced, the electron beam is passed through a bunching system and then pre-accelerated for injection into the damping ring.

ILC Specific

The ILC electron guns must be able to meet the design requirements of more than 80% polarisation. In these systems a laser is fired at a photocathode material such as GaAs or Cs_2Te. Extensive R&D is underway for the development of polarised guns [27]; in this particular set up the electron gun will make use of a GaAs photocathode with a DC bias of 120 kV.

4.1.2 Positron Source

Generic LC System

For the production of the positrons the usual method involves producing e^+/e^- pairs by firing electrons or photons onto a target. The positrons are separated from the electrons and then pre-accelerated before entering the damping ring. For the electron/target set up the electrons can be produced using an electron gun; the electrons hit the target and undergo bremsstrahlung to produce photons which subsequently convert to e^+/e^- pairs. The photon/target method uses a thinner target to produce the pairs, allowing for lower initial emittance of the positrons as the amount of Coulomb scattering within the material is reduced. The incident photons can be produced by sending relatively high energy electrons through an undulator.

ILC Specific

Electrons with an energy of 150 GeV will be directed through a 200 m section of undulators in the main electron linac. The intense photons produced are directed onto the positron production target. One disadvantage with this system is that requiring high incident energies means that a proof of concept will be hard to test before construction of the ILC.

A second positron production method using a Laser-Compton source has been suggested as an alternative design option [28]. Focusing a laser across the path of an electron beam produces polarised gamma rays, which are subsequently directed onto a thin target to produce electron-positron pairs. One key advantage of this system would be the independence of the positron system from the main electron linac, potentially allowing for easier development, operation, and commissioning.

4.1.3 Damping Ring

Generic LC System

At injection to the damping rings the transverse beam emittances are large and therefore require significant reduction for the ILC to meet the small spot size requirements. The emittance reduction is achieved due to the fact that the beam will emit SR whilst circulating the damping ring. The direction of this energy emission is along the beam particles' trajectory - concentrated in a cone with an angular width of $\sim 1/\gamma$. The momentum lost by this process is subsequently restored in a controlled manner with an RF cavity that accelerates the beam in the direction of travel. As a result of this energy emission by SR and re-acceleration by RF cavities the transverse emittance of the beam can be reduced.

ILC Specific

The ILC damping rings will be approximately 6.6 km in circumference and will receive the beam from the electron or positron production system at the pre-accelerated energy of 5 GeV. Between the damping rings and the main linac – in the ring to main linac (RTML) section – the beams will undergo bunch compression and are accelerated to the pre-linac requirement of 13-15 GeV.

4.1.4 Main Linac

Generic LC Layout

The main linac is typically the longest section of a linear collider, consisting of accelerating structures, beam instrumentation, and tune up dumps. The length is dominated by the desired collision energy coupled with the accelerating gradient available to achieve this. In addition to the elements listed above, the linac employs the use of a number of focusing magnets (typically arranged in focus-drift-defocus-drift sections, or FODO cells) to help control emission growth.

ILC Specific

Although several methods have been developed to accelerate bunches to the TeV energy scale, it is the superconducting RF technology that will be used in the 12 km linac section of the ILC. For the baseline configuration the linac will be required to accelerate the beam from the input energy of 13-15 GeV to 250 GeV. The electron linac will also contain a single undulator to be used with the positron production system.

4.1.5 Beam Delivery System (BDS)

Generic LC Layout

Once the bunches have been accelerated they are transported to the IR by the BDS. The BDS also provides a multitude of beam diagnostics and feedback systems to ensure that the beams collide as intended. The bunches pass through the post-linac collimators whilst in the BDS, which are used to remove errant particles that may induce backgrounds in the detector or that could cause machine protection issues. After collimation the bunches are focussed to nanometer spot sizes for collision at the IP.

ILC Specific

The ILC design currently caters for a BDS with a beam switch yard that can direct the beam along one of three optics lines: a fast beam dump line for commissioning and machine protection reasons, and delivery lines to two IP crossing angles of 14 mrad. Further details along with collimation studies can be found in chapter 8.

4.1.6 Interaction Region

Generic LC Layout

The two beams collide in the IR after undergoing final focussing by the last few quadrupoles in the BDS. A detector consisting of the calorimeter and tracking components surrounds the IP to record particle collision data. In order to produce usable data it is important that the backgrounds in the IR are well understood and are reduced to a tolerable level.

ILC Specific

The ILC is expected to have two 14 mrad IPs and there are currently several detector concepts with designs for these regions. For reasons of maintenance and protection, the two IR's will be separated transversely by at least 3 m of shielding. A number of background studies in relation to the IR are detailed in chapter 7.

4.1.7 Extraction Line

Generic LC Layout

The post-collision bunches can be highly disrupted and must be safely transported to the high power dumps via the extraction lines. The extraction line contains several diagnostic regions that can be used to provide feedback on the condition that the bunches had when they were at the IP.

ILC Specific

The ILC beams will be of very high powers – up to 18 MW requiring special attention in the designing of the optics and beam dumps. The crossing angle at the IP may necessitate R&D into non-standard magnets due to the proximity of the incoming and outgoing beam lines. Further details and ILC design-related studies can be found in section 8.4.

4.2 Baseline Configuration Document (BCD)

The BCD [28] was introduced by the Global Design Effort (GDE) at the ILC Snowmass workshop in August 2005 to be a totally encompassing document containing the full design parameters and configurations for every aspect of the ILC machine. The document defines the design choices required for building a 500 GeV centre of mass energy machine and includes an upgrade path to 1 TeV. Fig. 4.2 illustrates the overall design of the ILC at the time of writing (October 2006).

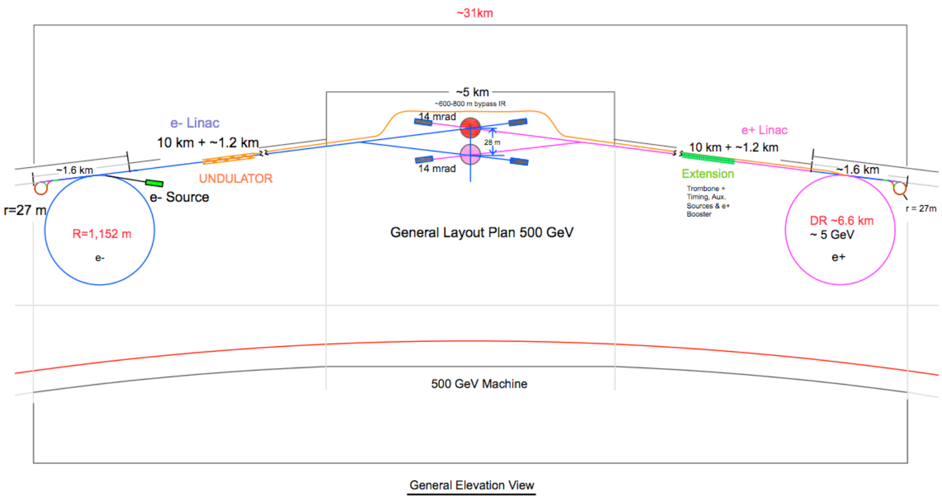

Figure 4.2: Schematic view of the ILC layout [29].

Every choice of technology used in the BCD is supported by extensive R&D to enable the document to be a realistic design that could be built using currently available techniques. The overall structure of the BCD (see Fig. 4.3) is laid out using a number of "nodes", each dealing with distinct areas of the overall design:

- General Parameters
- Electron Source
- Positron Source
- Damping ring
- Ring to Main Linac
- Main Linac
- Beam Delivery
- Cost Engineering
- Conventional Facilities and Siting
- Operations and reliability
- Instrumentation and Controls

Owing to the complexity of the design process, many of the nodes have subsidiary topics that overlap with those of other nodes. Design choices for each node can therefore

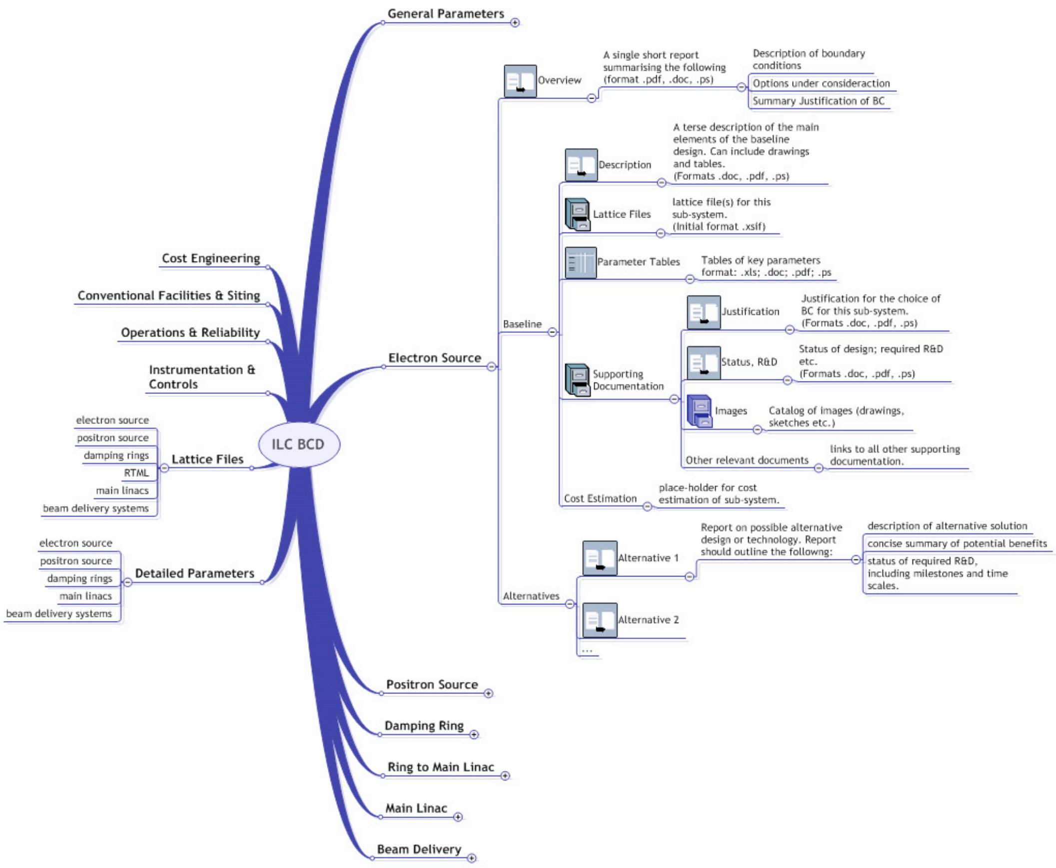

Figure 4.3: Overview of the BCD with an example of the general node structure [29].

rely on the input and decisions from other nodes and working groups. In this way the BCD has developed into a highly iterative document with contributions from collaborations around the world.

4.3 Machine Parameters

The suggested machine parameter sets for both the baseline beam energy of 500 GeV and the upgrade option of 1 TeV are given in Fig. 4.4 and 4.5 [30]. The different parameters given are not necessarily examples of how the machine should be run, but are instead intended to give a realistic range of beam conditions with which to test the flexibility of the various ILC design choices. Each collision energy has 5 beam parameter sets associated with it:

- **Nominal**

  This is the standard beam parameter set used as a reference for the other sets, which help define the operating range of the ILC.

- **Low Bunch Charge (low Q)**

  Bunch charge and separation is halved whilst the number of bunches is doubled. This set would be useful for reducing space charge effects and wakefields, ultimately resulting in decreasing the disruption at the IP.

- **Large Spot (large Y)**

  A larger vertical spot size at the IP leading to higher IP disruption.

- **Low Power (low P)**

  Less than half the number of bunches compared to the nominal case and an increase in bunch separation. A reduction in the spot sizes help recover the lost luminosity in this case.

- **High Luminosity**

  Not part of the baseline parameter sets, but often used as a “worse case” scenario for setting limits of the survivability and operation of components in the ILC.

500 GeV Beam and IP Parameters

	TESLA	USSC	Nominal	Low Q	Large Y	Low P	High Lum
E_cms (GeV)	**500**	**500**	500	500	500	500	500
N	**2.00E+10**	**2.00E+10**	2.00E+10	1.00E+10	2.00E+10	2.00E+10	2.00E+10
Nb	**2820**	**2820**	2820	5640	2820	1330	2820
T_sep (ns)	**336.9**	**336.9**	307.7	153.8	307.7	461.5	307.7
Buckets @ 1.3 GHz	**438**	**438**	400	200	400	600	400
I_ave (A)	**0.0095**	**0.0095**	0.0104	0.0104	0.0104	0.0069	0.0104
Gradient	**23.40**	**28.00**	30.00	30.00	30.00	30.00	30.00
IP Parameters							
gamepsX (m-rad)	**1.00E-05**	**9.60E-06**	1.00E-05	1.00E-05	1.20E-05	1.00E-05	1.00E-05
gamepsY (m-rad)	**3.00E-08**	**4.00E-08**	4.00E-08	3.00E-08	8.00E-08	3.50E-08	3.00E-08
BetaX	**1.50E-02**	**1.50E-02**	2.10E-02	1.20E-02	1.00E-02	1.00E-02	1.00E-02
BetaY	**4.00E-04**	**4.00E-04**	4.00E-04	2.00E-04	4.00E-04	2.00E-04	2.00E-04
SigX	**5.54E-07**	**5.43E-07**	6.55E-07	4.95E-07	4.95E-07	4.52E-07	4.52E-07
SigY	**5.0E-09**	**5.7E-09**	5.7E-09	3.5E-09	8.1E-09	3.8E-09	3.5E-09
SigZ	**3.00E-04**	**3.00E-04**	3.00E-04	1.50E-04	5.00E-04	2.00E-04	1.50E-04
Dx	**2.26E-01**	**2.35E-01**	1.62E-01	7.08E-02	4.68E-01	2.26E-01	1.70E-01
Dy	**2.53E+01**	**2.23E+01**	1.85E+01	1.00E+01	2.86E+01	2.70E+01	2.19E+01
U_ave	**0.054**	**0.055**	0.046	0.061	0.036	0.100	0.133
delta_B	**0.030**	**0.031**	0.022	0.018	0.024	0.057	0.070
P_Beamstrahlung (W)	**3.35E+05**	**3.47E+05**	2.48E+05	2.05E+05	2.67E+05	3.06E+05	7.90E+05
N_gamma	**1.477**	**1.504**	1.257	0.823	1.664	1.756	1.725
Hd_x	**1.061**	**1.069**	1.022	1.002	1.465	1.061	1.026
Hd_y	**5.317**	**5.071**	4.727	3.764	3.211	4.142	5.037
Hd	**1.80E+00**	**1.78E+00**	1.70E+00	1.56E+00	1.79E+00	1.65E+00	1.74E+00
Geometric Luminosity	**1.64E+38**	**1.45E+38**	1.20E+38	1.29E+38	1.12E+38	1.24E+38	2.83E+38
Luminosity ($m^{-2}s^{-1}$)	**2.94E+38**	**2.57E+38**	2.03E+38	2.01E+38	2.00E+38	2.05E+38	4.92E+38
Coherent pairs/bc	**7.14E-35**	**4.65E-34**	7.71E-43	4.29E-31	3.19E-56	3.31E-15	2.21E-09
Inc. Pairs/bc	**4.14E+05**	**3.66E+05**	2.59E+05	8.37E+04	3.50E+05	6.12E+05	6.37E+05

Figure 4.4: Beam and IP parameters for 500 GeV centre of mass energy .

1 TeV Beam and IP Parameters

	TESLA	**USCS**	**Nominal**	**Low Q**	**Large Y**	**Low P**	**High Lum**
E_cms (GeV)	**800**	**1000**	1000	1000	1000	1000	1000
N	**1.40E+10**	**2.00E+10**	2.00E+10	1.00E+10	2.00E+10	2.00E+10	2.00E+10
Nb	**4886**	**2820**	2820	5640	2820	1330	2820
T_sep (ns)	**175.4**	**336.9**	307.7	153.8	307.7	461.5	307.7
Buckets @ 1.3 GHz	**228**	**438**	400	200	400	600	400
I_ave (A)	**0.0128**	**0.0095**	0.0104	0.0104	0.0104	0.0069	0.0104
Gradient	**35.00**	**35.00**	30.00	30.00	30.00	30.00	30.00
IP Parameters							
gamepsX (m-rad)	**8.00E-06**	**9.60E-06**	1.00E-05	1.00E-05	1.20E-05	1.00E-05	1.00E-05
gamepsY (m-rad)	**1.50E-08**	**4.00E-08**	4.00E-08	3.00E-08	8.00E-08	3.50E-08	3.00E-08
BetaX	**1.50E-02**	**2.44E-02**	3.00E-02	1.50E-02	1.10E-02	1.20E-02	1.00E-02
BetaY	**4.00E-04**	**4.00E-04**	3.00E-04	2.00E-04	6.00E-04	2.00E-04	2.00E-04
SigX	**3.92E-07**	**4.89E-07**	5.54E-07	3.92E-07	3.67E-07	3.50E-07	3.20E-07
SigY	**2.8E-09**	**4.0E-09**	3.5E-09	2.5E-09	7.0E-09	2.7E-09	2.5E-09
SigZ	**3.00E-04**	**3.00E-04**	3.00E-04	1.50E-04	6.00E-04	2.00E-04	1.50E-04
Dx	**1.98E-01**	**1.45E-01**	1.13E-01	5.67E-02	5.09E-01	1.89E-01	1.70E-01
Dy	**2.80E+01**	**1.75E+01**	1.79E+01	8.96E+00	2.67E+01	2.47E+01	2.19E+01
U_ave	**0.086**	**0.123**	0.109	0.154	0.081	0.257	0.376
delta_B	**0.042**	**0.061**	0.050	0.044	0.060	0.134	0.178
P_Beamstrahlung (W)	**7.33E+05**	**1.38E+06**	9.02E+05	8.03E+05	1.09E+06	1.15E+06	3.21E+06
N_gamma	**1.433**	**1.601**	1.429	0.987	2.163	2.109	2.220
Hd	**1.80E+00**	**1.68E+00**	1.52E+00	1.54E+00	2.02E+00	1.61E+00	1.74E+00
Geometric Luminosity	**2.81E+38**	**2.27E+38**	1.85E+38	1.85E+38	1.40E+38	1.81E+38	4.54E+38
Luminosity ($m^{-2}s^{-1}$)	**5.07E+38**	**3.81E+38**	2.82E+38	2.84E+38	2.81E+38	2.92E+38	7.88E+38
Coherent pairs/bc	**3.15E-19**	**6.80E-11**	1.92E-13	8.39E-08	2.03E-20	9.91E-01	8.18E+02
Inc. Pairs/bc	**4.66E+05**	**5.01E+05**	4.32E+05	1.50E+05	6.67E+05	1.10E+06	1.36E+06

Figure 4.5: Beam and IP parameters for 1 TeV centre of mass energy .

Chapter 5

Laser-wire Project

To meet the luminosity goal of 10^{34} m^{-2}s^{-1} the ILC aims to deliver high power electron and positron beams, resulting in collisions with spot sizes of approximately 5 nm vertical by 200 nm horizontal. To achieve these performance targets the beams must be heavily monitored throughout the acceleration and delivery phases with the diagnostic results utilised in feedback systems for controlling and modifying the beam properties. In many respects the ILC beam conditions will be more stringent and harder to measure than at any previous e^+/e^- facility. In view of this a significant amount of R&D must be invested into beam diagnostic techniques. Beam profile and emittance measurements are essential parts of the ILC diagnostic system. This chapter describes the underlying principles for one such system – the Laser-wire project – and details the studies conducted throughout its development stages.

5.1 Emittance

The standard method for monitoring the development of a particle beam along the length of the collider is to measure the advancement of its transverse phase space. This phase space is defined by the angular and positional transverse components of each particle within a given bunch and usually takes the form of an ellipse in the (x,x') or (y,y') planes as illustrated by Fig. 5.1. The area - or more precisely Area/π - enclosed by the ellipse is referred to as the emittance (ε_x and ε_y) of the beam. According to Liouville's Theorem, the emittance of a beam is invariant in the absence of components that modify the beam's energy [7]. This is the case in the BDS where the beam energy is constant (neglecting the effect from emission of SR) and the particles only pass focusing and bending magnets.

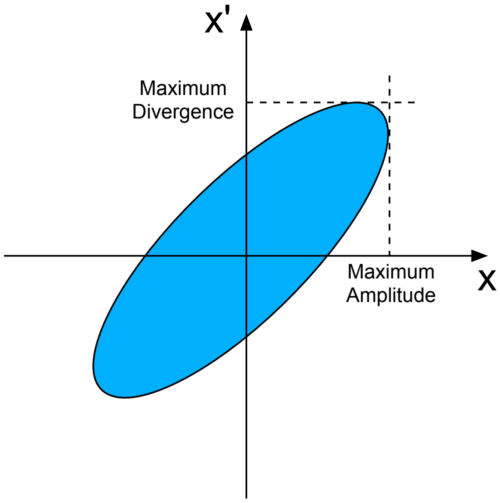

Figure 5.1: Phase space ellipse in the (x, x') plane. The (shaded) area enclosed by the ellipse is equivalent to the emittance of the particles forming the ellipse.

The transverse focusing of the BDS components is measured by the betatron function (β_x and β_y). It follows that the transverse profile of the beam at a given location in the BDS is proportional to both the betatron function at that point and also the (invariant) emittance. In terms of luminosity delivered at the IP it is useful to define the collision spot size $\sigma^*_{x,y}$ – assuming zero divergence – as:

$$\sigma^*_{x,y} = \sqrt{\varepsilon_{x,y}\beta^*_{x,y}} \tag{5.1}$$

where $\beta^*_{x,y}$ is the betatron function at the IP. By substituting Equation 5.1 into Equation 2.3 it is possible to produce an emittance dependant relation for the luminosity:

$$\mathcal{L} = f \frac{N_1 N_2}{4\pi \sqrt{\varepsilon_x \beta_x^*} \sqrt{\varepsilon_y \beta_y^*}} H_D \tag{5.2}$$

To deliver high luminosity the ILC will have small IP spot sizes, requiring low transverse emittances. It is therefore important that real-time information on the emittance and quality of the beam is gathered along the BDS to help maximise the luminosity.

5.1.1 Phase Space Evolution

The properties of the optics lattices used in the BDS are typically characterised by the transformation of the phase space of the transported beam. Expanding upon the previous emittance discussions, it is possible to enhance the phase space schematic given in Fig. 5.1 to that of Fig. 5.2.

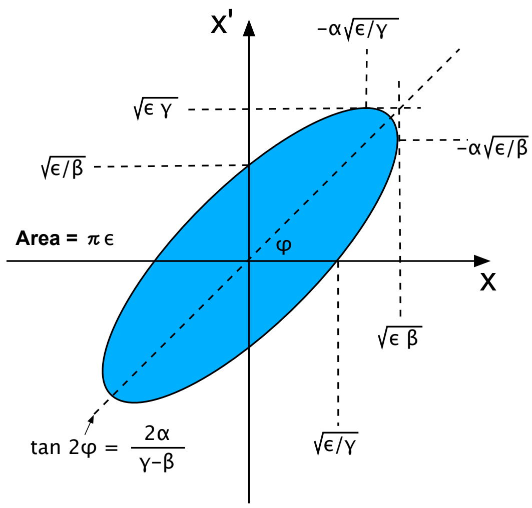

Figure 5.2: Phase space ellipse [8].

The parameters α, β, and γ are used to define the shape and orientation of the ellipse, whilst the emittance ε corresponds to the area. Although the area is invariant during transportation along a constant energy beam-line, the shape and orientation of the phase space continuously changes. This suggests that α, β, and γ are in fact functions with respect to position along the length of the beam-line and are known as betatron functions. Since all particles enclosed by the ellipse are bound by that ellipse, knowledge of the betatron functions at any given point along the beam-line allows for the complete description of the beam at that point. A full review of the betatron functions and their use in describing the beam in an optics lattice can be found in [8].

5.1.2 Measuring the Emittance

As a combination of both the beam's angular divergence and transverse size the emittance is not a property of the beam that is readily measured directly. A typical method of inferring the beam emiitance therefore involves taking various measurements of the beam size. However, measurements performed at a single location do not allow for a full understanding of the shape and rotation of the phase space ellipse. Obtaining this information requires the beam profile to be monitored at several stages along the beam line with different advances in the betatron phase as illustrated by Fig. 5.3. By observing how the phase space propagates between each monitoring station it is possible to reconstruct the emittance.

Current techniques for measuring the transverse dimensions of a beam typically involve passing a solid wire through the beam. Particles scattered as a result of this can be collected downstream and counted according to the wire's position. In this way the width of a beam can be discerned, albeit at a cost of temporary disruption to the beam that is unacceptable in a single pass machine such as the ILC. The solid wire technique is also limited in resolution by the requirement that the thickness of the wire must be less than the width of the beam. With spot sizes in the ILC BDS typically in the low micrometer range this requires a thickness of wire that would not be able to withstand the power of the beam without being destroyed.

The beam conditions at the ILC have therefore introduced the requirement for R&D into beam profiling techniques that are able to:

- Resolve beam sizes of a few micrometers with a resolution error of less than 10%.
- Survive under high power beam conditions.

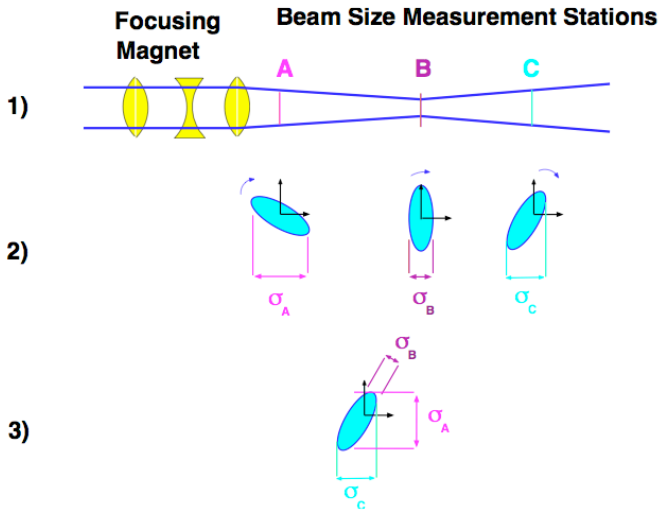

Figure 5.3: Multi-station emittance measurements. The beam size is measured at several locations along the beam line. The emittance can then be reconstructed from these measurements by accounting for how the phase space is expected to propagate along the given section of beam line. [31].

- Operate non-invasively to allow continuous measurements.
- Operate fast enough to provide information on bunches within a train (intra-train scanning).

Replacing solid wires with laser-based scanning techniques has been suggested as a possible solution to meet these goals [32]. The Laser-wire project discussed in the following sections is a beam profiling system that aims to monitor the electron beam at numerous beam-line locations with at least two different transverse profiles. As well as obtaining emittance measurements in the BDS, the use of Laser-wires within the main linac has been suggested in terms of a feedback system for emittance optimisation [33]. In this scheme an emittance tuning 'bump' is introduced to the beam line as an arrangements of magnets such that dispersion or wakefield kicks are generated in a controlled manner. Two Laser-wire monitor stations separated by a betatron phase advance of 90° are located at the end of the linac to measure the beam emittance before entry to the BDS.

The emittance can be tuned (i.e. minimised) by altering the dispersion or wakefield kicks at the tuning bumps.

5.2 Laser-wire Concepts

The underlying principle of the Laser-wire project is to scan focused laser light across the path of the electron[1] bunch. This produces Compton-scattered photons (and degraded electrons) that can be detected further downstream. As illustrated in Fig. 5.4, a single high powered laser can be used to scan both horizontal and vertical profiles by splitting the laser light accordingly.

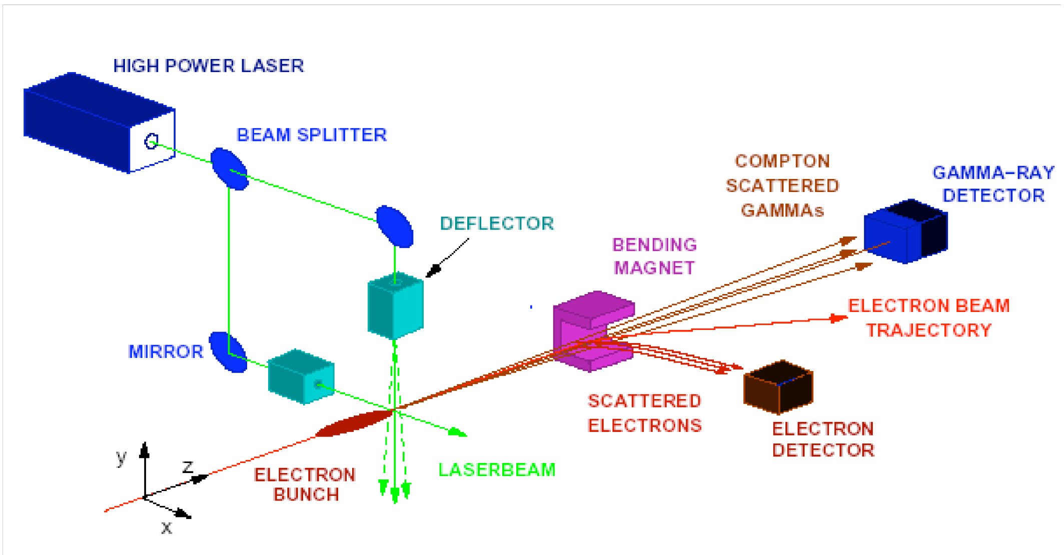

Figure 5.4: Schematic of the Laser-wire project

With their trajectories unaffected by magnetic fields, the scattered photons can be detected after the main beam has passed a bending field. The degraded electrons are generally lower in energy than the main beam and so their trajectories are bent to a greater degree. It is however more challenging to detect these particles as they have a wide range

[1]this chapter discusses the Laser-wire project referencing only electrons. The technique is equally applicable to positrons

of energies, leading to a large angular spread after the bending fields and hence detector positioning becomes difficult. For this reason the Laser-wire project has concentrated on detecting the Compton-scattered photons.

5.2.1 Compton Scattering

The relativistic electrons within the main beam scatter off the laser photons via the inverse Compton Scattering process: $e^{\pm} + \gamma \rightarrow e^{\pm} + \gamma$. As discussed in [32], the cross-section (σ_c) for Compton-scattered electrons in terms of the Thomson scattering cross-section ($\sigma_t = 6.65 \times 10^{-25}$ cm^2) is:

$$\frac{\sigma_c}{\sigma_t} = \frac{3}{4}\left[\frac{1+\varepsilon}{\varepsilon^3}\left(\frac{2\varepsilon(1+\varepsilon)}{1+2\varepsilon} - \ln(1+2\varepsilon)\right) + \frac{1}{2\varepsilon}\ln(1+2\varepsilon) - \frac{1+3\varepsilon}{(1+2\varepsilon)^2}\right] \tag{5.3}$$

where ε is the energy of the incident laser photon normalised to the rest frame of the electron. Up to a maximum photon energy, $\omega_{max} = \frac{2\varepsilon E_{beam}}{1+2\varepsilon}$, the energy spectrum of the scattered photons is given by:

$$\frac{d\sigma_c}{d\omega} = \frac{3\sigma_t}{8\varepsilon}\left[\frac{1}{1-\omega} + 1 - \omega + \left(\frac{\omega}{\varepsilon(1-\omega)}\right)^2 - \frac{2\omega}{\varepsilon(1-\omega)}\right] \tag{5.4}$$

where ω is the energy of the Compton-scattered photon normalised to the rest frame of the electron. Typical energy spectra for scattered photons based on a variety of beam energies and laser wavelengths are given in Fig. 5.5.

The angular distribution of the emitted photons is generally confined to be within a cone with a half-angle a few times the critical angle, α_c:

$$\alpha_c = \frac{\sqrt{1+2\varepsilon}}{\gamma} \tag{5.5}$$

5.2.2 Obtaining a Beam Size Measurement

The gaussian waist of the laser is focused to a sufficiently small size to enable enough scan points through the electron bunch to resolve its profile. Assuming that both the laser

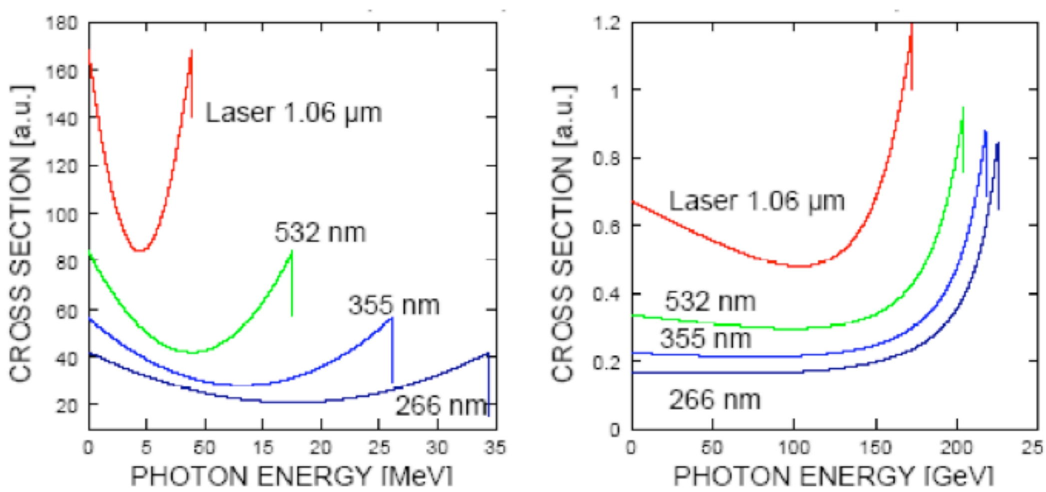

(a) (b)

Figure 5.5: Energy spectra for Compton-scattered photons based on four laser wavelengths and with electron beam energies of a) 1 GeV and b) 250 GeV

and electron pulses are gaussian, the expected number of photons per laser/electron pulse crossing can be given as [32]:

$$N_\gamma = N_b \frac{P_L \sigma_c}{ch\nu_0} \frac{1}{\sqrt{2\pi}\sigma_s} \exp \frac{-y^2}{2\sigma_s^2} \tag{5.6}$$

where N_b is the number of electrons, P_L is the power of the laser, ν_0 is the frequency of the laser light, y is the transverse position of the laser waist with respect to the centre of electron bunch, and the overlap region of the laser waist and electron bunch is given by $\sigma_s^2 \equiv \omega_0^2 + \sigma_y^2$. The peak number of Compton-scattered photons for a given set of laser and electron beam parameters occurs at the central overlap position of $y = 0$. The total detected energy of the Compton-scattered photons as a function of the laser's scan position can be used to infer the size of the beam, Fig. 5.6.

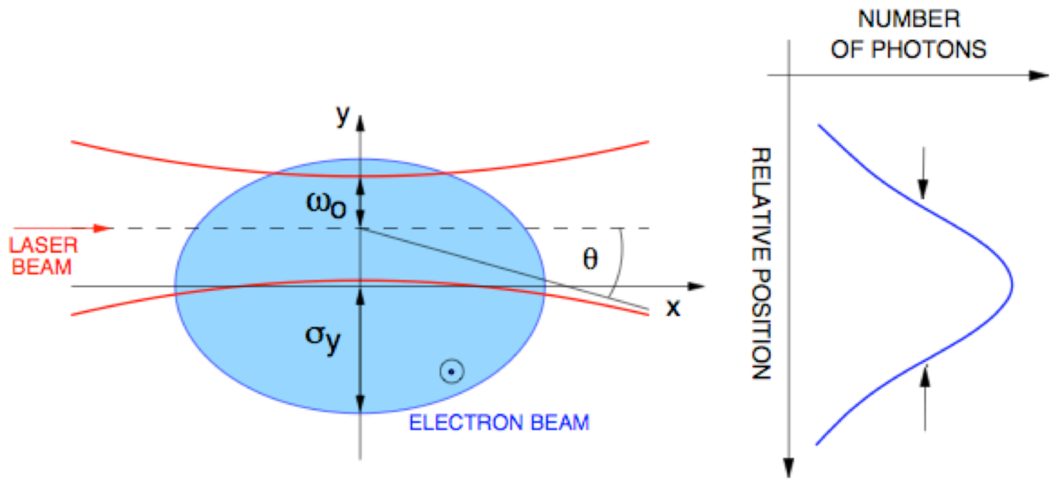

Figure 5.6: Schematic of how the laser overlap with the electron bunch, and hence scan position, can be used to recreate the gaussian profile of the electron bunch [34]. σ_y is the size of the electron beam, and ω_0 is the waist of the laser pulse – the minimum of which is limited by the diffraction θ as $\omega_0 = \frac{\lambda}{\pi\theta}$

5.3 Project Overview

To experimentally test the feasibility and evaluate the performance of a laser based system as described above requires the use of an electron beam with similar properties to those expected in the ILC BDS. The use of the PETRA (Positron Electron Tandom Ring Accelerator) electron storage ring at the DESY (Deutsches Elektronen-Synchrotron) facility was proposed [35] as this is able to provide a beam size of 10 to 100 μm. PETRA has a lower operating energy ($E_{max} \approx 12$ GeV) than the expected ILC conditions, but this is convenient during the commissioning phase of the Laser-wire project. The PETRA machine parameters relevant to the Laser-wire project are given in Table 5.1. The experiment location at PETRA (see Fig. 5.7) was chosen as it had the advantage of a straight beam-line section with an existing access pipe to the tunnel allowing the laser to be operated from outside the radiation environment and guided safely to the PETRA beam-pipe.

Table 5.1: PETRA machine parameters

Energy, E	4.5 to 12	GeV
Bunch Length, σ_z	20 to 100	ps
Charge per Bunch	1 to 3	nC
Horizontal Beam Size, σ_x	100 to 300	μm
Vertical Beam Size, σ_y	10 to 100	μm
Circumference	2.3	km
Beam Lifetime	$\sim$ 10	hours

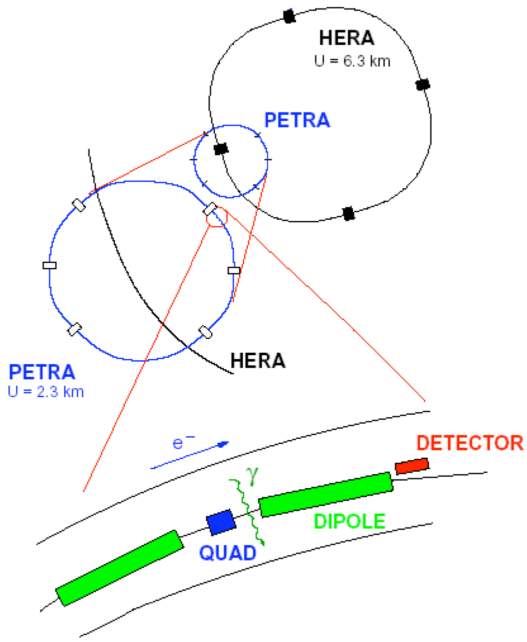

Figure 5.7: Location of the Laser-wire project on the PETRA storage ring at DESY.

5.3.1 Experimental Set Up

A schematic of the experimental set up at PETRA is shown in Fig. 5.8. The Laser-wire project was supplied with a Q-Switch Nd:YAG laser that had been decommissioned from the LEP polarimeter . The laser operates with a repetition rate of 30 Hz at 532 nm, with a measured power output of 1.46 MW, and an average pulse length of 10 ns. The laser is triggered by purpose-built hardware with timing derived from the PETRA bunch and revolution clocks. The laser is transported to the electron beam-line and focused to a waist size of 80 μm. Scanning of the laser across the electron bunch is accomplished with a piezo operated scanning mirror – however during the early testing of the Laser-wire concept only the vertical scan was implemented.

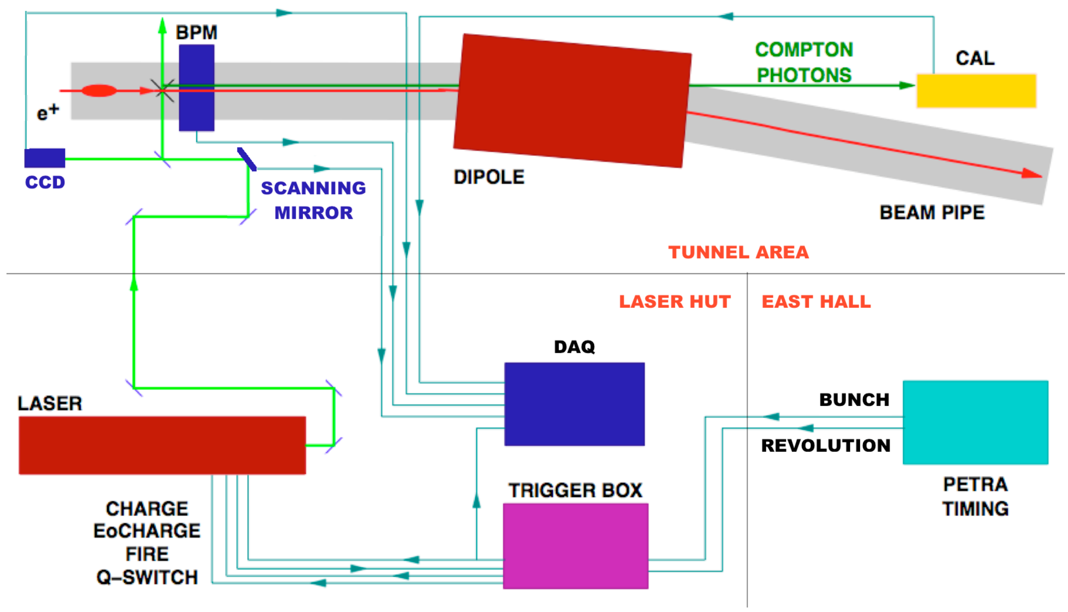

Figure 5.8: Schematic of the Laser-wire experiment at the PETRA storage ring at DESY.

Diagnostics on laser spot size are provided by a charge coupled device (CCD) camera located next to the beam-line. Details of the CCD set up and signal analysis can be found in [36]. A PETRA beam position monitor (BPM) located next to the laser/electron IP is used to ensure that the electron bunch and laser waist are correctly aligned spatially for the scanning. A more detailed description of the hardware-software integration carried out for the Laser-wire project can be found in [37].

The Compton-scattered photons are collected in a calorimeter shortly after being separated from the main PETRA beam (and degraded electrons) by a dipole magnet. The calorimeter consists of a 3×3 matrix of $18 \times 18 \times 150$ mm lead tungstate ($PbWO_4$) crystals connected to a single photomultiplier tube (PMT) with optical grease. A comprehensive report of the development and commissioning of the Laser-wire calorimeter can be found in [31].

All the hardware in the experiment uses purpose-written software controllers, all of which are controlled by a central data acquisition (DAQ) system. This system transmits vital timing information to each component to ensure the synchronisation of the trigger and the data collecting hardware. The DAQ software also polls every software element for experimental data and collates it accordingly.

5.4 First Experimental Results

During the commissioning phase of the project the first goal was to obtain a steady signal from the detector at maximum laser/electron pulse overlap. The first conclusive Compton-scattered photons were detected in the early stages of the project shortly after the introduction of the BPM visualisation software [37]. The original signal from the digital scope is shown in Fig. 5.9.

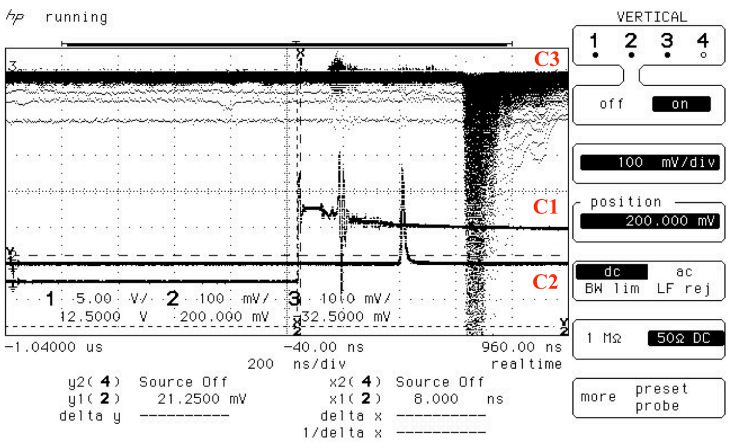

Figure 5.9: First Laser-wire signal obtained for Compton-scattered photons. The scope channels are identified as: C1 – laser trigger; C2 – photodiode at the laser/electron IP, used to check the arrival time of the laser light; C3 – detector signal.

Following the discovery of the first signal, long data runs were taken at the point of laser/electron maximum overlap, Fig 5.10. For these runs the PETRA beam energy was at 7 GeV and both low (1 mA) and high (5 mA) electron bunch current was used.

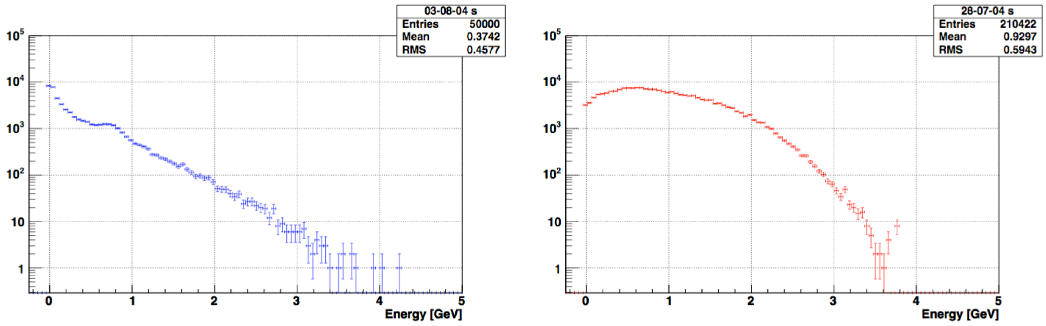

(a) (b)

Figure 5.10: Laser-wire signals at maximum laser-electron overlap for two bunch currents: a) 1mA and b) 5 mA.

Based on the above experimental parameters and assuming that the vertical beam size is within the PETRA machine parameter range, the expected number of Compton-scattered photons from Equation 5.6 is 115 to 184 for a 1 mA bunch current. The expected Compton-scattered photon energy spectrum for the PETRA Laser-wire experiment is given in Fig. 5.11. This spectrum indicates a maximum photon energy of 0.78 GeV and a mean value of 0.38 GeV. A mean total energy incident on the calorimeter of $115 \times 0.38 = 43.7$ GeV should therefore be observed. Fig. 5.10a shows no evidence of energies of this magnitude, however a peak at $\sim$0.8 GeV can be seen. This is an indication that single photons with the maximum energy are arriving at the detector. The accompanying tail reaches $\sim$4 GeV, suggesting that on occasion a few photons at a time are detected.

A profile scan of the electron bunch was achieved by using the piezo scanning mirror in the laser optics to move the laser waist position vertically through the electron bunch [38]. The scan was done in steps, collecting 5000 events at each of 20 locations. With a laser repetition rate of 30 Hz each scan point took 3 minutes giving an overall time of 60 minutes for an entire profile measurement. A Gaussian fit on the measurement data

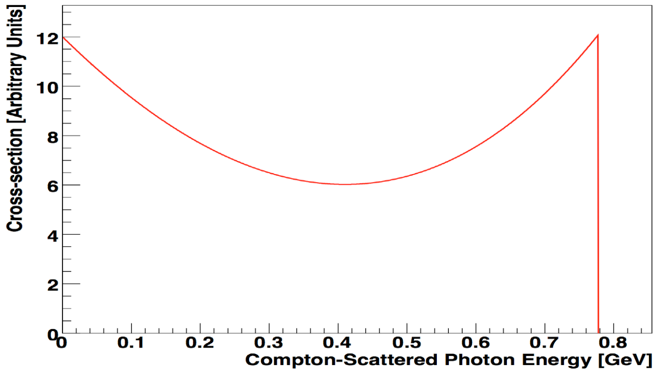

Figure 5.11: Theoretical energy spectrum of the Compton-scattered photons based on a beam energy of 7 GeV and a laser wavelength of 532 nm. The maximum energy is 0.78 GeV and the mean value is 0.38 GeV.

(see Fig. 5.12) for the vertical scan during low bunch current conditions gave $\sigma_{meas} = 68 \pm 3_{stat} \pm 14_{sys}$ μm [38]. The systematic error was dominated by the uncertainty of the scanning mirror position in relation to voltage applied.

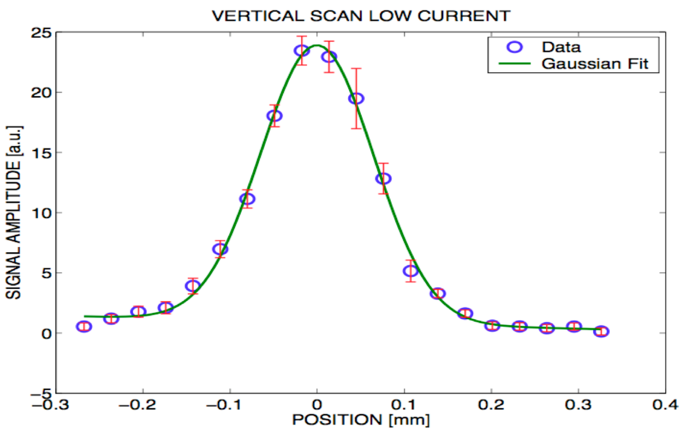

Figure 5.12: Beam size measurement data and fit for the low current scan

5.5 Simulation of the PETRA Laser-wire

The large difference in expected and experimental number of detected photons prompted a realistic simulation of the PETRA Laser-wire project to be performed. The simulation code used for the Laser-wire is a special case set up in an early version of BDSIM[2]. The entire simulation process detailed in this section has been split into three main categories: the geometrical construction of the physical experimental environment; the production, tracking, and subsequent detection of the Compton-scattered photons; the post-simulation analysis and comparison with experimental data.

5.5.1 Constructing the Laser-wire Environment

The simulation was set up as in Fig. 5.13. The layout of the experimental area consists of two beampipes either side of a 28 mrad sectorbend magnet. The calorimeter is located downstream of the sectorbend outside of the PETRA ring.

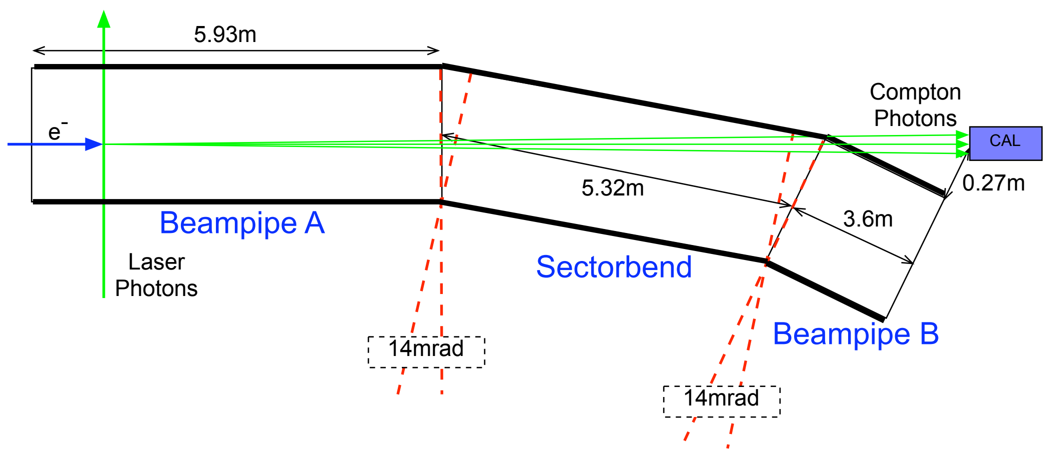

Figure 5.13: Geometry layout of the PETRA Laser-wire experiment. The Compton-scattered photons must traverse the finite thickness of the beampipe wall at a slight angle.

The PETRA beampipe (see Fig. 5.14a) has a flattened octagonal cross-section containing a water cooling channel enclosed by two aluminium walls on the outer perimeter of the beam-line. When the laser/electron IP is vertically centred within the beampipe the Compon-scattered photons must traverse this side wall. The simulated beampipe shown in

[2]BDSIM is described in detail in Chapter 6. The version used for the purposes of simulating the Laser-wire set up was essentially a stand-alone GEANT4 application.

Fig. 5.14b is therefore modelled as a simple cylindrical tube with a water coolant section added within the wall.

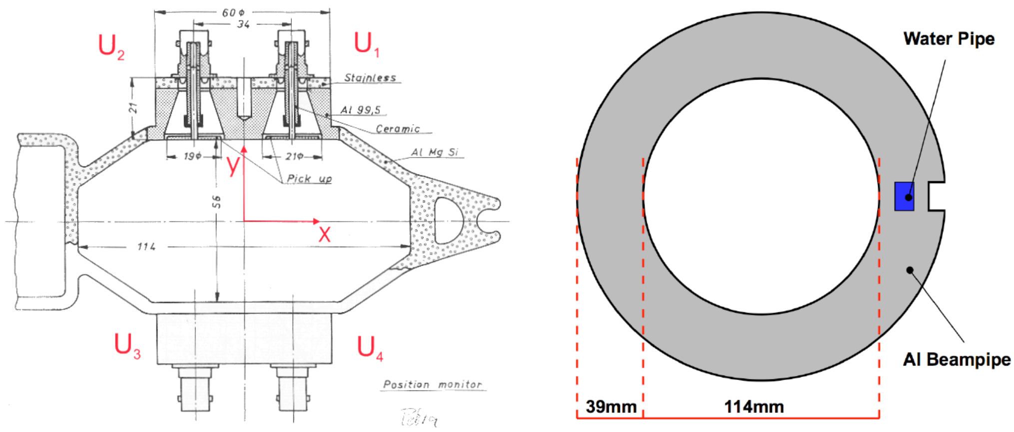

(a) Cross-section of the PETRA beam pipe with the right hand side being the on the outer circumference of the PETRA ring [39]. This example also shows the button pickups of a BPM.

(b) Simulated set up of the beam pipe. Circular approximation is for ease of geometry construction and should not affect simulation performance as only the wall with the water pipe is traversed by the photons.

Figure 5.14: Cross-sections of both the simulated and the actual PETRA beam pipes

Following the Laser-wire design, the calorimeter is modelled as nine appropriately sized $PbWO_4$ crystals arranged in a 3×3 matrix. This forces the simulated photons incident on the detector to undergo the EM showering processes that would take place in the real detector – in this way the simulation can inherently model the expected containment losses. All energy deposited within the calorimeter is logged for analysis. The energy of any photons leaving the rear of the calorimeter are also logged by a counting plane. The PETRA Laser-wire calorimeter is automatically polled for data by the DAQ system. This means that if no photons were detected for a given DAQ trigger then a zero energy reading would be registered. The calorimeter and counting plane in the simulation code are configured in a similar manner to log a non-deposit or non-hit for a given simulation event as 0 GeV.

5.5.2 Simulating the Compton signal

The simulation operates on the assumption that every laser pulse and electron bunch interaction produces a single Compton-scattered photon. The simulation therefore creates a photon with a randomly chosen energy from the Compton energy spectrum appropriate for the PETRA beam energy and the laser wavelength as in Fig. 5.11. The direction of the photon is chosen to be within the expected emission cone. The photon is then tracked along beampipe-A and through the aperture of the sectorbend. Following a direct path parallel to beampipe-A requires the photon to exit the simulated PETRA ring through beampipe-B at a slight angle of 28 mrad. The simulation uses the inbuilt EM processes within GEANT4 to dictate how the photon interacts with the beampipe material. All subsequent particles leaving the beampipe are then tracked to the calorimeter where EM showers are simulated.

5.5.3 Post-simulation Analysis

Repeating the above process a large number of times produces a full energy spectrum of single photons being detected in the calorimeter. This spectrum must then be extrapolated to the theoretical number of photons, N_γ. Poisson statistics can be used to model the fact that N_γ is an expectation value and that the actual number of photons (N_p) for a given laser/electron interaction will be some value based around a mean of N_γ. N_p energy values are randomly sampled from the simulated single photon spectrum and are summed to give a total energy incident on the calorimeter, E_T. This process is repeated for the required number of laser shots – determined by laser rep-rate and the duration of data taking.

Accounting for Experimental Factors

The extrapolated spectrum described above does not take experimental aberrations into account and therefore requires post-simulation corrections. The simulation assumes that the laser pulse has no substructure and that it delivers 100% of the specified power at all times. Ultra-fast streak cameras with a resolution of a few picoseconds were used to probe the power delivery of the laser pulses, Fig. 5.15a. The results indicate that the laser has a very erratic substructure implying that the power delivered to the electron bunch cannot be assumed as constant. The actual power delivered to a 20 ps long electron bunch is estimated by taking a random starting point within the laser pulse and then integrating the observed laser power in the following 20 ps time period, Fig. 5.15b. The distribution of the fractional power delivered using this method is given in Fig. 5.16. This distribution demonstrates that on average the nominal laser power is available during a laser/electron interaction. However, the distribution is asymmetric with a positive skew and indicates that the power can fluctuate from 60% to 350% of nominal.

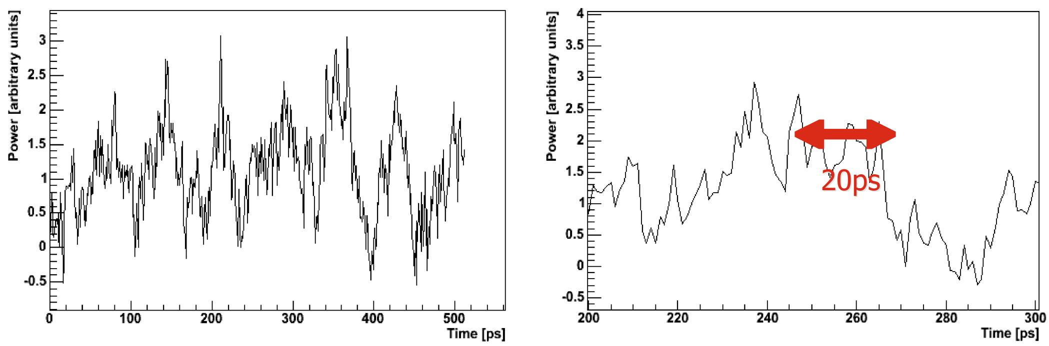

(a) (b)

Figure 5.15: Temporal substructure of the laser captured by a streak camera. (a) shows a typical shot and (b) illustrates a random positioning of the 20 ps electron bunch to produce an effective laser power distribution seen by an electron bunch.

From Equation 5.6 it follows that the number of Compton-scattered photons is directly proportional to the power of the laser. The laser substructure can therefore be accounted for by randomly calculating the fractional laser power (P_f) for a laser/electron interaction and altering each N_p value as $N_p \to P_f N_p$ before sampling the single photon spectrum.

Another factor that must be incorporated into the pre-analysis preparation of the simulated data is the experimental error introduced by the PMT. The simulation assumes that all energies logged by the calorimeter are measured with no loss in accuracy. Realistically

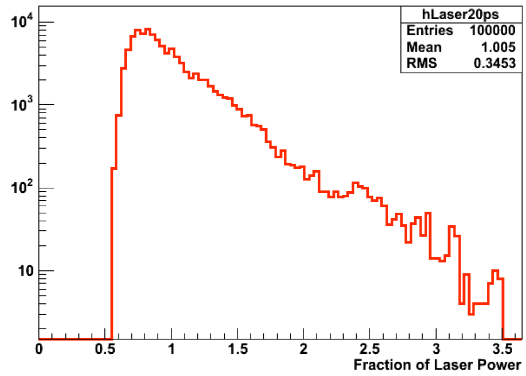

Figure 5.16: Fraction of laser power delivered to 20 ps long electron bunches.

the PMT has a resolution associated with it that depends on operating conditions such as temperature, voltage supply stability, and local radiation levels. The estimated resolution of 11% [31] was therefore factored into each energy reading from the simulated calorimeter.

5.5.4 First Simulation Results

The simulations produce a single Compton-scattered photon spectrum as shown in Fig. 5.17a. From counting the number of zero energy events registered by the calorimeter it is evident that more than 99% of the photons are lost before reaching this point.

The photons are fully tracked from their production point at the laser/electron IP to the detector. The main obstacle between these two locations is the beampipe wall and the slight angle of entry of the photons into this material equates to more than 1 m of aluminium and $\sim$0.17 m of water that must be traversed. The lack of signal indicated by the simulations implies that the majority of the photons are lost in this beampipe material and forecasting simulations show that this situation can be greatly improved in the absence of such material, Fig. 5.17b.

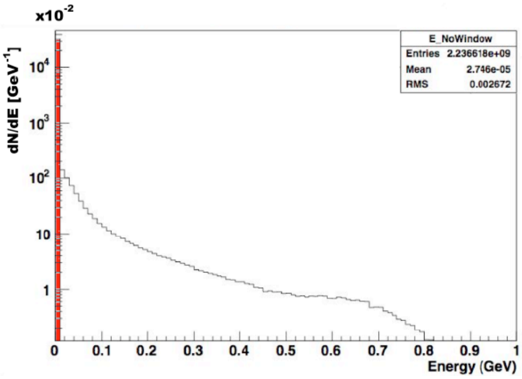

(a) Expected spectrum with beampipe material. More than 99% of the events are registered in the shaded region with zero energy

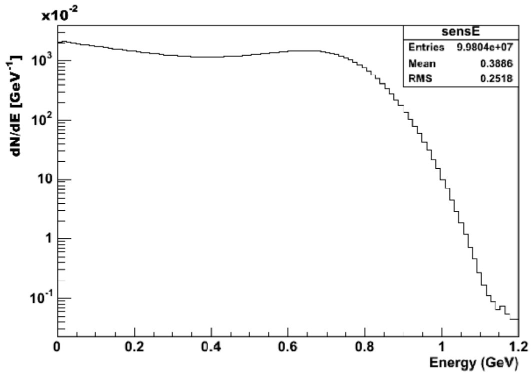

(b) Expected spectrum if no beampipe material. The theoretical spectrum can be seen in addition to a tail resulting from PMT resolution effects.

Figure 5.17: Energy spectra for a single Compton-scattered photon, including PMT resolution.

5.5.5 Exit Window Installation

The initial simulation results suggested that the PETRA beampipe required extensive alterations to improve the detected signal. Engineers at DESY were therefore contacted to start the design process for a beampipe that would reduce the material “seen” by the Compton-scattered photons, see Fig. 5.18a. A signal “exit window” was subsequently fabricated to enable the photons to arrive at the beampipe wall with an incident angle of 90°, requiring the traversal of a maximum of 6 mm of aluminium. Fig. 5.18b shows the finished installation of the signal exit window in the PETRA beam-line.

5.5.6 Experimental Data with Exit Window

The installation of the exit window required several steps to be taken to protect the detector set up from the now unhindered SR photons. Shielding in the form of a 25 mm lead block was placed directly in front of the detector assembly to reduce the radiation load on the calorimeter to within tolerable limits. Even with this shielding the Compton

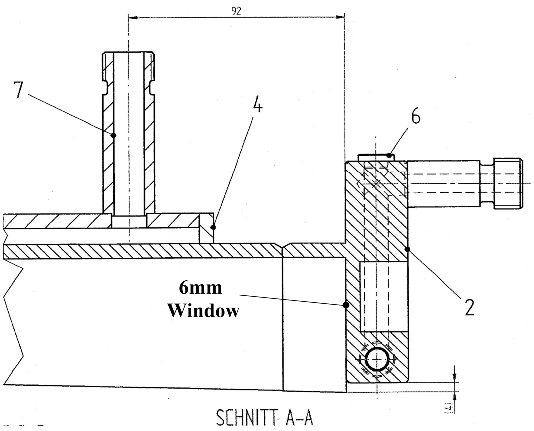

(a) Technical design drawing of the exit window

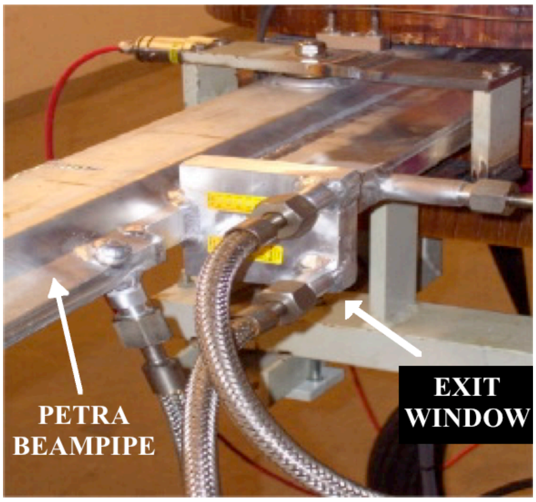

(b) Photo of the new window installed

Figure 5.18: The exit window installed in the PETRA storage ring for the Laser-wire project.

signal was noticeably enhanced and required the voltage gain on the PMT to be lowered in order to avoid signal saturation. Owing to time constraints on PETRA machine time and intermittent run capability with a degradation in laser stability[3], a long data run with the laser position at maximum overlap with the electron bunch, or "on-peak", was not possible. Priority was instead allocated to improving the Laser-wire's scanning times and profile measurement techniques. Data from $\pm 20\%$ of the Gaussian fitted profile peaks was therefore extracted from seven successful low current profile measurements in an attempt to reproduce on-peak data for simulation comparisons, Fig. 5.19.

The simulation was modified to account for the 6 mm exit window and also the alterations made to the detector configuration discussed above. Based on the PETRA machine parameters used during the vertical profiling scans the expected number of photons at the on-peak position is 170. The single Compton-scattered energy spectrum from the simulation was accordingly extrapolated and compared to the on-peak data, Fig. 5.20.

[3]The laser was suffering from cooling issues and was subsequently upgraded.

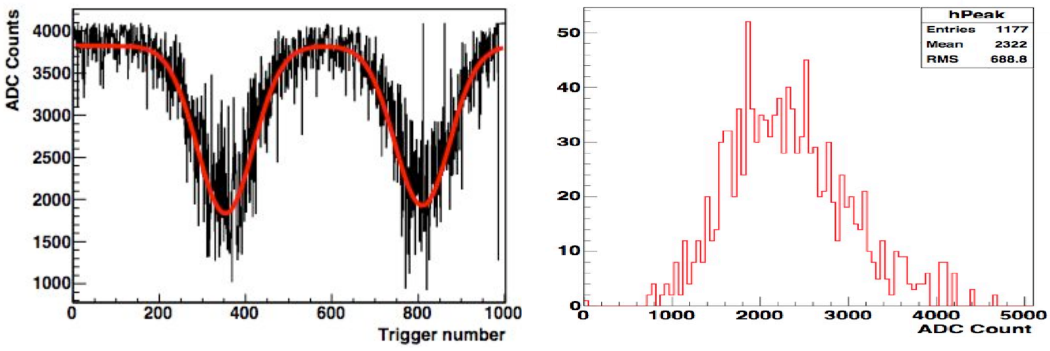

(a) (b)

Figure 5.19: Laser-wire data: a) for a single scan of the electron beam. To generate maximum laser-electron overlap, data from 25% of the Gaussian-fitted peak of each scan was collected resulting in (b).

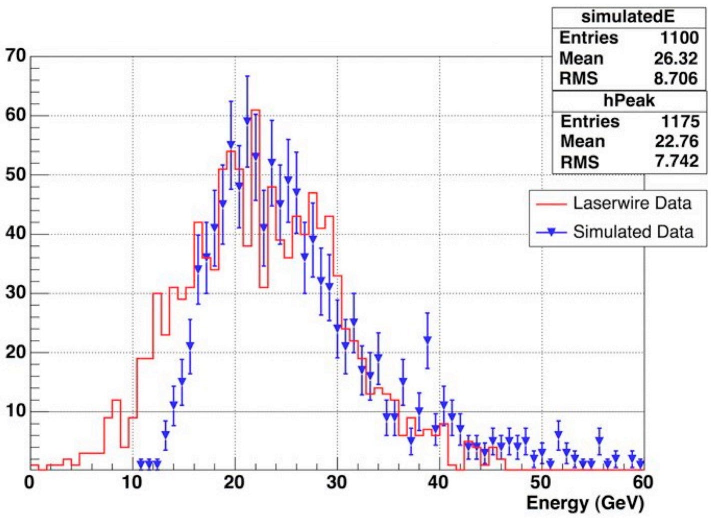

Figure 5.20: Calorimeter energy spectra for experimental data and simulated events based on 170 Compton-scattered photons [40].

The experimental data show an energy resolution of 34% which is dominated by the longitudinal fluctuations in the laser power. At this stage in the Laser-wire development, these fluctuations were incorporated into the simulation using relatively old streak camera data as described in section 5.5.3 and so did not account for the degrading quality of the laser since then. The calorimeter had also been in the PETRA radiation environment for three years which may have contributed to a poorer energy resolution than accounted for in the post-simulation analysis. This could explain why the simulation fails to completely model the experimental data in the lower energy region.

5.6 Laser Performance Projections

The power stability issues of the laser have been discussed in section 5.5.3. The simulations have shown that under these conditions the photons are detected with an energy resolution of more than 30%. Fig. 5.21 shows the energy resolution on a given number of Compton-scattered photons with and without the laser power fluctuations. These plots confirm that the major contribution to the low energy resolution is from the laser stability. These results are indicative of the quality of signal that should be expected with the purchase of a laser that can deliver highly stable pulses. In this case the detector resolution of $\sim$11% becomes the dominant factor.

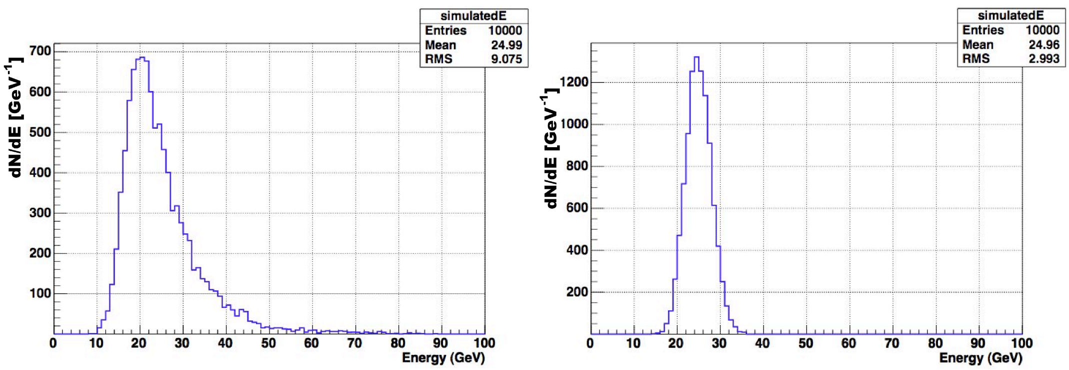

(a) (b)

Figure 5.21: Simulated energy spectra (a) including laser fluctuations and (b) assuming the laser delivers nominal power at all times.

5.7 Summary

The concept of a non-invasive beam-profiling technique using focussed laser light has been discussed as an alternative to standard wire-scanners. The installation of the Laser-wire project at the PETRA storage ring initially operated below expectations in terms of the observed Compton signal. Full simulations of the Laser-wire installed in the PETRA storage ring were performed using an early version of BDSIM, forming the first experimental benchmarking of the simulation code. The results demonstrated that more than 99% of the signal was lost whilst traversing the material of the beampipe. Subsequent recommendations to install a purpose built window in the PETRA beam-line allowed a significantly stronger signal to reach the detector.

The degradation of the laser with respect to its temporal profile was modelled within the simulations and was shown to contribute to the majority of the energy resolution error. The Laser-wire project has since installed an upgraded laser with a higher degree of stability. Laser optics have also been developed to perform horizontal beam profile scans.

Chapter 6

Beam Delivery SIMulation Toolkit (BDSIM)

Throughout the design process of the ILC a variety of software simulation tools have been employed to evaluate expected operating conditions, achievable performance levels, and to provide useful feedback on key development issues. The level of sophistication required from these simulation codes has increased hand in hand with the complexity of the ILC design. For this reason many software packages have evolved to become invaluable tools in highly specialised areas of the ILC.

The idea of BDSIM was conceived as a necessary tool to extend existing styles of simulating beam transportation [41]. The combination of accelerator-style fast tracking and the handling of particle interaction processes enabled essential simulations to be performed under a single code framework. This chapter introduces the infrastructure of the BDSIM software package and describes the various validation and benchmarking studies carried out. The extensive development for beam-line and detector integrated simulations is also discussed in detail along with modifications whose implementation has been dictated by various studies carried out in this thesis. A full overview and usage guide for BDSIM can be found in [42].

6.1 Code Framework

Written in the C++ programming language, BDSIM is a GEANT4.8 [43] extension toolkit that provides accelerator-style particle tracking. GEANT4 provides the overall run management, geometry construction, visualisation classes, and particle physics framework. The basic architecture of BDSIM is illustrated by Fig. 6.1. BDSIM introduces a comprehensive user input system, tracking techniques, geometry descriptions, and specialist/modified physics processes. The ROOT analysis framework [44] is incorporated into BDSIM to handle the simulation data. The following sections describe how BDSIM implements these features.

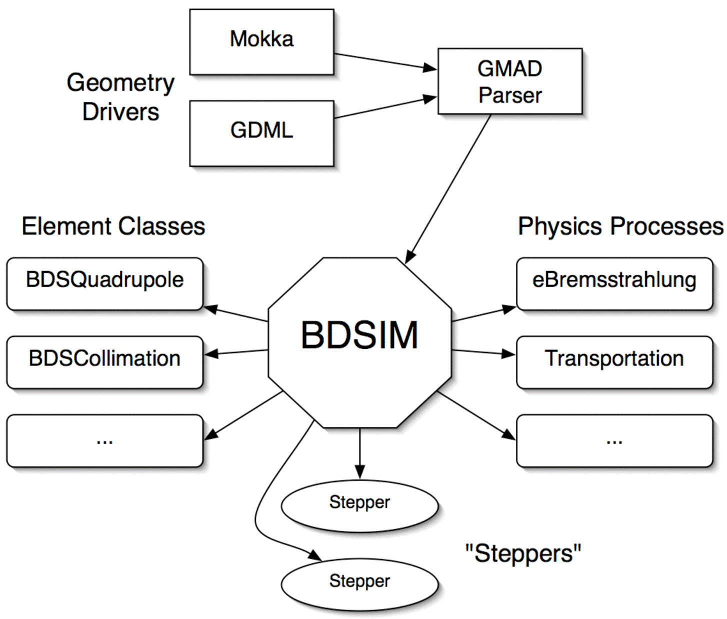

Figure 6.1: Chart of BDSIM architecture.

6.1.1 User Interface and Input

BDSIM has undergone extensive development to facilitate the simulation set up process and has evolved to include a user interface and input system that potentially removes the need for any programming knowledge. An accelerator description language referred to as

GMAD [45] has been designed to add GEANT-like extensions to the MAD [46] language commonly used by accelerator physicists. The user specifies the beam-line components, beam properties, and physics processes for a given simulation using a GMAD file as an input to BDSIM. A basic example for tracking a Gaussian distributed 500 GeV electron through a user-defined optics lattice could take the following form:

```
option, beampipeRadius=10*cm,
        beampipeThickness=0.1*cm,
        boxSize=0.5*m;
d: drift, l=0.5*m;
qd: quadrupole, l=1.0*m, k1=-0.1;
qf: quadrupole, l=1.0*m, k1=0.1;
a_lattice: line=(qf,d,qd,d);
use, period=a_lattice;
beam, particle="e-", energy=500*GeV, distrType="gauss";
```

The above GMAD script would produce the visual output from BDSIM given in Fig. 6.2.

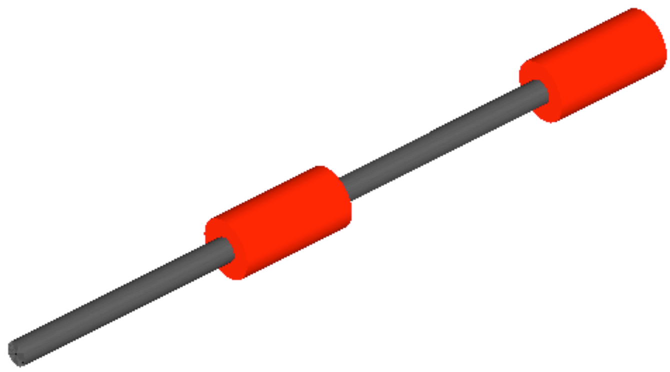

Figure 6.2: Visualisation produced from running the example script in BDSIM. The red cylinders represent the quadrupoles whilst the beampipe is denoted by the grey tubes.

The GMAD input file has an extensive and constantly evolving array of options and parameters that can be added to further customise both the BDSIM and GEANT4 simulation options. The initial particle conditions can be randomly generated according to an inbuilt distribution as shown in the above example script. Alternatively, any space-delimited input files can be used in the case that specific initial particle parameters or bunch output from third party simulation programs is required. For example, a file containing energy, x, y, x′, and y′ could be specified by setting:

```
distribType="E[GeV]:x[nm]:y[nm]:xp[mrad]:yp[mrad]"
```

The default co-ordinate system used within the BDSIM framework follows the accelerator standard of the nominal beam trajectory forming the z-axis, with x and y axes being the horizontal and vertical axes respectively.

Advanced methods for defining complex geometry descriptions have been developed and are described in detail in section 6.5. Geometry construction in GEANT4 is handled by this interface to allow a wide range of volume types with placement hierarchy at runtime. The application of either uniform fields, standard component fields (up to octupole), and limited field maps are possible.

6.1.2 Beam-line Component Construction

GEANT4 applications ordinarily track particles through magnetic fields by solving equations of motion over many incremental steps using Runga-Kutta (or otherwise) techniques. BDSIM adds to these inbuilt tracking algorithms in a complimentary way, defining a set of tracking mechanisms called "steppers" based on standard high energy beam transport components – such as quadrupoles, and sectorbends. Each stepper type has a pre-defined algorithm relevant to its accelerator component. The algorithms allow the stepper to transform the particle's momentum and position without using Runga-Kutta techniques to solve the usual equation of motion. This greatly improves the tracking time and also allows for the inclusion of complex (e.g. multipole) fields. An example of the transformation rules used by the steppers is given in the case of a (focusing) quadrupole stepper, Equation 6.1. A comprehensive review of the BDSIM steppers can be found in [42].

$$\begin{pmatrix} x \\ x' \\ y \\ y' \end{pmatrix} = M \times \begin{pmatrix} x_0 \\ x'_0 \\ y_0 \\ y'_0 \end{pmatrix} \tag{6.1}$$

where M for a quadrupole providing horizontal focusing of positively charged particles is given by:

$$M = \begin{pmatrix} \cos(\mathrm{h}\sqrt{\mathrm{k}}) & \frac{1}{\sqrt{k}}\sin(\mathrm{h}\sqrt{\mathrm{k}}) & 0 & 0 \\ -\sqrt{k}\sin(\mathrm{h}\sqrt{\mathrm{k}}) & \cos(\mathrm{h}\sqrt{\mathrm{k}}) & 0 & 0 \\ 0 & 0 & \cosh(\mathrm{h}\sqrt{\mathrm{k}}) & \frac{1}{\sqrt{k}}\sinh(\mathrm{h}\sqrt{\mathrm{k}}) \\ 0 & 0 & -\sqrt{k}\sinh(\mathrm{h}\sqrt{\mathrm{k}}) & \cosh(\mathrm{h}\sqrt{\mathrm{k}}) \end{pmatrix} \tag{6.2}$$

where h is the step length and k is the strength of the quadrupole in terms of the field gradient dB_z/dx normalised to magnetic rigidity $B\rho$ as:

$$k = \frac{1}{B\rho}\frac{dB_z}{dx} \tag{6.3}$$

Each beam-line component is implemented via a set of dedicated element classes that have the following common functionality:

- Constructing GEANT4-compliant geometry from standard component templates with minimal user input for definitions. Rotation and positioning of elements is automated with respect to preceding elements, with alignment centered upon the beampipe.

- Defining a region of 3-dimensional space in which a tracked particle is expected to be subjected to the function specific to the element-type.
- Creating and assigning an instance of an appropriate stepper to dictate how the particle should be propagated in the aforementioned volume.

An overall construction class arranges the components to form a beam-line as specified by the GMAD input file. By default the beam-line is placed arbitrarily in space, however it can optionally be enclosed within a concrete tunnel if containment related studies (such as muon backgrounds) are necessary.

6.1.3 Physics Processes

Having specified the geometry and accelerator tracking aspects of the simulation, the processes within GEANT4 are activated from within the GMAD file. The processes are grouped into lists that, depending on the application of BDSIM, can be prescribed for the simulation. BDSIM also includes modified versions of some GEANT4 standard processes to enhance their use in an accountable way. Processes that would otherwise have small cross-sections can be biased to occur more frequently so as to focus the output of the simulation. For instance, if muon production was left as the GEANT4 standard then muon background studies would be time consuming. Altering the physics processes to increase muon production can dramatically speed up these investigations and requires simple weighting of the results to cancel the introduced production bias. The simulation output can then be re-weighted accordingly before being analysed. Physics processes can also be modified to allow for the controlling of production cuts within certain geometry regions.

6.1.4 Data Handling

The data produced by a simulation can be either be saved to ASCII files or handled by BDSIM's integrated ROOT functionality. Regardless of how the data is presented to the user it can be created via two methods. The first method is an automated mechanism that records the beam energy loss as a function of beam-line length by logging the relevant information of each particle that deposits energy in the beampipe material. This is an inbuilt feature partly as it forms a useful debugging tool to check that the simulation has been properly set up, but mainly because energy loss plays a key role in the evaluation of lattice designs.

The second method of logging data within BDSIM is by the placement of sampling planes at user-specified beam-line locations. These planes are effectively zero length (1×10^{-11} m) and record a comprehensive range of information of a passing particle without altering the particle or optics lattice. As samplers fall into the category of beam-line elements they are placed into the lattice centred on the beampipe, which is useful when viewing data from many consecutive samplers.

In the case that the user chooses ROOT data handling, the simulation data is stored in structured ROOT files, Fig. 6.3. Output can also be spread over multiple ROOT files in the case of a large number of simulation events. As well as being analysable using the main ROOT package, a purpose-built ROOT display application has been designed for use with BDSIM[1]. This application reads in a ROOT file and the initial GMAD file to combine elements of both the input and output data on a single interactive ROOT canvas. Data from samplers can be analysed and displayed as graphs or histograms below a linked optics lattice layout as illustrated by Fig. 6.4. Zooming is linked for both the plot and the lattice layout and clicking on an element in the lattice display will open a second window containing the component parameters.

[1] ROOT display for BDSIM use designed by O. Dadoun, LAL.

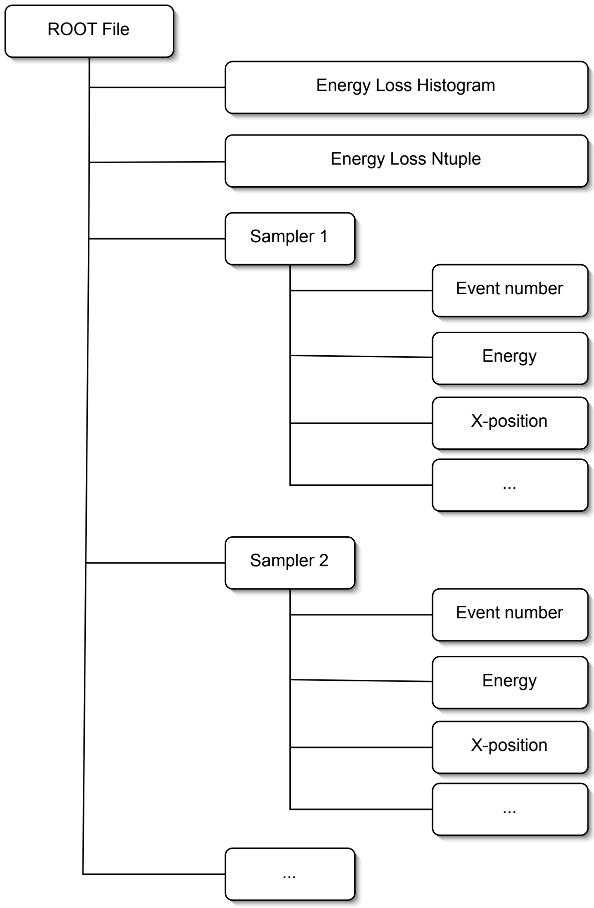

Figure 6.3: ROOT file structure.

6.2 Code Management

As a rapidly evolving simulation code BDSIM is maintained by several developers and contributors at a number of institutes. The code is housed under a concurrent versioning system (CVS) repository at Royal Holloway University that allows for updates and modifications to be made whilst also keeping a development history. The code within the CVS repository is used strictly as a developmental version of BDSIM, whilst production stable packages with version release stamps are available from the code's web area [47].

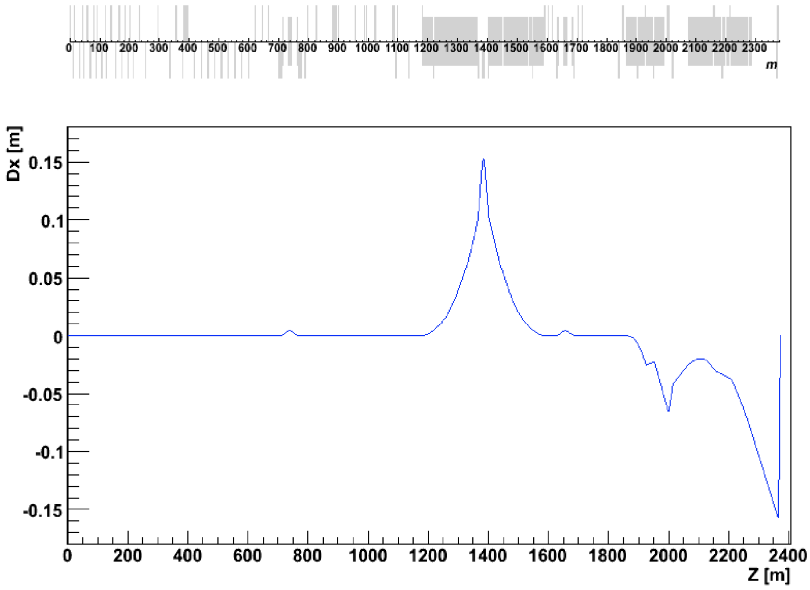

Figure 6.4: Example of the interactive ROOT display application that shows GMAD lattice data above the simulation data plots. In this example the horizontal dispersion is mapped along a 2.4 km optics lattice.

6.3 Distributed Computation

The level of detail achievable by simulation codes such as BDSIM are often limited by the available processing power of the host machine. This is an issue shared throughout all areas of computational physics and so an enormous amount of effort has been devoted to developing platforms to meet the demands of processing intensive applications. The LHC project has developed a distributed analysis framework referred to as the worldwide LHC Computing Grid (LCG) [48]. The driving philosophy behind the LCG is to have a number of sites around the world that each have a large collection of linked computers, known as computer farms. Each farm is managed by an automated queuing system that distributes incoming jobs to the individual processing nodes. Submitting a large simulation as a single job to the LCG provides no real advantage over running on a powerful and locally available machine. The key advantage of using GRID platforms is derived from the simultaneous job processing capability. Splitting a large job into many small batches to be submitted to the LCG can provide a dramatic decrease in the overall processing time for a given simulation.

6.3.1 Royal Holloway Grid Farm

A Grid farm consisting of 75 worker nodes was installed at Royal Holloway University's Particle Physics group in 2004. Each node provides dual processing power enabling up to 150 jobs to be run simultaneously. A comprehensive set of scripts was developed to submit BDSIM jobs locally to this computer farm by distributing events across a specified number of smaller jobs. The scripts automatically submitted each batch to the job whilst managing the input bunches, GMAD files, ROOT output files, and runtime environment variables. The local grid farm has a development version of BDSIM installed in the users' area and thereby has a distinct advantage in that code modifications can be performed relatively quickly.

6.3.2 Global Grid

The scripts developed for the local job submission were enhanced and modified to include the necessary Grid communication scheme – forming the BDSIM Accelsoft package[2] [49]. In both local and global grid usage a version of BDSIM must be pre-installed before submitting the jobs. In the case of the global system, a variant of Accelsoft is used to "parachute" a compressed version of BDSIM and its dependancies onto a grid farm. The sole function of the submitted "job" is to unpack and install BDSIM. This process is performed whenever a new version of BDSIM is released.

6.4 Simulation Comparison Studies

Benchmarking and comparison studies of simulation codes such as BDSIM are essential for code development. As well as ensuring credible and reliable results, studies of this

[2] BDSIM Accelsoft package developed by I. Agapov, RHUL.

type also help to draw attention to areas of the code that can be improved – often giving a useful insight into the various methods available to execute the modifications.

6.4.1 DIMAD

DIMAD [50] is an optics lattice code that tracks charged particle beams using the second order matrix formalism of TRANSPORT [51]. Simulations are configured using MAD optics decks which can be easily converted to the GMAD format used by BDSIM. Tracking comparisons of these two codes within the scope of the ILC disrupted beam extraction lines have been performed and documented in [52].

The approach to lattice construction is fundamentally different for each code. BDSIM creates a lattice in a realistic 3-dimensional “virtual world” and so components are built using fully modelled materials. An unavoidable consequence of this is that each component has a physical extent that must be taken into account. In contrast to this DIMAD creates a mathematical lattice model containing regions (beam-line elements) in which particle behaviour is simulated. If the particles leave a region in a non-modelled way – such as through a beampipe wall – they are essentially “lost” to the simulation until they reach the z-location of a detection plane such as a collimator wall. This difference is illustrated schematically by Fig. 6.5 where the presence of physical dimensions and materials in BDSIM lead to a disparate result in terms of particle loss location. It can also be seen that BDSIM records losses along the entire inner aperture of an element, whereas in the configuration in Fig. 6.5b results in DIMAD collecting all loss information at a single location.

Another key difference between the two codes derives from the GEANT4 shower capability built into BDSIM. A particle registering a hit on a given element in DIMAD has its total momentum recorded as a loss and tracking of the particle is subsequently ceased. The same particle in BDSIM would interact with the material of the element in a way dictated by GEANT4. This could, for example, lead to scattering and EM showering and the creation of secondary particles. Only the energy deposited into the material is registered

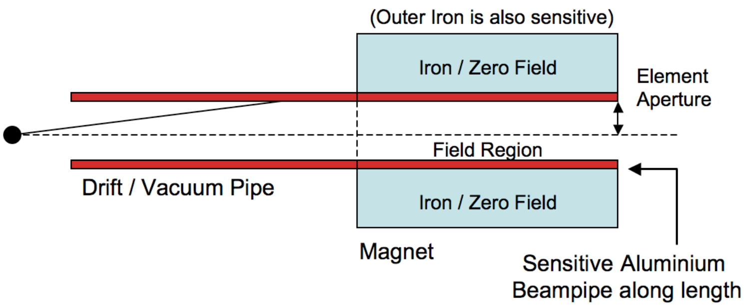

(a) BDSIM lattice treatment

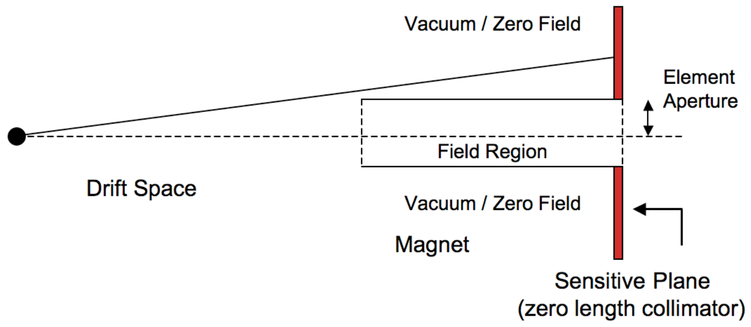

(b) DIMAD lattice treatment

Figure 6.5: Schematic to highlight a key difference in particle loss treatment between DIMAD and BDSIM.

by BDSIM as a ”hit” and an important point to note is that the act of hitting the element can have knock-on side effects from secondary particles at other beam-line locations.

6.4.2 STRUCT

STRUCT is a Fortran-based Monte-Carlo program for simulating particle tracking and interactions [53]. Lattices are entered into the program by specifying the parameters for the optics components on a line by line basis. Preliminary tracking comparisons with BDSIM were performed using the 2 mrad extraction line[3]. A standard particle distribution

[3]STRUCT simulations were performed by A. Drozhdin and Xi Yang at Fermilab National Laboratory

of nominal energy and a transverse phase space as shown in Fig. 6.7a was used as the tracking input to both codes. The tracking results showed excellent agreement up to the entrance of the pocket region of QF1. Fig. 6.6 illustrates the optics layout used in the BDSIM-STRUCT comparison.

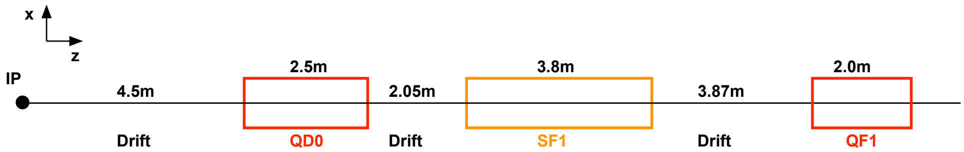

Figure 6.6: 2 mrad FF optics layout. The post-collision bunches are simulated with a horizontal opening angle of 1 mrad at the IP.

Fig. 6.7b illustrates the tracking differences seen after traversing this region, which was modelled in both codes as a multipole expansion. STRUCT took this expansion to the 9th order, whereas BDSIM went to the 4th. These results indicate that BDSIM required a more advanced method of multipole expansion and subsequent development of an n^{th} order multipole stepper was started.

6.5 Complex Geometry Regions

An important issue to be considered when designing the BDS is the level of backgrounds produced in the detector region as a result of the proposed layouts and designs. Passing data from beam transport programs to detector simulations is one method of performing such checks on background conditions. However, this approach is not without its drawbacks:

- Using output data from one software code as an input to a third party program can lead to data format issues and misinterpretations.
- Passing the data between two simulation programs increases the time required for feedback on designs. Delays in feedback affect the turnaround time for iterating the

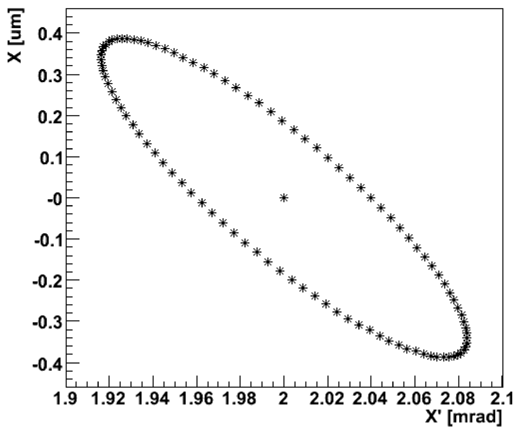

(a) Initial X/X' phase space of particles used tracked by BDSIM and STRUCT along the 2 mrad extraction line.

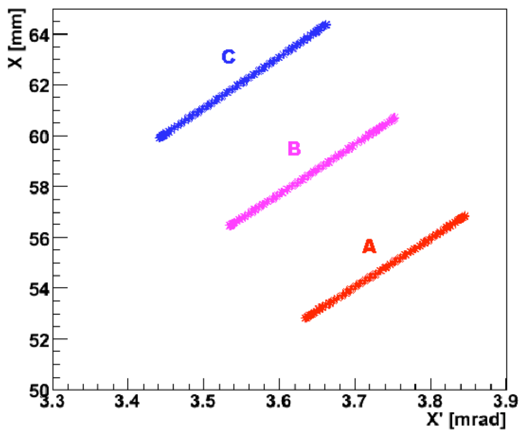

(b) Phase space before and after traversing the mulitpole expansion for the pocket field. Distributions labelled as: A – BDSIM and STRUCT before multipole; B – STRUCT after mulitople; C – BDSIM after multipole

Figure 6.7: Tracking results from BDSIM and STRUCT.

design. A simulation that is able to carry out both beam transport and investigate the detector region backgrounds will facilitate the fine tuning process of a given design.

- Studies that require numerous crossovers between the beam-line and detector regions – for instance performance checks on particle transport from the BDS, through the IR, and into the extraction lines – can become cumbersome with multiple exchanges between simulation programs.

It is therefore desirable to simulate both beam transport and detector regions from within a single code so that studies can be progressed from start to finish using a single simulation package. This goal has provided the motivation for the development of an interface to a detector geometry manager. In view of the fact that BDSIM operates within the GEANT4 geometry construction framework it was desirable to choose a GEANT4 compatible detector geometry description.

6.5.1 Mokka

The Mokka [54] detector simulation package is a GEANT4-based program that was designed for use with linear collider studies. It uses a MySQL driven database system for storing geometry descriptions that are called upon at runtime. The geometry models are stored within the database in tables that do not require standardisation as each model (or collection of models) has a purpose written "driver" that understands the format. The role of the driver is to use this knowledge of the table structure to pass the geometry data correctly to its GEANT4 volume constructor.

A central MySQL server, accessible via an internet connection, hosts the main database containing frozen reference geometry. Users typically download this geometry data into a local MySQL server to allow for model development. Once a new model or improvements to an existing one have been approved, the geometry data and the associated driver can be incorporated to the central repository.

6.5.2 Designing a Mokka Interface

The level of geometry detail required by detector simulations such as Mokka is far greater than that proposed for use with BDSIM. The background simulations required of BDSIM typically need the IR geometry in the sense of masking, scattering effects, and aperture constraints. A number of components can therefore be modelled as solid volumes of an appropriate size and material type – as opposed to the high sub-component structure necessary for detector simulations.

When considering the relatively limited number of geometry models to be stored, the overhead involved with maintaining and accessing a MySQL database is not justifiable. However, MySQL provides an ASCII based database output referred to as "dump" files. These files contain the data encased in MySQL command keywords so that they can be directly loaded back into a database. The decision was made to add an interface to BDSIM to enable it to parse geometry data files that have been dumped from the Mokka database.

A geometry handling class was created alongside the standard beam-line component classes. This class is passed the necessary parameters (such as file locations) by the GMAD script and the interfacing process (see Fig. 6.8) is started. All files are initially parsed by a purpose written wrapper class that uses the MySQL keywords and file structure to appropriately place the data into the simulation memory. A detector component may be too complex to be described by a single shape and so a dump file may contain several smaller shapes that must be combined – either by boolean operations or positioning hierarchy. To account for this, all the geometry data is stored in such a way that relational links are preserved. This means that components cannot be constructed in GEANT4 until all dump files have been read into memory. At this stage a geometry handler runs through all the data and follows all links to construct the GEANT4 volumes. The collection of components is then placed into the beam-line at a location and rotation specified in the GMAD file.

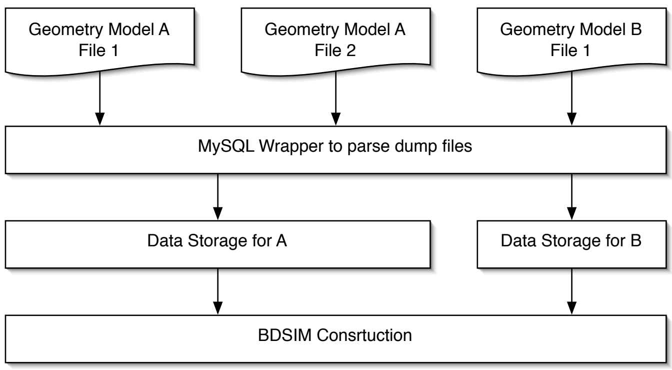

Figure 6.8: BDSIM geometry processing structure.

6.5.3 Geometry

The number of volume types and methods of handling geometry input within the Mokka-interface framework are constantly evolving according to simulation requirements. Potentially the interface should be able to use the full functionality of the GEANT4 geometry drivers. However, only the following geometry types are currently available: boxes, cylinders, tubes, cones, polycones, toroids, and Boolean shapes formed by adding or subtracting two volumes. In addition to these shapes the interface can handle hierarchal positioning of volumes in the usual GEANT4 mother/daughter fashion. Any volume can also be made to be “sensitive” so that it adds to the standard energy deposit versus beam-line position data. Thin sampler planes can be created anywhere within the Mokka interface region to record data in a separate but similar way to the BDSIM standard samplers. For ease of visualisation, the interface is capable of applying the usual GEANT4 range of attributes to prescribe how each volume should be drawn. A complete overview of how geometry descriptions should be constructed for use with BDSIM can be found in [42].

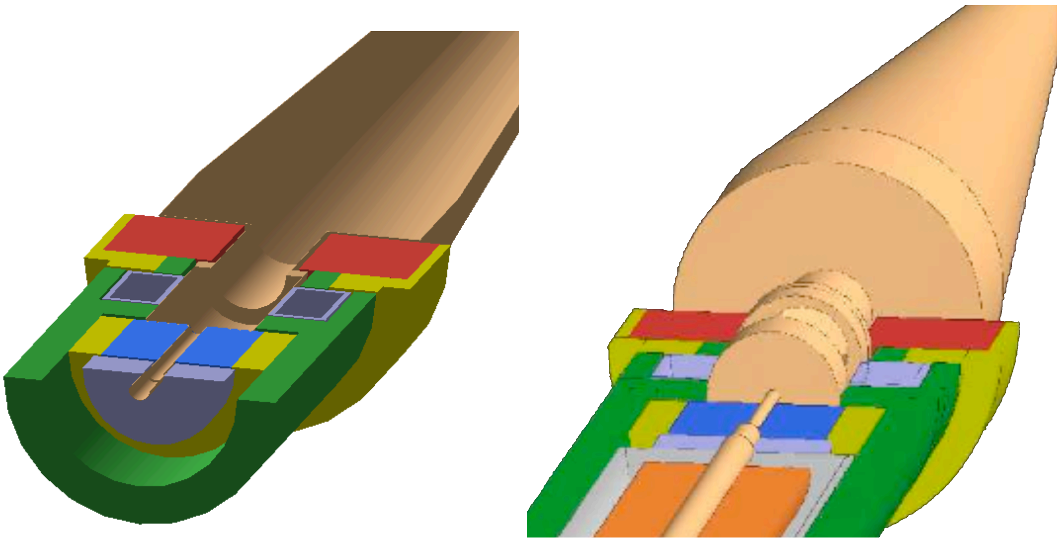

(a) BDSIM (b) Mokka [55]

Figure 6.9: Geometry building comparison. Both codes have built detailed 2 mrad IR’s using the same input files. This detector geometry is also modelled in BDSIM with the inclusion of the hadron and EM calorimeters in Fig 7.5.

6.5.4 Field Regions

There are two options available for attaching a field to a volume built using the interface. A uniform field can be set by specifying the three Cartesian field components alongside the volume’s geometry parameters and will be used to create a G4Uniform field. The second option is to apply pre-set fields for tracking in a quadrupole, sextupole, or octupole. For example, applying a quadrupole field to a vacuum tube would set the field components as:

$$B_x = y\frac{dB_z}{dx} \tag{6.4}$$

$$B_y = x\frac{dB_z}{dy} \tag{6.5}$$

$$B_z = 0 \tag{6.6}$$

where the co-ordinate system is a local definition that assumes that the length of the tube is on the z-axis and that x and y refer to the transverse position of the particle with respect to the centre of the tube. This ability to construct lattice elements in this way is useful as the end of the BDS is technically within the IR, and so often it is convenient to build the last these into the Mokka region. However, doing so negates the advantages gained from BDSIM's accelerator-style tracking, and so the Mokka variants should be used judiciously.

In order to properly study background issues in the IR the ability to set up a solenoid field from a range of typical map files has been implemented. The detector concept groups typically provide field maps as z positions with corresponding B_z strengths. The interface reads in these values and calculates the radial strength B_r on the assumption that the solenoid field has azimuthal symmetry. To speed up tracking time within the solenoid region a complete 3-dimensional look-up table is created in the program's memory before any events are simulated. The accuracy of tracking is increased by calculating the field at any given point as an interpolation of the eight neighbouring points. By using this method it is possible to smooth out any discontinuities that may arise in the coarse description provided by the field map files. The solenoid field is set to saturate through all components in the Mokka region and to add to any existing uniform or magnet fields.

The field map implementation in BDSIM was cross-checked against a set of DIMAD simulations that studied the effect on vertical beam orbit from coupling of the solenoid and final focus magnets [56]. Fig. 6.10 shows the BDSIM results of tracking a 250 GeV and on-axis electron from the entrance of the final doublet to the IP when using the field map given in Fig. 7.6. A comparison between the BDSIM results and those from [56] are detailed in Table. 6.1. The small differences in the IP tracking values are due to the differences in the field interpolation methods employed by each code.

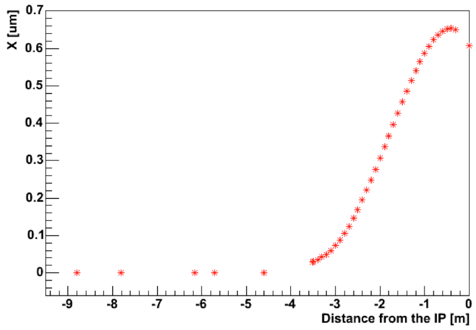

(a) Horizontal beam orbit

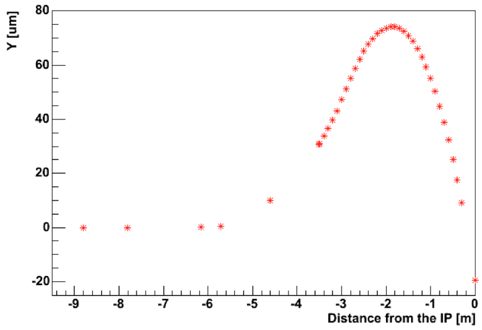

(b) Vertical beam orbit

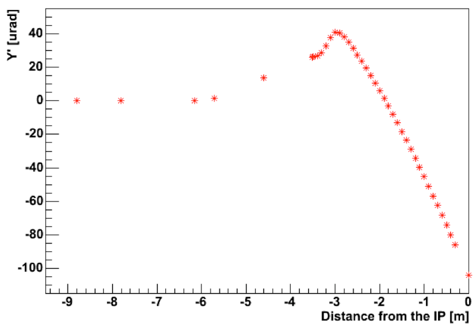

(c) Vertical angle

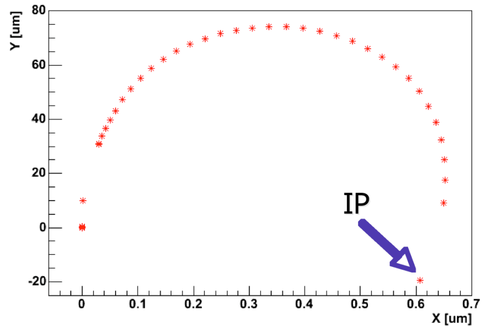

(d) Horizontal and vertical beam orbit

Figure 6.10: Tracking a 250 GeV electron with on-axis initial parameters through one half of the IR using BDSIM.

6.5.5 Other Geometry Interfaces

Initial development of alternative geometry interfaces was carried out after the first implementation of the Mokka geometry handler. In particular, the silicon detector (SiD) concept group [57] use an extension of the Geometry Description Markup Language (GDML)[58],

Table 6.1: Beam parameters at the IP after tracking through the solenoid and magnet coupled fields for BDSIM and DIMAD tracking.

	X [μm]	Y [μm]	Y' [μrad]
BDSIM	0.61	-19.45	-104.2
DIMAD	0.65	-18.50	-104.0

which is based on Extensible Markup Language (XML)[59]. This geometry package, known as the Linear Collider Detector Description (LCDD), is used within the detector simulation framework of SLIC (Simulator for the Linear Collider) [60]. The LCDD format extends the basic geometry format to include sensitivity parameters required for full GEANT4 simulations. SLIC is essentially a software hub that brings together a range of simulation tools, such as GEANT4 and LCDD to allow detailed simulations of the detector. The advantages of using the XML based format is that it is extremely well defined and highly portable.

The LCDD package is written in XML and so its use within BDSIM required the integration of a third party XML parser, Xerces C++. Using this parser in conjunction with several GEANT4 geometry handling classes provided by the GDML package it was possible to implement a simple geometry-only based LCDD parser within the BDSIM framework. The full SiD detector geometry was constructed using BDSIM resulting in the output shown in Fig. 6.11.

After the initial development phase it was decided that the LCDD extension to BDSIM would be implemented in a public release version at a later date if deemed necessary. There are several reasons as as to why this decision was made:

- The inclusion of another third party software – in the form of the XML parser – made the initial installation of BDSIM cumbersome. The Mokka-style interface requires no extra software and so forms an attractive baseline interface.
- The LCDD format available at the time of development was extremely comprehen-

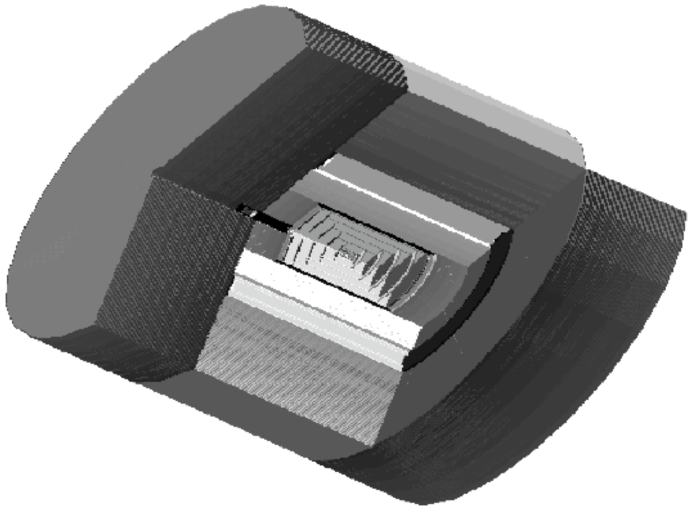

Figure 6.11: Cut-away view of the SiD detector constructed in BDSIM using the LCDD format.

sive with over 26,000 lines of XML code used to describe the SiD detector. This results in a far greater detail than required for BDSIM. The geometry descriptions stored in the Mokka MySQL database were more readily available in reduced versions suitable for BDSIM.

- The ability to develop the code locally and the simple framework of the Mokka-style interface allows for customisable implementation of new features with a faster iteration time.

- The LCDD XML files are designed to be read into SLIC as an all-inclusive GEANT4 geometry description – encasing the detector volumes within the top-level “World” volume. The GDML geometry handlers strictly follow this set up process. However, BDSIM requires the geometry to be input as a subset of its existing geometry model and so extensive re-development of the LCDD file handling would be necessary.

6.6 Automatic Magnet Re-scaling

The strength of each element in the BDS optics lattice is set based on a particle of constant energy. As discussed in section 3.2, a particle travelling along a beam-line can emit SR and therefore lose energy. As soon as this occurs the particle is no longer at the constant energy for which the lattice was designed. At each successive magnet the decreasing energy of the particle will cause a larger change in trajectory compared to the nominal constant energy particle. For a transport line with large bends this will eventually lead to the particle deviating from the nominal orbit. To counter this effect the field strength of each magnet along the beam-line can be lowered by a calculable amount so that the energy of the particle (or mean energy of a bunch) is such that the trajectory is inline with that of the theoretical constant energy particle. By successively correcting the magnet strengths in this way the orbit of the energy losing particle can be stabilised near to that of the nominal particle.

Although the automatic re-scaling of magnets was included in the early versions of BDSIM, major updates to the infrastructure of later releases had rendered the original implementation obsolete. For beam transport along the main BDS the optics has been partly motivated to reduce the energy loss and so the need for re-scaling the simulated magnets was not critical. However, the extraction lines are expected to handle highly disrupted bunches with a large energy range and so re-scaling of magnet strengths becomes an important issue. An appropriate re-scaling implementation was therefore developed.

To calculate the amount by which a magnet strength must be scaled requires knowledge of the mean energy of a bunch at the start of the magnet. Due to the disrupted nature of the post-collision beams in the extraction line it was decided that a purely analytical solution to this problem should be preceded by a more practical solution using a pilot bunch. This bunch would be tracked along the entire beam-line to re-scale all the magnet strengths before the usual simulations are allowed to take place. A phase space ellipse comprising of 200 particles is therefore generated based on the disrupted IP parameters. As BDSIM is a single particle tracking simulation this requires careful manipulation of the GEANT4 tracking stack so that the particles are sequentially tracked from start to end of an element. At this stage their mean energy is calculated and the field strength of the next element is accordingly modified as a direct ratio of this mean energy to the nominal energy. The pilot bunch is stepped through each lattice element according to this method until all magnet strengths have been re-scaled.

The implementation of automatic re-scaling has been tested on a simple lattice with overly large sectorbend angles to assist in highlighting any differences seen, Fig. 6.12. As a reference the on-axis orbit for tracking a particle with SR processes turned off has been supplied. With no re-scaling of magnet strengths the nominal particle soon loses energy and deviates by a large amount from the reference orbit. The same particle tracked after re-scaling shows a significant reduction in this deviation. The observed differences between reference and re-scaled orbits is due to the fact that although the magnet strength is altered according to the incident particle energy, it is not possible to account for SR losses within the magnet.

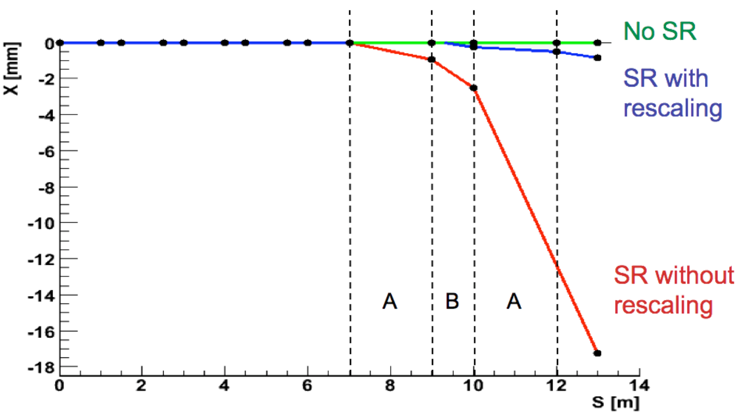

Figure 6.12: Effect of magnet re-scaling implemented in BDSIM by tracking a single particle along a short test lattice with unreasonably large angle sectorbends to emphasise differences. Region A corresponds to a sectorbend whereas B is a drift.

Chapter 7

Interaction Regions

To allow the physics potential of the ILC to be fully realised, the detectors in the Interaction Region (IR) must be located in an environment that allows them to discriminate between signal and background. The large field gradients of the final quadrupoles can lead to high background in the IR from the focussing of beam halo. The intensity of the collisions can also lead to high power radiation from beam-beam effects. Simulation studies are therefore essential to ensure that the background levels are tolerable within the IR – in terms of both signal detection and also machine protection issues.

The design of the ILC currently accommodates two Interaction Regions (IRs) with 14 mrad crossing angles at the IP. This scheme is a recent addition (September 2006) motivated by civil engineering cost issues as well as the results from numerous performance evaluations of the previous configuration such as those outlined in this chapter.

Historically, the baseline configuration of the ILC allowed for the Interaction Region (IR) to come in two different forms: a small (2 mrad) crossing angle region, and a large (14-20 mrad) angle design. The larger crossing angle was a relatively mature design that allowed for separate incoming and outgoing delivery lines. The flexibility provided by such a design potentially catered for a greater freedom in the choice of beam conditions and machine parameters. In contrast to this, the small crossing angle scheme was a more recent design that relied on shared incoming and outgoing magnets in the immediate vicinity of the IR. An advantage gained by this is that it allowed for less leakage of interesting collision interactions and so provided good hermeticity. This is especially important for low angle electron tagging required for vetoing spectator leptons down to very small scattering angles during slepton pair production studies [61]. An overview of both of these crossing angle schemes is given in the following sections.

Due to the large amount of R&D that has already been devoted to the development and refining of the large crossing angle, the following studies are largely concentrated upon investigating the feasibility of the 2 mrad design.

7.1 Crossing Angle Overview

One of the main distinctions in the design of small and large crossing angles is the handling of incoming and outgoing beams in the final doublet (FD) and detector region. The large crossing angle keeps the FD optics distinct and separate to the extraction optics. The generic layout for such a design is given in Fig. 7.1. It should be noted that the lower limit of 14 mrad is set from the smallest crossing angle that allows for separate delivery and extraction lines in the space provided whilst accounting for realistic magnet sizes.

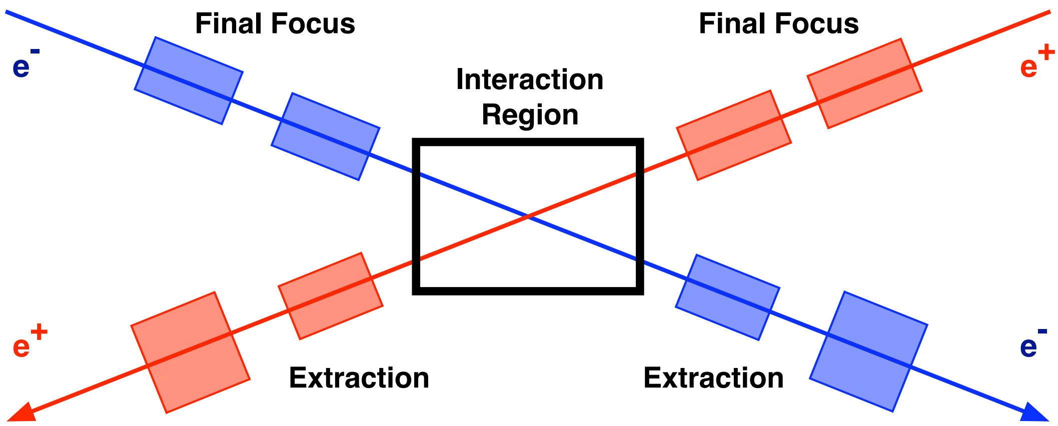

Figure 7.1: Schematic of large crossing angle design – not to scale.

In contrast to the 14 and 20 mrad schemes, the small crossing angle design makes use of shared magnets for both the incoming and outgoing beams, Fig. 7.2. This is achieved by taking advantage of the off-axis and angled entry of the disrupted beam into the field aperture of the first FD quadrupole after the IP – causing the beam to experience a dipole-like trajectory kick. By optimising the field strengths, aperture sizes, and distances between the FD magnets it is possible for the disrupted beam to pass through the pocket region of the second quadrupole, where the field strength is negligible. At this stage it is possible to separate the beam delivery and extraction lines. Chapter 8 contains a full description and detailed studies of the various extraction line options.

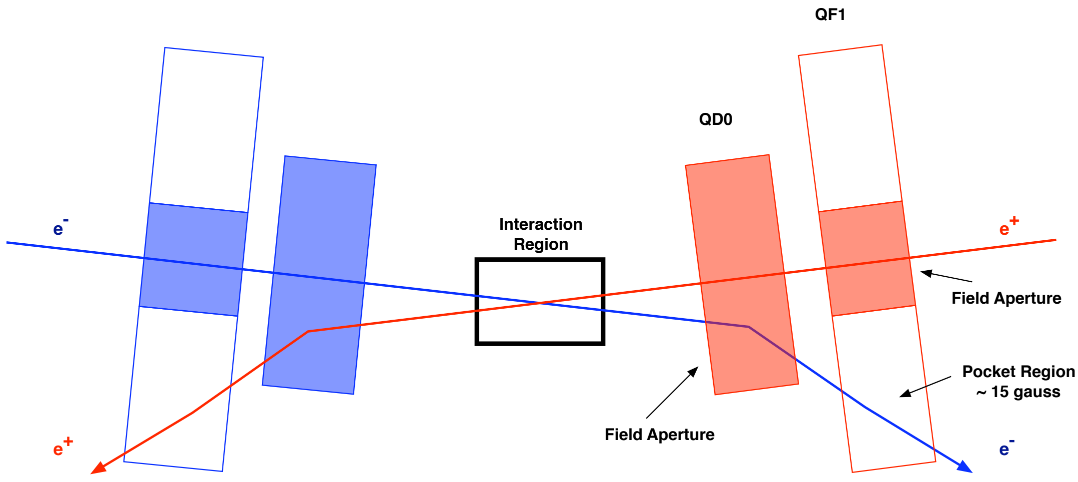

Figure 7.2: Schematic of small (non-zero) crossing angle design – not to scale.

Due to the combined nature of the incoming and outgoing beam optics for the small crossing angle design, optimisation of either system inherently requires careful consideration of the implications on both optics designs. The margin of error for successfully extracting the disrupted beam is extremely small and as such minor alterations to magnet strengths and beam conditions must be kept in check. The following studies investigate the ramifications of situations such as the impingement of halo material on magnet apertures used in the 2 mrad optics design.

7.1.1 Luminosity Issues

The extraction techniques available to the 2 mrad design put potential limits on the manageable beam luminosity. It follows that a higher luminosity will result in a more disrupted post-collision beam, the energy spread of which will cause problems for the shared magnet scheme. The separate beam-lines incorporated into the large crossing angle designs provide the tuning capability for a greater luminosity reach.

A crossing angle can result in a loss in luminosity due to the relative bunch orientation at the IP. Assuming no beam offsets or pinch effect, the reduced luminosity due to a crossing angle θ can be expressed as [62]:

$$\mathcal{L} = \mathcal{L}_0 \frac{1}{\sqrt{1 + \left(\frac{\sigma_z}{\sigma_x} tan\frac{\theta}{2}\right)}} \tag{7.1}$$

If the angle is between zero and $\sim\sigma_x/\sigma_z$ then there will be only minimal luminosity loss [63]. The 0.5 TeV nominal IP parameters dictate that this upper limit is $\sim$2.2 mrad, which motivates the size of the small crossing angle design. For the 20 mrad scheme the luminosity lost is $\sim$75% using nominal bunch parameters and $\sim$85% for the 14 mrad design [28]. Essential R&D has therefore been invested into the development of crab cavities that can be used to rotate the bunch prior to final focussing, Fig. 7.3. Crab cavities are expected to reduce luminosity loss to less than 2% – but have a very tight margin of error on phase stability. This is a direct result of requiring a crab cavity for each incoming beam line as any phase error between them can cause the two beams to receive different levels of transverse kick - which can lead to an offset at the IP. Although not as significant as the larger crossing angles, the 2 mrad design also suffers from angle-related luminosity losses on the order of 10% for nominal bunches. However, upstream crab cavities could potentially be used to reduce this luminosity loss.

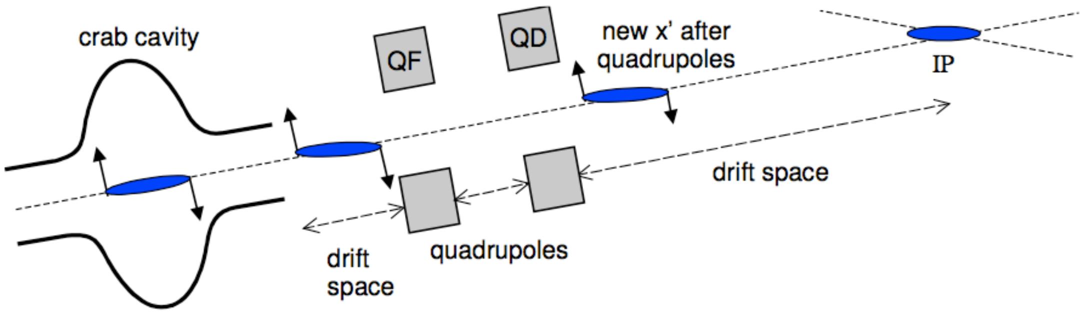

Figure 7.3: Schematic representation of crab crossing [64].

7.1.2 Alternative Designs

A second option for the small crossing angle has recently been suggested as a revival of the head-on crossing scheme. A zero mrad crossing angle was originally proposed as part of the TESLA technical design review (TDR) [65]. Post-collision bunches required separation from the main beam-line shortly after the IP using electrostatic separators. Until recently, the radiation levels and high beam power specified by the ILC configuration meant that this technique was not a viable option. Several options have recently been discussed for extracting the beam – whereby either the electrostatic separator is replaced with an ultra-fast RF-kicker [66], or the extraction optics is optimised to reduce the kick needed by the electrostatic separator [67]. Owing to the infancy of the head-on scheme, and hence the lack of studied extraction line optics, this design will not be studied in this thesis.

7.2 Simulation of the Interaction Region

The IR was included into BDSIM with the use of the purposely written Mokka interface (see section 6.5), where the detailed geometry was based upon the “Stahl” design [68] shown in Fig. 7.4. All elements of this design were included as accurately as possible with respect to their size, layout and material type. A 3D visual output of the BDSIM geometry for this is given in Fig. 7.5 in which the quadrupole has not been included. The electromagnetic and hadronic calorimeters (ECAL and HCAL) were not implemented as sensitive components for the purpose of these studies. To decrease simulation time and output file size these components were merely included in the simulations as solid blocks of appropriately sized material so that their shielding effects could be accounted for.

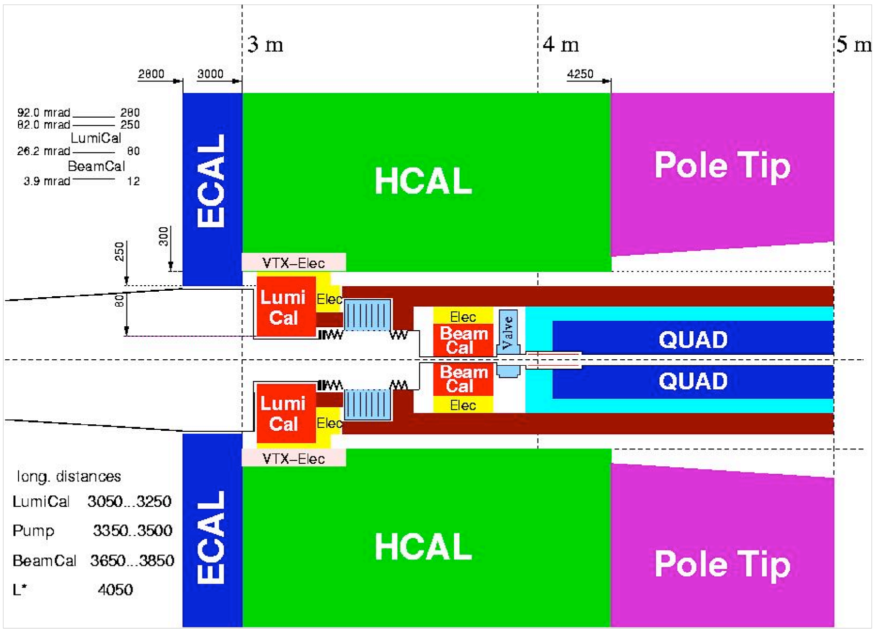

Figure 7.4: Proposed design for the IR for L*≤4.05 m [68].

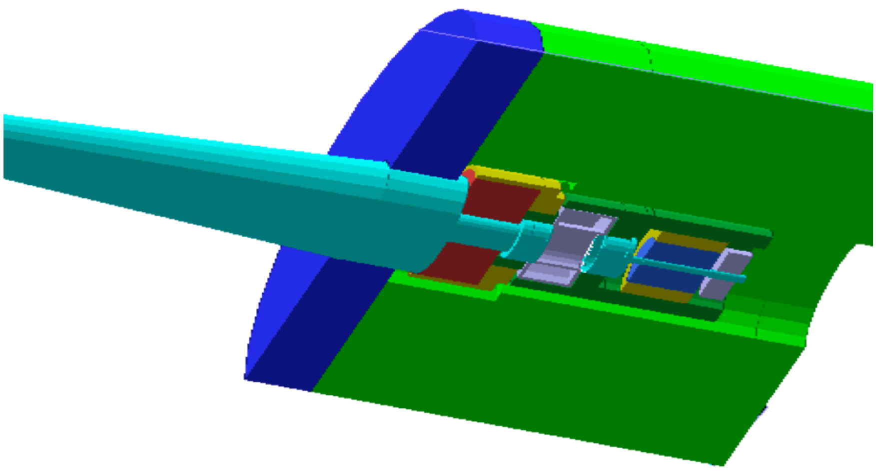

Figure 7.5: Cut away and rotated view of a section of the IR as modelled in BDSIM.

In order to include a realistic solenoid field within the IR a field map file from the Silicon Detector (SiD) concept group was used. No detector integrated dipole was included in this field map, leaving the field as illustrated in Fig. 7.6.

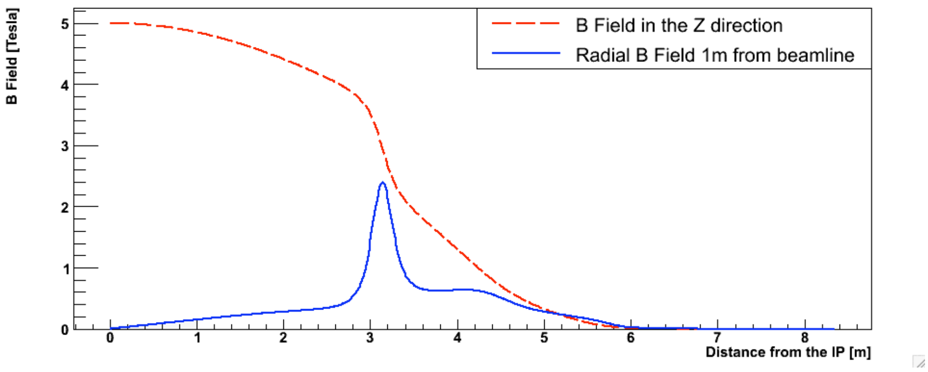

Figure 7.6: SiD field map.

7.3 Halo Collimation Depths

One of the driving motivations for an e^+/e^- linear collider is the potentially "clean" physics environment in which to make high precision studies. As discussed in section 2.4.1 this derives from the fundamental nature of the colliding particles. Nonetheless, this advantage is lost if the machine-related backgrounds in the detector become unaccountably large. The post-linac collimation system is assigned the responsibility of removing stray particles that would otherwise add to this background in the IR. With this performance goal in mind, the collimation system must also make provisions for the following:

- **Machine protection**

  The beam parameters as described in section 4.3 can be used to estimate the beam power for a train of 2820 bunches to be ∼11.3 MW for the 0.5 TeV CM nominal baseline configuration and ∼18 MW for the 1.0 TeV CM nominal upgrade option. No single beam-line component or collimator is able to tolerate this full power, and indeed R&D is still underway for viable beam dump solutions. However, in conjunction with responsive feedback from beam diagnostic equipment the collimation system must provide a certain degree of passive machine protection from at least the first few bunches in a train – each of which accounts for several thousand watts.

- **Collimator survival**

  Linked with the above goal of machine protection is the survivability of the collimators, which must be able to operate without too large a risk of being destroyed. Techniques for providing renewable and consumable collimators have been suggested for the NLC and could be viable options for the ILC [69].

- **Muon Production**

  Whilst attempting to remove beam halo and stray particles in the beam-line, the collimation system can itself become a potential background source for muons. As discussed in section 3.6, the resulting muon flux can be detrimental to both the detector signal and also personnel protection in the experimental halls.

- **Wakefield Kicks**

  The collimator jaws inserted into the beam-line can introduce both geometrical and resistive wakefield kicks as mentioned in section 3.1.3. In addition to potentially repopulating the beam halo, these kicks can also lead to beam misalignment. Experimental tests on the spoiler wakefields have been proposed [70, 71], with the latest results available at [72].

The common approach to particle collimation is to use a thin spoiler of $\sim$1 radiation length (X_0) in conjunction with a large absorber of $\sim$20-30 X_0. As illustrated in Fig. 7.7, the absorber is placed downstream in the spoiler's shadow and has a larger aperture to reduce wakefield effects. Hitting the thin spoiler will cause a high energy particle to undergo multiple Coulomb scattering; the resultant spread of secondary particles reduces the beam energy density to tolerable levels for the absorber. The thickness of the absorber is set at a high number of radiation lengths to maximise containment.

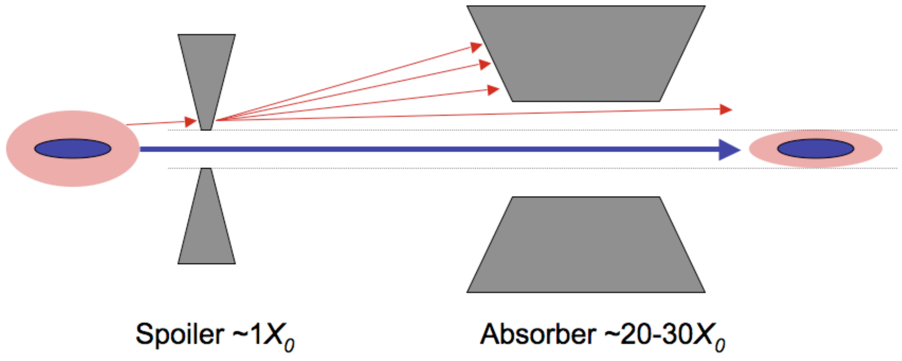

Figure 7.7: Schematic representation of the spoiler/absorber collimation set up

The collimation system is unable to remove all beam halo which leads to the generation of SR in the FD quadrupoles. This SR translates into a direct threat to sensitive components such as the Vertex Detector (VXD) – either by direct hits or by scattering backwards from downstream components. The minimisation of this effect enforces the requirement on halo collimation depths. Halo collimation depths are typically given in units of $\sigma_{x,y}$ where the values correspond to the number of each sigma ($N_{x,y}$) that the upstream collimator apertures need to be set at in order to achieve the necessary collimation. The collimators are therefore set to a depth that removes particles with a phase space amplitude that would lead to unacceptable SR production in the final focusing magnets.

7.3.1 Method

The collimation depth can be calculated for the 2 mrad design by generating a halo distribution at the exit of the linac and then tracking it through the BDS down to the IR using tracking simulation packages such as BDSIM. However, tracking the necessary amount of particles along approximately 2 km of optics can prove to be time consuming – especially when considering all of the permutations of σ_x and σ_y values that need to be assessed. Local calculations of the collimation depth – where only the FD and IR sections of the BDS are considered – can be therefore be made, with a view to taking the results and then tracking through the entire BDS. This technique makes the assumption that the upstream collimators have exactly achieved a given σ_x and σ_y collimation depth. By taking the known particle distribution parameters at the entrance to the FD, it is possible to reconstruct the halo distribution that is within the set collimation depth. Following this method, halo distributions were tracked through the IR using collimation settings from $N_x = 9$ to $12.5\sigma_x$ and $N_y = 0.5$ to $80\sigma_y$ in steps of $0.5\sigma_{x,y}$.

7.3.2 Results

The most constraining aperture in the IR is the inner radius of the beam calorimeter (see "Beam Cal" in Fig. 7.4). In the 2 mrad crossing angle design this 15 mm radius component is situated approximately 4 m from the IP. The crossing angle of the incoming and outgoing beamline result in the SR photons seeing an off-axis and tilted aperture. Using the off-axis post-IP beam calorimeter as the constraining aperture a collimation depth map has been produced (see Fig. 7.8a) where each N_x/N_y combination is weighted with the area of the SR distribution that hits the beam calorimeter. From this map it appears that the N_x is limited to $9\sigma_x$ whilst N_y is limited to $69\sigma_y$. The next constraining aperture after the beam calorimeter is the trapezoidal opening between the poles of the warm FD quadrupole (QF1). See Fig. 7.9 for details of QF1. The outgoing beam passes through this region – usually referred to as the pocket (see Fig. 7.2). Using the assumption that the beam calorimeter is not present, a second collimation depth map has been produced using the QF1 pocket (see Fig. 7.8b) as a constraining aperture. Based on this aperture N_x is limited to $10.5\sigma_x$ and N_y to $45\sigma_y$.

Taking into account both sets of results it is evident that the horizontal collimation depth limit is set by the beam calorimeter whilst the vertical limit is set by the QF1 pocket. The minimum collimation depth that the upstream collimation system must achieve is therefore $N_x = 9\sigma_x$ and $N_y = 45\sigma_y$.

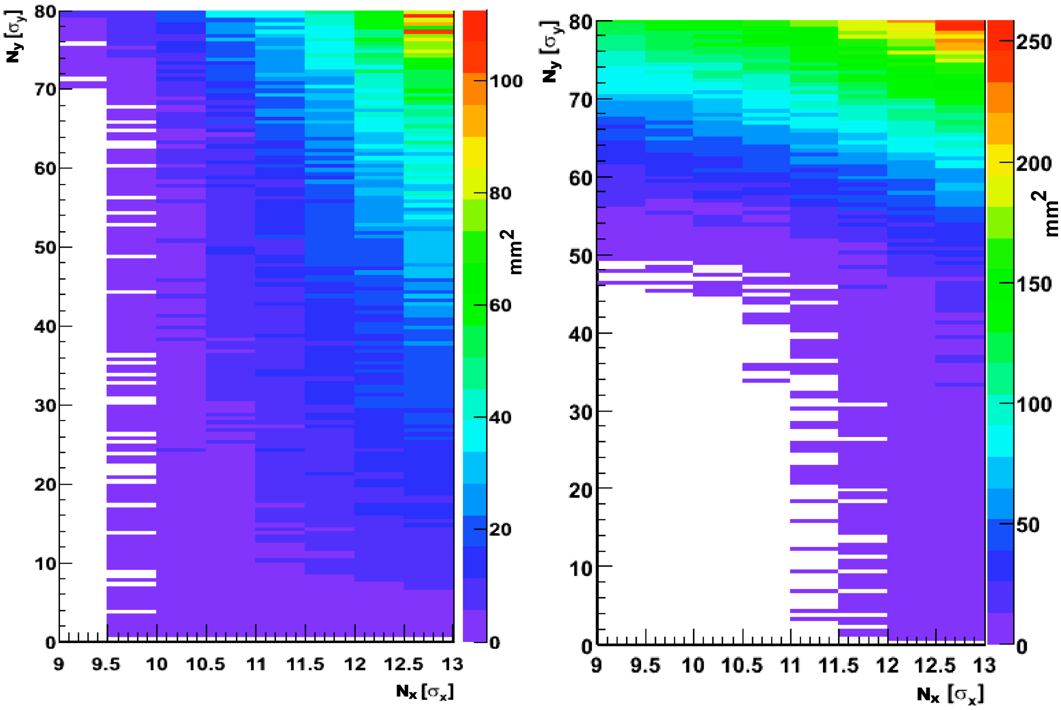

(a) (b)

Figure 7.8: Halo SR hit density on (a) the beam calorimeter and (b) QF1 post-IP for N_x Vs. N_y.

7.4 Synchrotron Radiation Back-scattering

Halo particles within the collimation limits will pass through the FD optics and generate a large amount of SR as discussed in section 3.2. As described in the previous section the collimation should be set such that no halo-related particles impinge upon an aperture with the detector region. However, a non-perfect collimation system and effects such as beam orbit offsets in the solenoid field can give rise to a certain amount of SR landing on the face of QF1. Detailed studies were carried out to track the SR photons and check the back-scattering rate to assess the potential addition to background in the VXD. For a silicon-based VXD most photons will either pass straight through or will convert in inert parts of the detector (such as the housing and fittings). Back-scattered photons that can

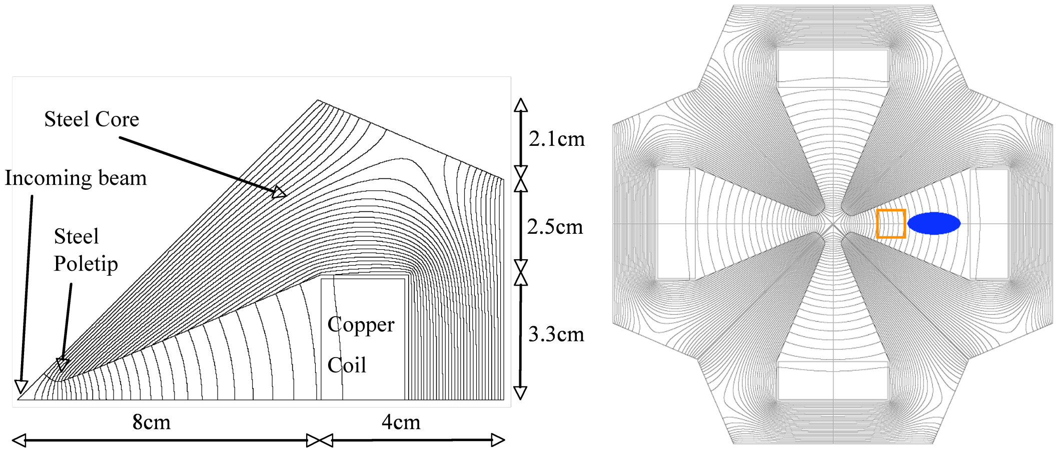

(a) One octant of the magnet design [73].

(b) Head-on view of QF1. The incoming beam travels down the centre of the quadruple. The outgoing beam (denoted by the blue area) and beamstrahlung photons (orange square) travel through the pocket.

Figure 7.9: QF1 – the warm technology quadrupole in the FD.

be mistakenly accepted as minimum ionising candidates are those that convert within the active thickness (approximately 20 μm) of each layer of the VXD. Photons in the energy range of 1 to 10 keV are therefore most likely to add to the background of the VXD [74].

7.4.1 Method

Following a similar method to the halo collimation depth studies, a halo distribution can be tracked through the IR along with any generated SR. Information regarding the production point and back-scattering paths of the SR can be analysed to provide a detailed study of the potential background risk to the VXD. For this study a distribution resulting from a halo collimation depth of 13 σ_x and 80 σ_y was chosen as from Fig. 7.8b. This maximises the amount of SR falling on the face of QF1 – and in this way ensures that the most pessimistic scenario for back-scattering is dealt with. The study was performed using 5 $\times$

10^5 halo particles with energies of 500$\pm$10 GeV. The BDSIM simulation was configured to track charged particles down to 10 keV. In order to properly address the issue of photon conversion in the VXD, the photons were tracked to 1 keV .

7.4.2 Results

The SR photons were tracked from their production point (see Fig. 7.10a) to the front face of QF1. The energy and spatial distribution of these photons at this point is given in Fig. 7.11. The majority of these photons continue to travel through the open apertures between the poles of QF1 and are no longer tracked in BDSIM for the purposes of this study. Those photons incident upon the material of QF1 are fully tracked and any photons arriving at the IP plane are recorded. Fig. 7.10b shows the production point of all photons travelling through the IP plane. Many of these particles originated from the upstream FD and are back-scattered to the IP. Photons that originated after the IP are either from SR generated in QD1 and directly back-scattered or from photons that have interacted with the material of the beampipe or magnets and been re-emitted as photons in the direction of the IP.

The VXD is susceptible to an increase in the background from incident photons with an energy of less than or equal to 10 keV. The energy spectrum of the back-scattered photons at the IP plane, shown in Fig. 7.12a, indicates that with the limited sample of halo fired there are no photons with an energy that could unaccountably add to the VXD background. Moreover, from Fig. 7.12b, it is evident that although there are a significant number of photons back-scattered and reaching the IP plane, the majority of these are outside of the VXD radius of 14 cm – leaving a back-scattered hit rate upon the VXD of 1×10^{-5}. Taking into account both the energy and probability of a back-scatter, along with the fact that the study was purposely set up with the worst case scenario for the area of QF1 directly hit by the SR, then the back-scattered rate to the VXD is acceptable.

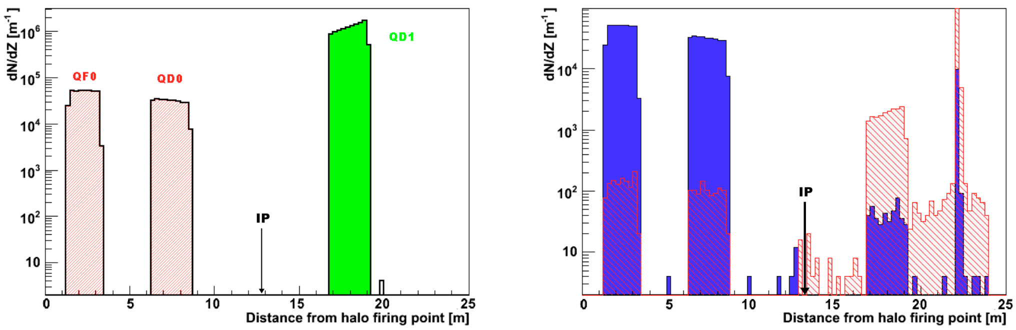

(a) The crossed region represents photons generated in the quadrupoles upstream of the IP. The shaded region represents those generated in QD1 – which is downstream of the IP.

(b) Shaded region represents the production point of photons that are crossing the IP plane whilst travelling from the incoming optics to the extraction line. The crossed regions show the production point of photons that are travelling in the opposite direction.

Figure 7.10: Production point of SR photons found at QF1 (a) and crossing the IP (b).

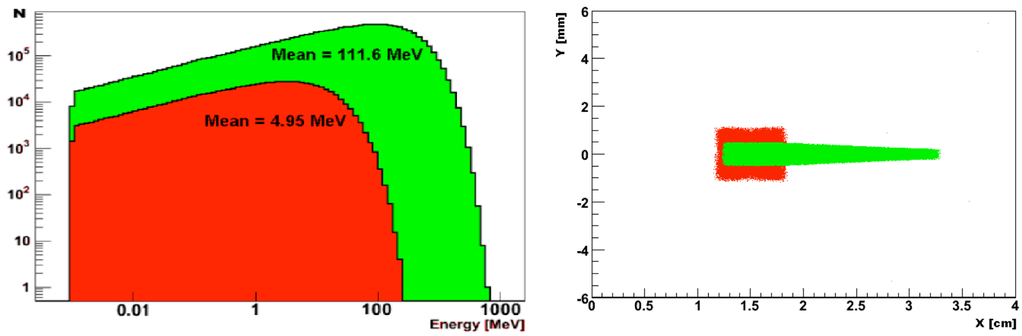

(a)

(b)

Figure 7.11: The energy (a) and position (b) of SR Photons incident upon the face of QF1. The red (dark) shaded regions represent photons generated in the quadrupoles upstream of the IP. The green (light) regions represent those generated in QD1 – which is downstream of the IP.

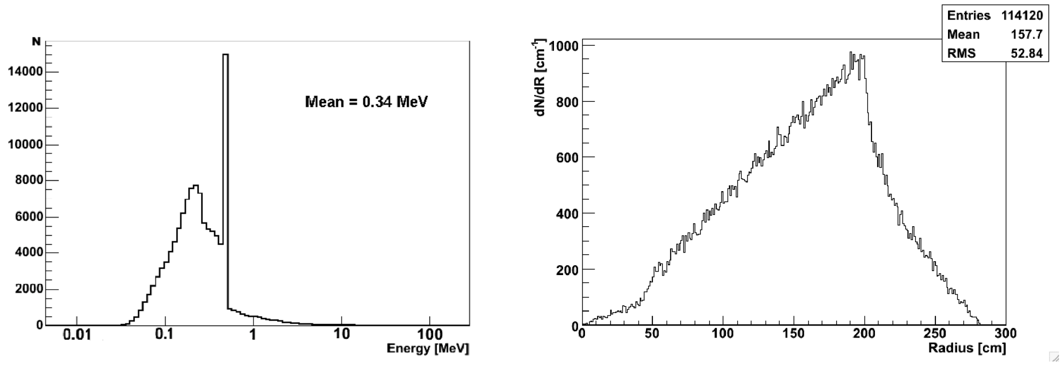

(a) (b)

Figure 7.12: The energy (a) and radius (b) of photons reaching the IP as a result of back-scattering from the face of QF1.

7.5 Radiative Bhabha Backgrounds

As mentioned in section 3.5, Radiative Bhabha particles produced in the IR can lead to an undesired power load on the nearby focussing elements. These superconducting quadrupoles have a very tight power deposition limit set on them in order to avoid quenching. Quenching occurs when the superconducting state of the coils is compromised by localised power depositions within them. This can very quickly lead to the loss of the superconductivity and would result in the immediate ceasing of operations at the ILC and several hours/days of downtime. In view of this a detailed simulation study has been carried out to gauge the danger to the nearest superconducting quadrupole (QD0/1) in the 2 mrad IR. This design utilises a quadrupole similar in specifications to the superconducting quadrupoles that are planed for use in the Large Hadron Collider (LHC). Quenching limits for these magnets require that the peak power density should not exceed 1.5 mW/g, however due to the proximity of QD0 to the radiation levels generated in the IR this has been reduced to 0.5 mW/g to include a relatively large safety factor.

7.5.1 Method

BDSIM typically provides power losses from the beam onto the elements as a power per meter value. For this study however, it was necessary to track the power deposition and particle showers through the material of QD0 to look for localised power densities. BDSIM was therefore modified for this study to enable the scoring of the QD0 element such that energy deposits could be accounted for in a number of small and well defined sub-volumes. This was achieved by checking the location of each energy deposit within QD0 and binning the results accordingly. QD0 was in this way divided into 3×10^5 volumes each storing a running total of energy deposits throughout the duration of the simulation. By knowing the material density and volume of each of these regions it is possible to calculate the localised power densities throughout the entire magnet. The scoring of the magnet volume was accomplished by dividing it into 1 cm planes along the beamline axis, and then dividing each plane into 6 rings, each containing 200 radial divisions (see Fig. 7.13 and Table 7.1 for details). The quadrupole was built up in the simulation with a moderate amount of detail. It consisted of a 1 mm aluminium beampipe and a NbTi superconducting coil with a density of 5.6 g/cm^3 set at a temperature of 4 Kelvin. For the purposes of this study, the NbTi coil was assumed to be a solid block with no support structure or insulation material accounted for.

Table 7.1: Ring properties used for the scoring of QD0.

Ring Number	**1**	**2**	**3**	**4**	**5**	**6**
Radii [cm]	3.4 – 3.5	3.5 – 4.0	4.0 – 5.0	5.0 – 8.0	8.0 – 13.0	13.0 – 20.0
Material	Al	NbTi	NbTi	NbTi	NbTi	NbTi

The study was run using the Radiative Bhabhas produced by the Guinea-Pig [75] beam-beam simulation program as bunch inputs to BDSIM. Four different machine parameters were used: nominal and high luminosity beam parameters for both the 0.5 and 1.0 TeV configurations. The choice of these parameter sets arises from the fact that the en-

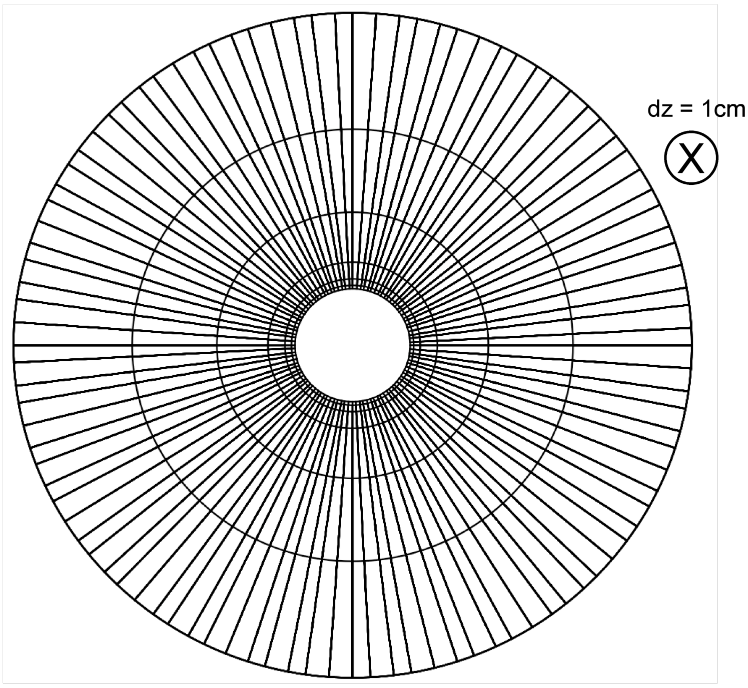

Figure 7.13: Illustration of the scoring of QD0.

ergy lost by beam particles to radiative Bhabhas is directly proportional to the luminosity. Hence nominal conditions and high luminosity cases where chosen with no beam-beam offsets (as loss of luminosity due to beam offset would lead to negligible radiative Bhabha power). In this way, the nominal and worst case scenarios are evaluated.

7.5.2 Results

The simulation results are presented in Table 7.2. It is clear that for all machine parameter configurations the localised power densities within the superconducting coils exceeds the recommended minimum for the quench limit. Power deposition maps for each scored ring of QD0 for the 0.5 TeV Nominal case are presented in Fig. 7.14 where it is evident that all the losses are on one side of the magnet. This is a result of both the crossing angle and also the fact that the particles have the same charge – all electron and positron Radiative Bhabha particles leave the IP back-to-back.

In an attempt to reduce the peak power density in QD0, tungsten was placed as a

Table 7.2: QD0 Power Losses in the 2 mrad design

	Incident Power [W]	**Total Power Deposited in Beampipe and Coils [W] ($R < 20$ cm)**	**Peak Power Density in Beampipe [mW/g]**	**Peak Power Density in NbTi Coils [mW/g]**
0.5 TeV Nom.	0.45 ± 0.01	0.27 ± 0.01	0.71 ± 0.03	1.90 ± 0.07
0.5 TeV High Lumi.	1.07 ± 0.09	0.60 ± 0.05	1.60 ± 0.15	4.27 ± 0.41
1.0 TeV Nom.	1.12 ± 0.07	0.65 ± 0.04	1.35 ± 0.08	4.11 ± 0.23
1.0 TeV High Lumi.	3.61 ± 0.31	2.08 ± 0.18	4.41 ± 0.38	13.7 ± 1.20

liner to the beampipe. The liner thickness was set to 3 mm, which is approximately one radiation length. Results for the power deposition simulations with this liner in place are presented in Table 7.3. Due to the reduction in effective aperture size after the addition of the tungsten liner, the incident power is seen to increase by 30-40%. The liner does, however, succeed in reducing the peak power density in the coils by more than 92% for all parameter cases. The 1.0 TeV high luminosity configuration continues to result in peak power loads in the quadrupole that are greater than the minimum safety value of 0.5 mW/g. However, it is worth noting that this is still below the original LHC limit of 1.5 mW/g for this magnet type. The reduction of the coil peak power densities are illustrated in Fig. 7.15.

This study appears to indicate that the power loss on the 2 mrad QD0 magnet from Radiative Bhabha particles can be tolerated if shielding methods such as the insertion of a tungsten liner are accounted for. However, further studies into the effects that this liner has on magnet operation and design are required to insure its feasibility. It should also be noted that the version of GEANT4 used by BDSIM in these studies is unable to simulate time-dependent properties of materials such as heat conduction and other heating effects (e.g. expansion/destruction of materials). The results of this study may therefore be altered by the introduction of such material characteristics and indeed appropriate methods for

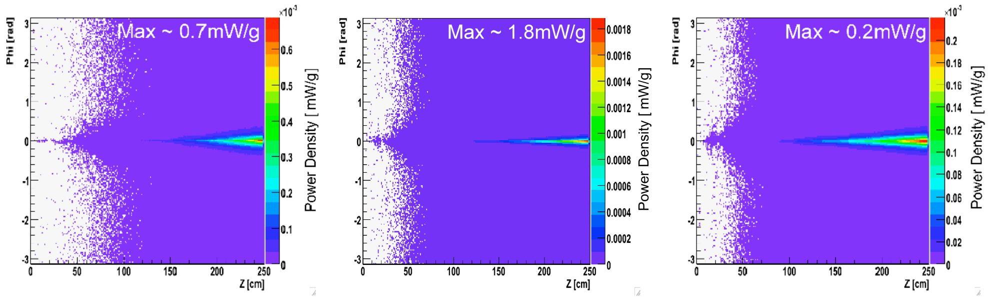

(a) Ring 1 – Aluminium beampipe

(b) Ring 2 – NbTi Coil

(c) Ring 3 – NbTi Coil

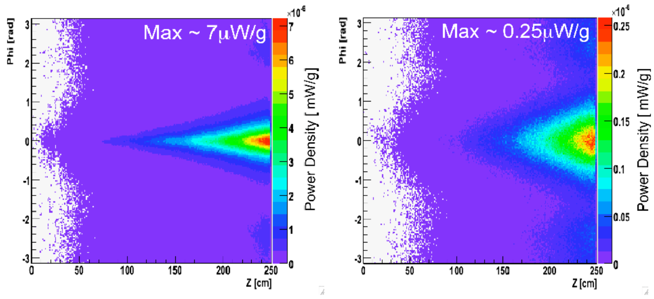

(d) Ring 4 – NbTi Coil

(e) Ring 5 – NbTi Coil

Figure 7.14: Power density maps for the first 5 rings of QD0 for 0.5 TeV nominal Radiative Bhabha particles. Peak power density occurs in the first ring of the NbTi coil. The 6th ring had no energy deposits.

controlling the heat load upon the tungsten liner should be taken into consideration.

Table 7.3: QD0 Power Losses in the 2 mrad design with Tungsten Liner.

	Incident Power [W]	**Total Power Deposited in Beampipe and Coils [W] ($R < 20$ cm)**	**Peak Power Density in Beampipe [mW/g]**	**Peak Power Density in NbTi Coils [mW/g]**
0.5 TeV Nom.	0.61 ± 0.02	$0.13 \pm .004$	0.26 ± 0.01	0.11 ± 0.01
0.5 TeV High Lumi.	1.44 ± 0.12	0.32 ± 0.03	0.61 ± 0.05	0.27 ± 0.02
1.0 TeV Nom.	1.49 ± 0.09	0.34 ± 0.02	0.67 ± 0.04	0.30 ± 0.02
1.0 TeV High Lumi.	4.95 ± 0.43	0.69 ± 0.07	1.40 ± 0.15	0.62 ± 0.07

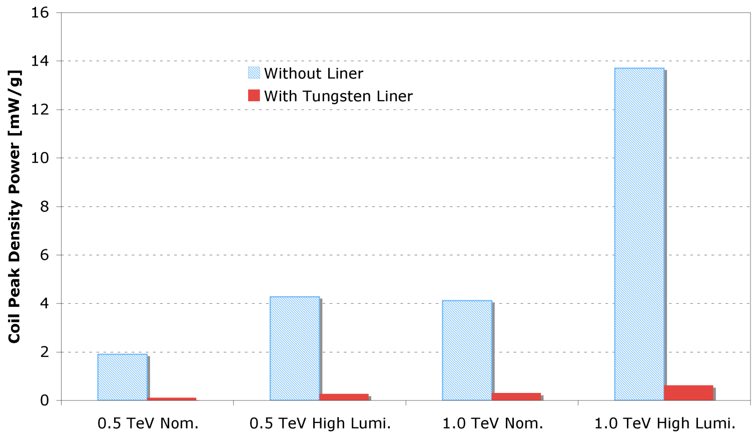

Figure 7.15: Comparison of the peak power densities in the NbTi superconducting coils of QD0 with and without a tungsten liner.

Chapter 8

Beam Delivery and Extraction Lines

Beam transportation plays a crucial role in achieving the performance goals of the ILC. Once the beam has been accelerated to the collision energy it must be delivered to the IP, collided, and subsequently transported to the beam dumps. This must all be safely accomplished whilst simultaneously considering the delivered luminosity, transportation-induced detector background levels, and general protection issues. A multitude of beam diagnostic tools – such as the Laser-wire detailed in Chapter 5 – are therefore employed by the transport lines to provide essential feedback on beam conditions. Performance studies for the BDS and a comprehensive set of power loss evaluations of the proposed extraction lines are discussed in this chapter.

8.1 Beam Delivery System

The BDS is entrusted with the task of transporting the beam from the exit of the main linac to the IP with nanometer precision. This is achieved with the use of a carefully designed arrangement of focusing and bending magnets that form an “optics lattice”. By controlling the magnetic fields in the beam’s path it is possible to condition the beam in preparation for collision at the IP. Throughout its transportation, the beam is monitored by a range of beam diagnostic instruments to ensure that its parameters are within a tolerable range. Fast feedback from these monitors can be used to correct minor deviations from the nominal beam conditions by performing operations such as orbit correction.

8.1.1 Layout

Historically, the baseline for the ILC contained one large crossing angle of 14-20 mrad and one small crossing angle of 0-2 mrad. The proposed layout for the 2 and 20 mrad options, Fig. 8.1, was referred to as the “strawman” design.

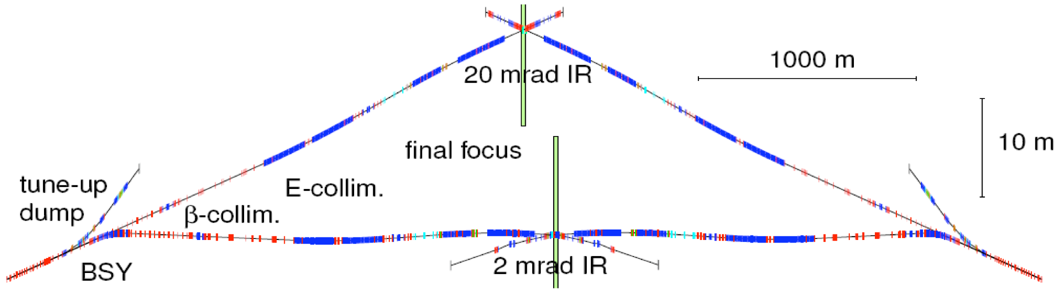

Figure 8.1: Proposed BDS “strawman” layout for 2 and 20 mrad [28]

The first few hundred meters of the BDS transports the beam from the exit of the main linac to the beam switch yard (BSY). If the beam is deemed to be within acceptable parameters then it can be directed to one of two crossing angles. The option of sending the beam to a tune-up dump is available as a tool for use during the commissioning of the main linac or as an emergency extraction point. Assuming that the beam exits the main linac within specifications then the beam-line optics should be able to transport it with only minor corrections from feedback systems. However, if one or more magnets were to fail – for example, in the case of a power loss – then a sudden change in beam orbit could occur. Considering the high power of the beam this could lead to a catastrophic failure in the case that the orbit were to shift enough that the beam landed directly upon an element aperture. Owing to the fact that a train of bunches can carry up to 18 MW of power, a few bunches can be sufficient to cause significant damage to beam-line components. Fast feedback is therefore essential to ensure that the beam can be dumped as soon as possible.

At the BSY the 2 mrad BDS veers away from that of the 20 mrad with a bend of $\sim$11 mrad – achieved by combined-function quadrupole and dipole magnets. Although the use of this large bend produces SR, it has the advantage of curving away from any linac collimation debris. A collimation system is positioned in both BDS's shortly after the BSY to remove wayward particles that could cause background in the IR's. The location of the collimators is optimally set to be as far from the IP's as possible to reduce the possibility of scattered particles reaching to the IR. The final focus systems then proceed to transport the beams to the IP.

As discussed in section 7.1, recent developments in the baseline configuration of the ILC have led to the introduction of a BDS layout for two 14 mrad crossing angles, Fig 8.2. The motivation for this change in layout is derived from both construction cost issues and also beam optics performance results such as those outline in the remainder of this chapter – which deals with the evaluation of the 2, 14, and 20 mrad extraction line designs for the small and large crossing angle layout.

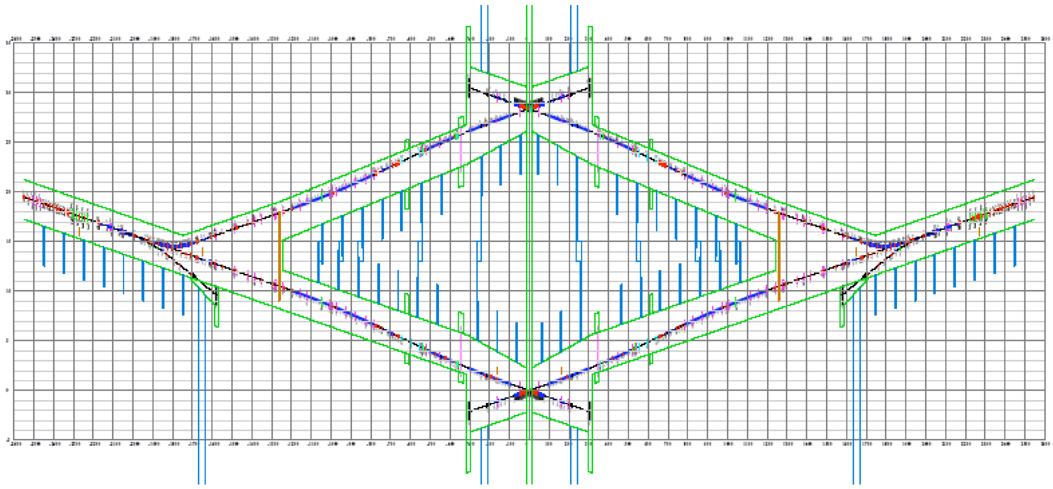

Figure 8.2: Proposed BDS "strawman" layout for 14/14 mrad [76]

8.2 Final Doublet

The last few magnets of the BDS are used to focus the beam down to approximately 5 nm vertical by 200 nm horizontal at the IP – entailing a demagnification of the beam by a factor of up to 200 times. This requires very high quadrupole gradients of approximately 200-300 T/m and as such the last focussing magnet in the lattice uses superconducting technology. The general approach to designing the final doublet is to pair up two quadrupoles with two sextupoles, Fig. 8.3. In keeping with the small vertical spot size, the final quadrupole is a horizontally defocusing (and hence vertically focusing) magnet.

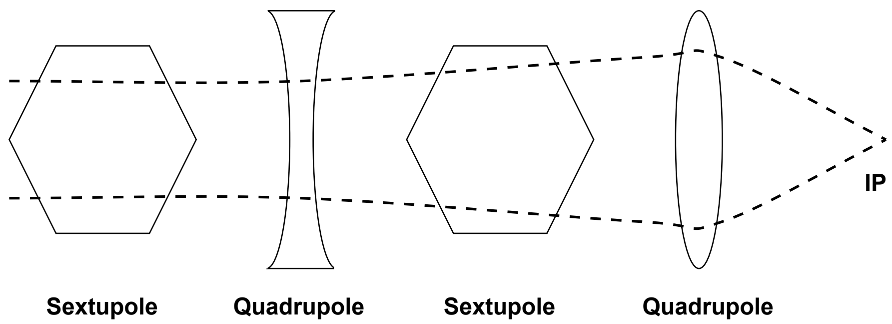

Figure 8.3: Schematic representation of the final doublet layout. The dash lines represent the beam envelope.

The sextupoles play a subtle role in the final doublet whereby they are used to counter the chromatic effect that would otherwise be evident. The chromatic effect refers to how the focal length of the magnet changes with the particle's momentum – as illustrated in Fig. 8.4. This effect is especially apparent at the IP due to the high focussing strength of the last quadrupole. A typical bunch arriving at the final doublet will have a finite energy spread which results in an enlargement of the spot size.

It follows that to correct for chromaticity, the higher energy particles must be over-focussed whilst the lower energy particles should be under-focussed. This can be achieved by positioning sextupoles in non-zero dispersion regions created by careful placement of weak dipoles further upstream. Although the chromaticity can be cancelled by careful

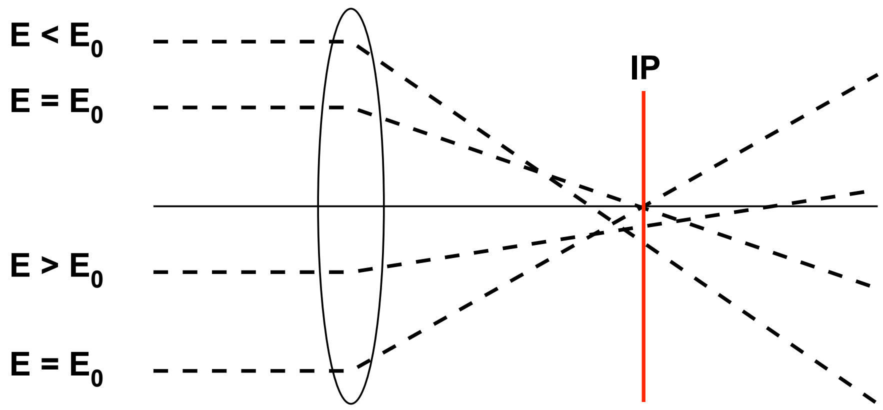

Figure 8.4: Schematic representation of the chromatic effect. The dash lines represent individual particles within a bunch.

placement of these sextupoles, non-linear terms lead to undesirable geometric effects that can enlarge the spot size by a similar order as the chromatic effect. These geometric aberrations can be cancelled by pairing the final doublet sextupoles with a second set placed 180° in betatron phase further upstream.

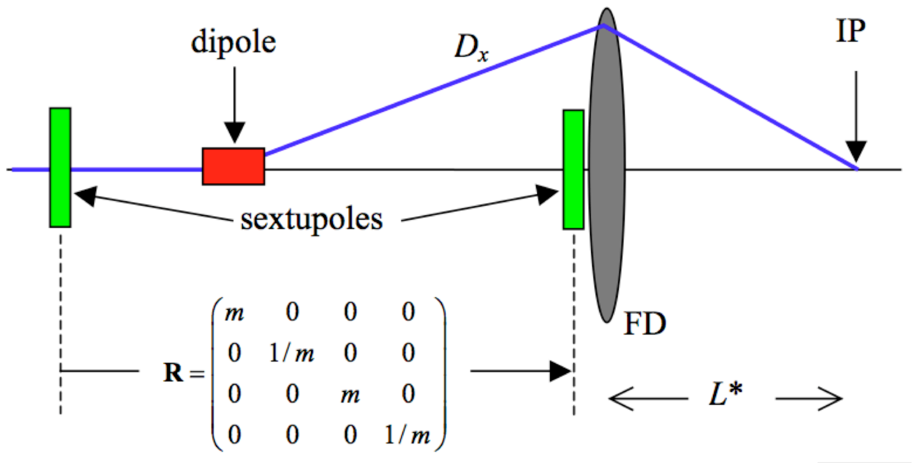

Figure 8.5: Schematic representation of the local chromatic correction scheme [77].

The final superconducting quadrupole is situated less than 5 m from the IP and is therefore positioned partly inside the detector region. The close proximity to the IP places the quadrupole in a vulnerable position in terms of post-collision backgrounds. Studies on the operational effects of beam-related power deposition within this quadrupole are presented in section 7.5.

8.3 Energy Collimation

In addition to the phase space collimation as described in section 7.3, energy collimation is also required. The optics lattice for the BDS is designed to transport nominal energy beams with a $\pm 10\%$ spread and so as part of the machine protection scheme, particles outside this energy acceptance must be collimated. The collimation is performed in a region of non-zero dispersion whereby the transverse displacement of a particle is correlated with its energy. In ILC BDS the dispersion for energy collimation is created in two locations with the use of chicanes. The first chicane houses the machine protection collimator and is located immediately before the BSY, Fig. 8.6. A beam position monitor (BPM) is positioned at the maximum dispersion point and is used to provide energy measurement feedback to the main linac. The second energy collimation chicane is located after the after the BDS betatron collimators and so are able to intersect their particle debris.

8.4 Extraction Lines

After the beams have been collided at the IP they are transported from the detector region by extraction beam-lines. As the post-collision bunches are highly disrupted and have a large energy and angular spread, careful design of the extraction line is required to ensure that the spent beam is carried to the beam dumps with minimal beam loss. Depending on the machine parameter configuration, the extracted power of the beam ranges from 10 to 17 MW. Although this is less than the power managed by the incoming beam-lines, the disrupted nature of the spent beams increases the stringent demands on the design of the extraction lines.

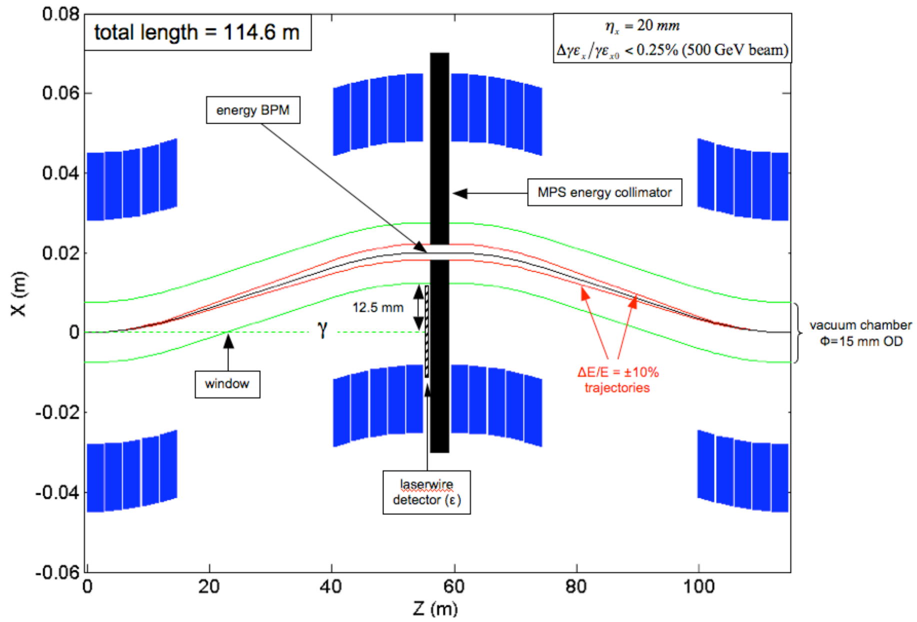

Figure 8.6: The energy collimation/diagnostic chicane [78]

8.4.1 Large Crossing Angle Extraction

One of the defining characteristics of the large crossing angle is that the incoming and outgoing beams use completely separate beam-lines, as illustrated by Fig. 7.1. This means that the optics lattice for the extraction line can be set up and fine tuned independent of the incoming lines. The close proximity of the first extraction magnet to the IP allows for early treatment of the divergence of the post-collision bunches. The large crossing angle is currently realised by two designs: a more mature 20 mrad scheme, and a recently proposed 14 mrad configuration. The latter being the smallest possible angle that can realistically accommodate separate incoming and outgoing magnets.

8.4.2 Small Crossing Angle Extraction

In contrast to the large crossing angle, the limited transverse space as a result of a small crossing angle does not allow for an entirely separate extraction line. Neglecting the detector solenoid field, simple geometric considerations dictate that with a crossing angle of 2 mrad the outgoing beam will be transversely separated from the opposite incoming beam by only 9 mm after the L* length of 4.5 m has been travelled. This means that the beam will pass through the 35 mm aperture of the final focussing quadrupole as illustrated by Fig. 7.2. However, the fact that the beam reaches this quadrupole both off-axis and at an angle results in it experiencing a dipole-like bending effect from the magnet's field. This an essential element in the design of the 2 mrad extraction line and by fine tuning of this field along with the next few components, it is possible to begin to separate the incoming and outgoing beam-lines some 15 m from the IP. However, even at this distance the 2 mrad design requires novel magnet designs that can house zero field regions for one beam-line and normal field regions for the other. In view of the shared nature of the last few magnets, it follows that the design process for the 2 mrad extraction is more difficult than the 20 mrad and that the margin for error is smaller.

8.4.3 Power Losses

A key estimation of the performance of an extraction line design is the level of power losses observed along the beam-line. Losses of below 100 W/m, if well understood, should be acceptable for the extraction lines to operate. Above this level the power loss may lead to destruction of components and suggests that the optics may need further optimisation. Particle tracking simulations have been performed for the 2, 14, and 20 mrad extraction line designs using BDSIM. The studies were carried out for both 0.5 and 1.0 TeV parameter sets under nominal and high luminosity conditions, and with zero and non-zero vertical offsets at the IP[1]. In addition to this, each parameter set was tracked with and without SR processes turned on in BDSIM. The full list of parameter sets used in the simulation of each extraction line design, along with the abbreviations that will be used to refer to them in the text, are given in Table 8.1.

[1]The post-collision bunches were simulated by the Guinea-Pig beam-beam simulation package [75]

Table 8.1: Machine parameter sets used for extraction line power loss simulations. Refer to Tables 4.4 and 4.5 for further beam condition details. The offset refers to the vertical beam-beam displacement at the collision point.

Abbreviation	**CM Energy [TeV]**	**Beam Conditiions**	**Offset [nm]**
cs11	0.5	Nominal	0
cs11-dy200	0.5	Nominal	200
cs15	0.5	High Lumi.	0
cs15-dy120	0.5	High Lumi.	120
cs21	1.0	Nominal	0
cs21-dy100	1.0	Nominal	100
cs25	1.0	High Lumi.	0
cs25-dy80	1.0	High Lumi.	80

Calculation Details

The simulations in BDSIM were configured to use the `stopTrack` option whereby a particle hitting a material is stopped and its total energy is logged as being deposited at that location. This greatly speeds up the computational time and also allows facilitates comparisons with other tracking-only codes. The total energy lost at a given location (E_{loss} in units of GeV) produced by BDSIM can be used to calculate the power loss (P_{loss} in units of watts) with the following expression:

$$P_{loss} = 1.6 \times 10^{-10} \frac{N_b f N_{beam}}{N_{sim}} E_{loss} \tag{8.1}$$

where N_b is the number of bunches in a train, f is the repetition rate of the machine (5 Hz for the 0.5 TeV and 4 Hz for the 1.0 TeV), N_{beam} is the number of particles populating a standard bunch (assumed as 2×10^{10}), and N_{sim} is the number of particles in the simulated bunch.

The tracking of the low energy tails of the disrupted bunch are especially important in assessing the extraction lines' ability to handle the post-collision energy spread. For this reason higher statistics were used in the low energy regions of the simulated bunch,

Fig. 8.7. To account for this difference, the resulting power loss from these particles was weighted according to the ratio of the core/tail overlap.

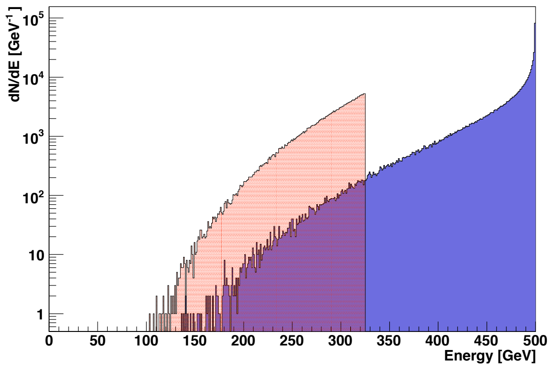

Figure 8.7: Example of the differences in statistics levels of the core and tail bunch files, in this case for the 1.0 TeV nominal, zero IP offset bunches.

2 mrad Results

Owing to the fact that the 2 mrad design is a relatively newer design compared to the 20 mrad, the losses have been given in terms of the first few key magnets and then the collimators. The losses for the cs11 parameter set, in the absence of SR, are less than 1 kW for all elements. However, cs11-dy200 suggests that the introduction of a 200 nm offset increases the recorded power losses up to a maximum of ∼27 kW. With SR processes turned on, the losses in the first few magnets and collimators for cs11 and cs11-dy200 are still within tolerable limits. The later collimators suffer higher power losses with SR processes with several showing tens of kW of power. The high luminosity cases – cs15 and cs15-dy120 – show intolerable losses with and without SR processes. Megawatt loss levels are observed on several of the collimators. With no SR tracking, the losses for cs21 appear to be within acceptable limits with the exception of VCOL2 – which receives nearly 50 kW of power. Synchrotron-related losses lead to further intolerable losses. The remaining 1.0 TeV parameter sets, with and without SR, all show high level of losses up to several megawatts in some instances. Tracking examples are given in Fig. 8.8.

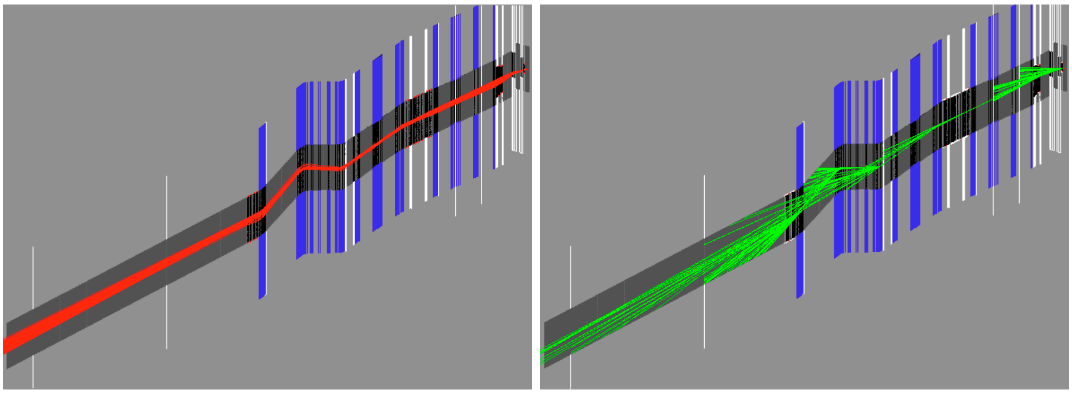

(a) Plan view – with 100 beam particles (b) Plan view – example of SR

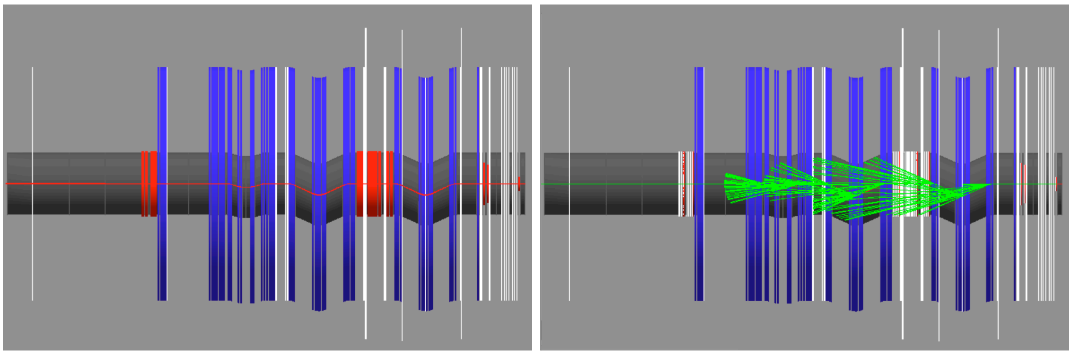

(c) Side view – with 100 beam particles (d) Side view – example of SR

Figure 8.8: 2 mrad extraction line tracking in BDSIM. Using 0.5 TeV nominal beam parameters and scaling x:y:z as 1:200:1.

Overall the 2 mrad power losses appear to be largely unacceptable. Only the nominal case for the 0.5 TeV parameter set, whilst assuming no vertical collision offsets, is seen to produce tolerable losses. Importantly, both the 0.5 and 1.0 TeV nominal parameter simulations show low losses on the first superconducting quadrupole, QD0.

14 and 20 mrad Results

In contrast to the 2 mrad results, the 20 mrad power losses have been quoted as the maximum power density for a group of magnet types. Due to the similarity between the 14 and 20 mrad optics lattices, the 14 mrad results have been given in the same format as the 20 mrad. In both the extraction line designs, the crucial superconducting elements receive no power losses for all nominal beam conditions, with and without vertical offsets and SR processes. For the high luminosity parameters the power loss in these magnets is above the $\sim$2 W tolerable limit. The cs11 parameter set shows tolerable losses for both extraction line designs with and without SR processes. The introduction of a vertical beam-beam offset produces high collimator losses for the 14 mrad design, but moderate losses for the 20 mrad. Both designs have generally high losses for the high luminosity beam conditions, but the 14 mrad is considerably worse with megawatt level losses observed in the case of a vertical offset. Tracking examples for the 20 mrad extraction line are given in Fig. 8.9.

Conclusions

The maturity of the 20 mrad design is clearly evident from the generally low power losses observed. The 0.5 TeV nominal beams are extracted in this design with tolerable power losses whereas the high luminosity case produces unacceptable losses on the superconducting elements and high losses on the collimators. The 1.0 TeV extraction results in tolerable losses, but collimator losses are high with SR. The 14 mrad performance shows that the current design is unable to extract high luminosity beams, but the nominal beams are extracted well with respect to losses on beam-lines – although special attention must be made to ensure collimator survivability.

The 2 mrad extraction line design is clearly a more complex system that requires significantly more effort in terms of lattice tuning than the larger crossing angle schemes. This becomes apparent from the power loss results that suggest that only the nominal beams in the ideal case of zero vertical offset are extractable within tolerable levels. The

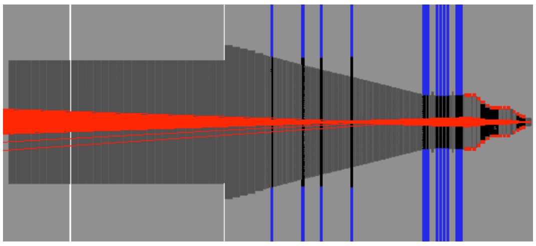

(a) Plan view – with 100 beam particles

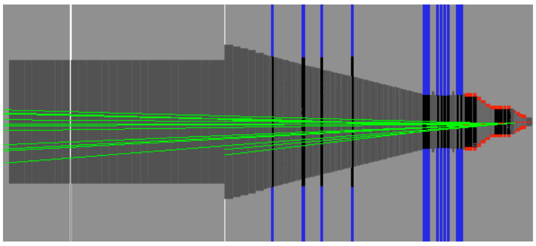

(b) Plan view – example of SR

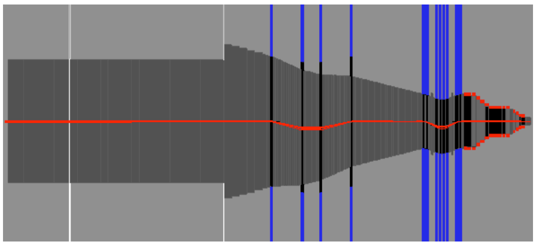

(c) Side view – with 100 beam particles

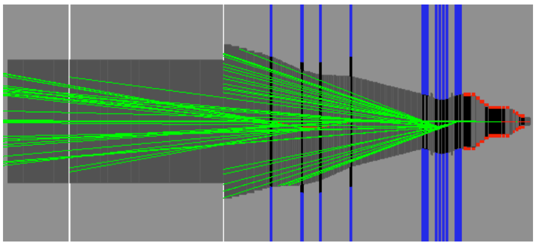

(d) Side view – example of SR

Figure 8.9: 20 mrad extraction line tracking in BDSIM. Using 0.5 TeV nominal beam parameters and scaling x:y:z as 1:200:1. Particle tracking in the 14 mrad design produces similar results.

lattice design of the 2 mrad scheme requires significant optimisation to attempt to reduce the power loss levels.

Table 8.2: 2 mrad extraction line power losses with all values quoted in units of Watts[b]. Beam statistics are also given.

	0.5 TeV Nominal		0.5 TeV High Luminosity	
Total Power	11.03M	10.89M	10.52M	10.18M
dy [nm]	0	200	0	120
QD0	0 $<$ 0.24	0 $<$ 0.24	106 $\pm$ 3.27	356 $\pm$ 35.7
SD0	0 $<$ 0.19	0 $<$ 0.19	0.31 $\pm$ 0.05	8.33 $\pm$ 4.80
SF1	0 $<$ 0.47	0 $<$ 0.47	4156 $\pm$ 105	2775 $\pm$ 319
ECOLA	0 $<$ 0.27	0 $<$ 0.27	264 $\pm$ 5.52	2294 $\pm$ 112
HCOL	0 $<$ 0.22	0 $<$ 0.22	6.67 $\pm$ 0.71	0 $<$ 0.25
VCOL	1.21 $\pm$ 0.43	4423 $\pm$ 468	1157 $\pm$ 19.8	1.02M $\pm$ 10.7k
VCOL2	735 $\pm$ 10.0	614 $\pm$ 52.4	63.9k $\pm$ 0.4k	103k $\pm$ 2.5k
HCOL2	813 $\pm$ 57.6	655 $\pm$ 100	845k $\pm$ 8.0k	545k $\pm$ 17.7k
HCOL3	230 $\pm$ 6.35	367 $\pm$ 52.5	10.0k $\pm$ 0.2k	18.0k $\pm$ 0.9k
ECOL0	10.1 $\pm$ 1.11	6711 $\pm$ 535	26.8k $\pm$ 0.6k	56.2k $\pm$ 2.5k
ECOL1	137 $\pm$ 15.1	27.3k $\pm$ 0.7k	11.7k $\pm$ 0.4k	475k $\pm$ 4.6k
ECOL2	1.65 $\pm$ 0.51	19.4k $\pm$ 0.6k	44.4 $\pm$ 3.25	413 $\pm$ 6.0k
ECOL3	0 $<$ 41.5	2563 $\pm$ 190	0 $<$ 41.5	209k $\pm$ 3.7k
Main Beam	640k	640k	640k	-
Tail	20k	50k	50k	1M

[b] The power loss tables in this chapter use the following symbolic notation: M $= 1 \times 10^6$, k $= 1 \times 10^3$, m $= 1 \times 10^{-3}$, $\mu = 1 \times 10^{-6}$.

Table 8.3: 2 mrad extraction line power losses with all values quoted in units of Watts. Beam statistics are also given.

	1.0 TeV Nominal		1.0 TeV High Luminosity	
Total Power	17.14M	16.68M	15.27M	14.36M
dy [nm]	0	100	0	80
QD0	0.86 $\pm$ 0.32	4.48 $\pm$ 0.94	9897 $\pm$ 153	17.0k $\pm$ 0.2k
SD0	0.09 $\pm$ 0.09	0.77 $\pm$ 0.39	132 $\pm$ 3.83	1155 $\pm$ 30.7
SF1	0 $<$ 0.31	0.17 $\pm$ 0.17	282 $\pm$ 31.1	1211 $\pm$ 40.6
ECOLA	55.7 $\pm$ 3.02	265 $\pm$ 11.2	21.8k $\pm$ 0.5k	47.4k $\pm$ 0.8k
HCOL	0.73 $\pm$ 0.33	2.16 $\pm$ 0.71	1257 $\pm$ 17.7	919 $\pm$ 41.0
VCOL	66.7 $\pm$ 3.71	62.8k $\pm$ 2.5k	6655 $\pm$ 281	963k $\pm$ 20.6k
VCOL2	45.2k $\pm$ 0.4k	110k $\pm$ 2.2k	740k $\pm$ 7.5k	407k $\pm$ 6.6k
HCOL2	10.3k $\pm$ 114	32.3k $\pm$ 1.7k	3.50M $\pm$ 31.9k	5.27M $\pm$ 45.2k
HCOL3	3746 $\pm$ 51.1	6078 $\pm$ 259	26.2k $\pm$ 0.7k	20.9k $\pm$ 0.7k
ECOL0	0 $<$ 0.99	8603 $\pm$ 365	62.8k $\pm$ 0.1k	359k $\pm$ 9.7k
ECOL1	3683 $\pm$ 49.1	101k $\pm$ 3.3k	76.4k $\pm$ 0.1k	581k $\pm$ 7.9k
ECOL2	0 $<$ 58.1	125k $\pm$ 2.5k	0 $<$ 58.1	201k $\pm$ 3.0k
ECOL3	0 $<$ 64.5	0 $<$ 64.5	0 $<$ 64.5	59.6k $\pm$ 1.3k
Main Beam	630k	620k	635k	625k
Tail	400k	600k	350k	1M

Table 8.4: 2 mrad extraction line power losses with SR processes turned on. All values quoted in units of Watts. Beam statistics are also given.

	0.5 TeV Nominal		0.5 TeV High Luminosity	
Total Power	11.03M	10.89M	10.52M	10.18M
dy [nm]	0	200	0	120
QD0	$0 < 0.58\mu$	$0 < 0.61\mu$	119 ± 10.2	349 ± 74.9
SD0	$2.26\mu \pm 2.24\mu$	$0.20\mu \pm 0.13\mu$	0.71 ± 0.02	31.5 ± 20.5
SF1	84.7 ± 3.72	37.1 ± 2.42	47.0k ± 1.1k	86.6k ± 5.1k
ECOLA	$0 < 0.24\mu$	$0 < 0.26\mu$	32.4 ± 4.76	554 ± 96.8
HCOL	4251 ± 9.89	4143 ± 9.77	4180 ± 11.1	3453 ± 22.5
VCOL	$0.31\mu \pm 0.22\mu$	1087 ± 13.9	140 ± 11.4	951k ± 5.9k
VCOL2	10.1k ± 0.03k	12.7k ± 0.4k	58.1k ± 0.3k	87.6k ± 3.8k
HCOL2	328 ± 6.97	792 ± 75.2	7971 ± 124	72.9k ± 3.6k
HCOL3	630 ± 9.88	656 ± 58.3	16.8k ± 0.7k	42.0k ± 2.3k
ECOL0	10.7k ± 0.01k	15.5k ± 0.6k	16.1k ± 0.7k	140k ± 4.7k
ECOL1	3060 ± 6.89	28.8k ± 1.4k	3445 ± 60.0	621k ± 5.5k
ECOL2	1635 ± 4.24	39.8k ± 1.6k	1588 ± 15.0	614k ± 5.2k
ECOL3	747 ± 3.03	32.6k ± 1.5k	1912 ± 325	392k ± 4.5k
Main Beam	100k	100k	100k	-
Tail	20k	45k	100k	200k

Table 8.5: 2 mrad extraction line power losses with SR processes turn on. All values are quoted in units of Watts. Beam statistics are also given.

	1.0 TeV Nominal		1.0 TeV High Luminosity	
Total Power	17.14M	16.68M	15.27M	14.36M
dy [nm]	0	100	0	80
QD0	0.48 ± 0.48	9.15 ± 3.40	10.7k ± 0.2k	17.2k ± 0.5k
SD0	0.32 ± 0.02	4.69 ± 2.02	658 ± 16.6	2557 ± 140
SF1	665 ± 13.1	1220 ± 14.1	78.2k ± 2.8k	57.1k ± 2.4k
ECOLA	10.3 ± 2.64	57.6 ± 9.00	7818 ± 113	19.5k ± 0.5k
HCOL	58.1k ± 0.1k	55.4k ± 0.1k	51.2k ± 0.2k	56.4k ± 0.2k
VCOL	0.69 ± 0.68	4874 ± 100	2295 ± 133	427k ± 8.7k
VCOL2	161k ± 0.3k	179k ± 0.6k	715k ± 10.4k	646k ± 5.0k
HCOL2	8550 ± 94.1	67.3k ± 0.4k	2.0M ± 32.4k	3.4M ± 67.8k
HCOL3	12.3k ± 0.1k	29.6k ± 0.3k	95.6k ± 3.3k	125k ± 2.0k
ECOL0	121k ± 0.2k	128k ± 0.5k	94.7k ± 0.3k	745k ± 9.8k
ECOL1	33.4k ± 0.06k	202k ± 3.7k	26.3k ± 0.1k	1.1M ± 13.0k
ECOL2	17.8k ± 0.04k	156k ± 3.9k	13.9k ± 0.05k	698k ± 9.3k
ECOL3	7691 ± 21.9	7723 ± 132	6128 ± 26.8	224k ± 5.7k
Main Beam	100k	100k	100k	100k
Tail	100k	100k	100k	100k

Table 8.6: 14 mrad extraction line power losses. Beam statistics are also given. Losses on collimators are given in watts, whereas losses on elements are given as maximum density (W/m) for a given group.

	0.5 TeV Nominal		0.5 TeV High Luminosity	
Total Power	11.03M	10.89M	10.53M	10.18M
dy [nm]	0	200	0	120
ECOL1	1.14 ± 0.62	2946 ± 45.5	38.0k ± 0.6k	1.01M ± 10.6k
ECOL2	1007 ± 77.5	27.1k ± 0.7k	233k ± 3.5k	856k ± 8.0k
ECOL3	527 ± 80.4	1863 ± 150	41.6k ± 1.0k	46.0k ± 0.8k
SC Quads	0 < 0.11	0 < 0.11	0.92 ± 0.20	1.32 ± 1.32
Warm Quads	0 < 0.13	0 < 0.13	28.5 ± 1.19	156 ± 16.0
Bends	0 < 0.27	0.05 ± 0.05	27.8 ± 1.18	589 ± 36.7
Main Beam	640k	640k	625k	-
Tail	20k	50k	900k	1M

Table 8.7: 14 mrad extraction line power losses. Beam statistics are also given. Losses on collimators are given in watts, whereas losses on elements are given as maximum density (W/m) for a given group.

	1.0 TeV Nominal		1.0 TeV High Luminosity	
Total Power	17.14M	16.68M	15.27M	14.36M
dy [nm]	0	100	0	80
ECOL1	223 ± 7.28	1011 ± 22.6	28.1k ± 0.7k	574k ± 6.6k
ECOL2	231 ± 7.27	15.2k ± 0.2k	369k ± 5.9k	1.27M ± 11.2k
ECOL3	16.3 ± 1.96	1780 ± 32.4	62.2k ± 1.3k	52.6k ± 1.1k
SC Quads	0 < 0.17	0 < 0.28	235 ± 4.27	236 ± 10.7
Warm Quads	0.66 ± 0.20	5.36 ± 0.81	2865 ± 33.4	3773 ± 68.6
Bends	2.74 ± 0.45	52.4 ± 3.40	2596 ± 75.8	8084 ± 194
Main Beam	630k	620k	635k	625k
Tail	400k	600k	350k	1M

Table 8.8: 14 mrad extraction line power losses with SR processes turned on. Beam statistics are also given. Losses on collimators are given in watts, whereas losses on elements are given as maximum density (W/m) for a given group.

	0.5 TeV Nominal		0.5 TeV High Luminosity	
Total Power	11.03M	10.89M	10.53M	10.18M
dy [nm]	0	200	0	120
ECOL1	2127 $\pm$ 5.51	4924 $\pm$ 21.0	38.5k $\pm$ 0.9k	1.07M $\pm$ 14.8k
ECOL2	3462 $\pm$ 116	18.4k $\pm$ 0.9k	210k $\pm$ 4.0k	878k $\pm$ 8.6k
ECOL3	1396 $\pm$ 7.04	2889 $\pm$ 319	39.6k $\pm$ 2.0k	46.9k $\pm$ 1.5k
SC Quads	0 $<$ 5.3m	0 $<$ 4.3m	0.39 $\pm$ 0.38	0 $<$ 0.80
Warm Quads	0 $<$ 0.9m	0 $<$ 0.7m	91.7 $\pm$ 6.47	750 $\pm$ 84.7
Bends	218 $\pm$ 1.11	219 $\pm$ 1.20	320 $\pm$ 8.78	5374 $\pm$ 274
Main Beam	100k	100k	100k	-
Tail	20k	45k	100k	200k

Table 8.9: 14 mrad extraction line power losses with SR processes turned on. Beam statistics are also given. Losses on collimators are given in watts, whereas losses on elements are given as maximum density (W/m) for a given group.

	1.0 TeV Nominal		1.0 TeV High Luminosity	
Total Power	17.14M	16.68M	15.27M	14.36M
dy [nm]	0	100	0	80
ECOL1	25.3k $\pm$ 0.07k	24.2k $\pm$ 0.07k	42.4k $\pm$ 1.3k	602k $\pm$ 17.5k
ECOL2	31.9k $\pm$ 0.07k	47.0k $\pm$ 0.3k	331k $\pm$ 6.9k	1.61M $\pm$ 17.0k
ECOL3	14.8k $\pm$ 0.04k	15.7k $\pm$ 0.1k	66.3k $\pm$ 2.7k	79.1k $\pm$ 3.3k
SC Quads	0 $<$ 0.01	0 $<$ 0.03	366 $\pm$ 7.85	347 $\pm$ 47.9
Warm Quads	0.74 $\pm$ 0.42	21.1 $\pm$ 3.59	10.6k $\pm$ 0.04k	26.0k $\pm$ 0.4k
Bends	1613 $\pm$ 8.06	1992 $\pm$ 25.8	11.8k $\pm$ 0.2k	59.8k $\pm$ 1.0k
Main Beam	100k	100k	100k	100k
Tail	100k	100k	100k	100k

Table 8.10: 20 mrad extraction line power losses. Beam statistics are also given. Losses on collimators are given in watts, whereas losses on elements are given as maximum density (W/m) for a given group.

	0.5 TeV Nominal		0.5 TeV High Luminosity	
Total Power	11.03M	10.89M	10.53M	10.18M
dy [nm]	0	200	0	120
ECOL1	1.71 $\pm$ 0.60	14.3 $\pm$ 1.44	47.9k $\pm$ 0.8k	384k $\pm$ 4.8k
ECOL2	28.7 $\pm$ 2.26	71.6 $\pm$ 3.54	74.5k $\pm$ 1.2k	319k $\pm$ 2.7k
SC Quads	0 $<$ 0.14	0 $<$ 0.14	14.5 $\pm$ 0.85	27.5 $\pm$ 6.66
Warm Quads	0 $<$ 0.11	0 $<$ 0.11	51.2 $\pm$ 1.39	226 $\pm$ 17.5
Bends	0 $<$ 0.28	0.10 $\pm$ 0.10	30.6 $\pm$ 1.28	886 $\pm$ 48.3
Main Beam	640k	640k	625k	-
Tail	20k	50k	900k	1M

Table 8.11: 20 mrad extraction line power losses. Beam statistics are also given. Losses on collimators are given in watts, whereas losses on elements are given as maximum density (W/m) for a given group.

	1.0 TeV Nominal		1.0 TeV High Luminosity	
Total Power	17.14M	16.68M	15.27M	14.36M
dy [nm]	0	100	0	80
ECOL1	606 $\pm$ 13.3	4847 $\pm$ 57.7	63.8k $\pm$ 1.1k	136k $\pm$ 1.0k
ECOL2	126 $\pm$ 5.34	551 $\pm$ 15.2	41.3k $\pm$ 1.3k	54.2k $\pm$ 1.2k
SC Quads	0 $<$ 0.20	0 $<$ 0.32	1128 $\pm$ 14.9	1248 $\pm$ 32.7
Warm Quads	1.14 $\pm$ 0.25	6.34 $\pm$ 0.79	4046 $\pm$ 70.5	5227 $\pm$ 59.4
Bends	3.58 $\pm$ 0.57	207 $\pm$ 28.4	2256 $\pm$ 86.6	8812 $\pm$ 0.2k
Main Beam	630k	620k	635k	625k
Tail	400k	600k	350k	1M

Table 8.12: 20 mrad extraction line power losses with SR processes turn on. Beam statistics are also given. Losses on collimators are given in watts, whereas losses on elements are given as maximum density (W/m) for a given group.

	0.5 TeV Nominal		0.5 TeV High Luminosity	
Total Power	11.03M	10.89M	10.53M	10.18M
dy [nm]	0	200	0	120
ECOL1	5483 ± 9.18	5276 ± 8.21	50.3k ± 1.3k	391k ± 9.6k
ECOL2	3910 ± 8.42	3852 ± 10.4	68.7k ± 2.1k	326k ± 4.1k
SC Quads	0 $<$ 5.4m	0 $<$ 5.7m	26.0 ± 3.67	58.2 ± 21.8
Warm Quads	3.3μ ± 2.2μ	3.2μ ± 3.1μ	119.0 ± 6.00	1006 ± 96.6
Bends	76.9 ± 0.59	81.8 ± 0.78	189.1 ± 7.89	6329 ± 304
Main Beam	100k	100k	100k	-
Tail	20k	45k	100k	200k

Table 8.13: 20 mrad extraction line power losses with SR processes turned on. Beam statistics are also given. Losses on collimators are given in watts, whereas losses on elements are given as maximum density (W/m) for a given group.

	1.0 TeV Nominal		1.0 TeV High Luminosity	
Total Power	17.14M	16.68M	15.27M	14.36M
dy [nm]	0	100	0	80
ECOL1	12.1k ± 19.5	65.7k ± 0.2k	106k ± 2.2k	188k ± 1.6k
ECOL2	8049 ± 17.5	45.5k ± 0.09k	64.3k ± 1.8k	97.3k ± 2.9k
SC Quads	0 $<$ 0.02	0 $<$ 0.04	2343 ± 25.6	2393 ± 167
Warm Quads	0 $<$ 3.4m	23.0 ± 3.49	11.6k ± 0.2k	27.0k ± 0.4k
Bends	0.29 ± 4.4m	1316 ± 26.1	8830 ± 350	63.2k ± 1.2k
Main Beam	100k	100k	100k	100k
Tail	100k	100k	100k	100k

Chapter 9

Summary

The ILC is a fast paced and rapidly evolving project that benefits from a huge level of international collaborative R&D effort. In the wake of the decision to use superconducting accelerator technology in 2004, the project has grown from the regionalised proposals of a future linear collider into today's globally driven ILC design. The advent of the Global Design Effort (GDE) has seen the development of the ILC design schedule, setting priorities and research targets for the international physics community. The first goal set by the GDE was the production of the Baseline Configuration Document (BCD) which laid down the key design concepts of the ILC. The BCD has collated studies and recommendations from all of the working groups and is to become the building blocks of the Reference Design Report (RDR). Expected for completion by early 2007, the main role of the RDR will be to provide a sufficient level of detail to enable the first proposals of costing and construction schedules for the ILC project. Following on from the RDR will be the development of a fully engineered design of the ILC in the form of the Technical Design Report (TDR). The schedule set by the GDE culminates in the first beam date for the ILC set at 2015.

The work contributed by this thesis has helped in key design choices throughout the lifetime of the BCD. Within the scope of the BDS and IRs, the development of the BDSIM software package has come at a crucial time – enabling the performance evaluations of a wide range of design proposals. The purpose built geometry interface allowed for the inclusion of detector descriptions under the same code framework as accelerator tracking. The user base and range of applications has quickly grown, both within the ILC project and more recently the LHC, proving BDSIM to be a flexible tool within the particle physics community.

The simulations performed to model the PETRA Laser-wire proved to be invaluable for allowing the successful progression of the project. After the installation of the signal exit window, the project was focused on decreasing the time for scans whilst also automating the process. The ability to scan the beam profile in a second plane has since been implemented at the PETRA installation. The optimisation of the locations of Laser-wire stations along the BDS is currently being investigated, along with the feasibility of linac-based beam profile monitors.

The appraisals of the extraction line designs have formed a significant contribution to the recent decision to change the baseline design with 2/20 mrad crossing angles with a 14/14 mrad scheme. In particular, the power losses shown to be experienced by the 2 mrad design – from both disrupted beams and also radiative Bhabha particles – have been instrumental. The cooling costs and restrictive degree of optics optimisation have been deemed sufficient to re-prioritise the design to be an alternative option as opposed to being part of the baseline configuration.

Bibliography

[1] F. Halzen and A. D. Martin. *Quarks & Leptons: An Introductory Course in Modern Particle Physics*. J. Wiley, 1984.

[2] S. Eidelman et al. Review of particle physics. *Phys. Lett.*, B592:1, 2004.

[3] Tevatron Electroweak Working Group. Combination of CDF and D0 Results on the Mass of the Top Quark. August 2006. hep-ex/0608032 - Temporary Submission.

[4] Takaaki Kajita. Atmospheric neutrino results from Super-Kamiokande and Kamiokande: Evidence for nu/mu oscillations. *Nucl. Phys. Proc. Suppl.*, 77:123–132, 1999. hep-ex/9810001.

[5] R. Barate et al. Search for the standard model Higgs boson at LEP. *Phys. Lett.*, B565:61–75, 2003. hep-ex/0306033.

[6] Thomas Hambye and Kurt Riesselmann. SM Higgs mass bounds from theory. 1997. hep-ph/9708416.

[7] E. Wilson. Accelerator lecture series. Presented at the John Adams Institute, 2004.

[8] H. Wiedemann. *Particle Accelerator Physics I*. Springer, 2003.

[9] G. Weiglein et al. Physics interplay of the LHC and the ILC. *Phys. Rept.*, 426:47–358, 2006. hep-ph/0410364.

[10] F. Abe et al. Observation of top quark production in $\bar{p}p$ collisions. *Phys. Rev. Lett.*, 74:2626–2631, 1995. hep-ex/9503002.

[11] Manel Martinez and Ramon Miquel. Multi-parameter fits to the t anti-t threshold observables at a future e+ e- linear collider. *Eur. Phys. J.*, C27:49–55, 2003. hep-ph/0207315.

[12] Iain W. Stewart. Threshold top quark production. *AIP Conf. Proc.*, 618:395–404, 2002. hep-ph/0201180.

[13] S. Boogert. Luminosity spectrum impact on the top mass. Presented at the QCD and Top session at the ECFA meeting in Durham, UK, September 2004.

[14] S. Heinemeyer, S. Kraml, W. Porod, and G. Weiglein. Impact of a precise top measurement. September 2004. hep-ph/0409063.

[15] G. A. Moortgat-Pick et al. The role of polarized positrons and electrons in revealing fundamental interactions at the linear collider. 2005. hep-ph/0507011.

[16] R. Brinkmann, N. J. Walker, and G. A. Blair. The tesla post-linac collimation system. *DESY-TESLA-2001-12*, 2001.

[17] S. Herzbach. SR Fans in NLC FF. Proceedings BD-IR, http://accelerator.dl.ac.uk/ap/bdir2000/proceedings.htm, 2000.

[18] Patrick Krejcik. Status of the slc: Developments in linear collider physics. Talk given at 17th International Linear Accelerator Conference (LINAC 94), Tsukuba, Japan, 21-26 Aug 1994.

[19] T. O. Raubenheimer. The core emittance with intrabeam scattering in e+ / e- rings. *Part. Accel.*, 45:111–118, 1994.

[20] P. Tenenbaum, T. O. Raubenheimer, and M. Woodley. Sources of beam halo in the Next Linear Collider main linac. Contributed to IEEE Particle Accelerator Conference (PAC 2001), Chicago, Illinois, 18-22 Jun 2001.

[21] W. Kozanecki, T. Markiewicz, and T. Tauchi. Beam delivery and interaction region: overview of critical design choices. Presented in Working Group 4 at the ILC Workshop, KEK, November 2004.

[22] A. E. Blinov et al. Large impact parameters cutoff in bremsstrahlung at colliding beams. *Phys. Lett.*, B113:423, 1982.

[23] T. Maruyama. Power Load from Radiative Bhabhas in 2mrad Extraction. SLAC ILC BDS Meeting, April 2005.

[24] L. P. Keller. Calculation of muon background in a 0.5-tev linear collider. Contributed to DPF Summer Study on High Energy Physics, Snowmass, CO, Jun 25 - Jul 13, 1990.

[25] D. S. Denisov, N. V. Mokhov, S. I. Striganov, M. A. Kostin, and I. S. Tropin. Machine-related backgrounds in the SiD detector at ILC. 2006. hep-ex/0608001.

[26] D. Angal-Kalinin, H. Yamamoto, and A. Seryi. Bds report. Summary report presented at the Vancouver Linear Collider Workshop (VLC06), 21-Jul 2006.

[27] I. Will, G. Koss, and I. Templin. The upgraded photocathode laser of the TESLA Test Facility. *Nucl. Instrum. Meth.*, A541:467–477, 2005.

[28] Wiki page for the Baseline Configuration Document. http://www.linearcollider.org/wiki/doku.php?id=bcd:bcd_home.

[29] ILC Global Design Effort. web page for authoring the baseline configuration document. http://www.linearcollider.org/cms/?pid=1000104.

[30] Raubenheimer T. Suggested ILC Beam Parameter Range. http://www-project.slac.stanford.edu/ilc/acceldev/beamparameters.html, February 2005.

[31] F.Poirier. *Beam Diagnositc Laser-Wire and Fast Luminosity Spectrum Measurement at the International Linear Collider*. PhD thesis, Royal Holloway University of London, 2005.

[32] Peter Tenenbaum and Tsumoru Shintake. Measurement of small electron-beam spots. *Ann. Rev. Nucl. Part. Sci.*, 49:125–162, 1999.

[33] P. Eliasson and D. Schulte. Dispersion free steering and emittance tuning bumps in the ilc linac. EUROTEV-REPORT-2005-021.

[34] T. Kamps. Compton scattering techniques for the measurement of the transverse beam size at the future linear collider. Presented at the Institute of Physics meeting in Southampton, UK, April 2001.

[35] G. A. Blair et al. Proposing a laser based beam size monitor for the future linear collider. Presented at IEEE Particle Accelerator Conference (PAC 2001), Chicago, Illinois, 18-22 Jun 2001.

[36] S. Malton. *Laser Interactions with High Brightness Electron Beams*. PhD thesis, University College of London, 2007. To be submitted.

[37] J. Carter. A beam position monitor for the laserwire project. Master's thesis, Royal Holloway University of London, August 2003.

[38] K. Balewski et al. Beam profile measurements at petra with the laserwire compton scattering monitor. Presented at the 9th European Particle Accelerator Conference (EPAC 2004), Lucerne, Switzerland, 5-9 Jul 2004.

[39] J. Keil. Orbit-Response-Matrix Analysis for PETRA-e. HERA Beam Dynamics Seminar, July 2003.

[40] J. Carter et al. Beam profile measurements and simulations of the PETRA laser-wire. 2005. physics/0508137.

[41] G. A. Blair. Simulation of the CLIC beam delivery system using BDSIM. CERN-OPEN-2002-057.

[42] I. Agapov, J. Carter, et al. BDSIM - Beamline Simulation Toolkit based on GEANT4. 2006. EUROTeV-Report-2006-035.

[43] S. Agostinelli et al. Geant4: A simulation toolkit. *Nucl. Instrum. Meth.*, A506:250–303, 2003.

[44] The ROOT System Home Page. http://root.cern.ch.

[45] I. Agapov. GMAD Accelerator Description Language. 2006. EUROTeV-Memo-2006-003-1.

[46] MAD-X Users' Guide. http://mad.home.cern.ch/mad/uguide.html.

[47] BDSIM Web Page. http://flc.pp.rhul.ac.uk/bdsim.html.

[48] LCG Web area at CERN. http://lcg.web.cern.ch/LCG/.

[49] BDSIM Accelsoft Web Page. http://flc.pp.rhul.ac.uk/accelsoft.html.

[50] R. Servranckx, Karl L. Brown, Lindsay Schachinger, and David Douglas. Users guide to the program DIMAD. SLAC-0285.

[51] Karl L. Brown, Frank Rothacker, David C. Carey, and F. C. Iselin. TRANSPORT: A computer program for designing charged particle beam transport systems. CERN-80-04.

[52] R. Appleby, P. Bambade, O. Dadoun, and A. Ferrari. Particle tracking in the ILC extraction lines with DIMAD and BDSIM. 2006. physics/0607163.

[53] A. Drozhdin and N. Mokhov. The STRUCT Program Users' Reference Manual. http://www-ap.fnal.gov/∼drozhdin, 2005.

[54] Mokka Web Page. http://polywww.in2p3.fr/geant4/tesla/www/mokka/mokka.html.

[55] A. Vogel. Simulations of Neutron Background in an ILC TPC using Geant4 - First Results from Mokka. Presented at the ILC European Regional Meeting, RHUL, UK, June 2005.

[56] Brett Parker and Andrei Seryi. Compensation of the effects of detector solenoid on the vertical beam orbit in NLC. *Phys. Rev. ST Accel. Beams*, 8:041001, 2005.

[57] SiD Detector Concept. http://www-sid.slac.stanford.edu/.

[58] GDML Web area at CERN. http://cern.ch/GDML/.

[59] World Wide Web Consortium. http://www.w3.org/XML/.

[60] J. McCormick. Full detector simulation using SLIC and LCDD. Contributed to 2005 International Linear Collider Workshop (LCWS 2005), Stanford, California, 18-22 Mar 2005.

[61] Hans-Ulrich Martyn. Detection of sleptons at a linear collider in models with small slepton neutralino mass differences. 2004.

[62] Olivier Napoly. The luminosity for beam distributions with error and wake field effects in linear colliders. *Part. Accel.*, 40:181–203, 1993.

[63] T. Raubenheimer. Accelerator Physics and Technologies for Linear Colliders. Lecture notes presented at University of Chicago, January 2002.

[64] G. Burt et al. Crab Cavity System for the ILC. *ECONF*, C0508141:ILCAW0532, 2005.

[65] (ed.) Behnke, T., (ed.) Bertolucci, S., (ed.) Heuer, R. D., and (ed.) Settles, R. TESLA: The superconducting electron positron linear collider with an integrated X-ray laser laboratory. Technical design report. Pt. 4: A detector for TESLA. DESY-01-011.

[66] Y. Iwashita. RF kicker update. Proceedings Snowmass ILC Workshop, http://www.slac.stanford.edu/econf/C0508141/proc/ilcaw5.htm, August 2005.

[67] L. Keller. Zero degree extraction using an electrostatic separator. Proceedings Snowmass ILC Workshop, http://www.slac.stanford.edu/econf/C0508141/proc/ilcaw5.htm, aug 2005.

[68] A. Stahl. New design of the mask. Presented at the Linear Collider Workshop, Amsterdam, March 2003.

[69] P. Tenenbaum. NLC Collimation. Presented at the NLC Collaboration Meeting, March 2001.

[70] N. Watson. ILC Collimator Design. High Energy Physics Seminar at RHUL, UK, February 2006.

[71] N. Watson and P. Tenenbaum. Spoiler wakefield test proposal at end station a, slac. http://hepunx.rl.ac.uk/swmd/beam/.

[72] Spoiler Wakefield and Mechanical Design. http://hepunx.rl.ac.uk/swmd/beam/.

[73] C. Spencer and B. Parker. ILC IR and Extraction Line Magnet CHALLENGES. Presented at the ILC-BDIR Workshop at RHUL, UK, June 2005.

[74] D. Jackson. Vertex detector modelling. Private Communications, May 2005.

[75] D. Schulte. *Study of Electromagnetic and Hadronic Background in the Interaction Region of the TESLA Collider*. PhD thesis, University of Hamburg, September 1996.

[76] D. Angal-kalinin, A. Seryi, and H. Yamamoto. Beam delivery design. Presented at the DCB meeting for the Global Design Effort, August 2006.

[77] D. Angal-Kalinin. Beam Delivery System for the Linear Collider. Presented for an ASTeC Seminar, October 2003.

[78] M. Woodley. ILC2006b BDS Documentation. http://www.slac.stanford.edu/ mdw/ILC/2006b/doc/.